A Novel Retro-directive Phased Array Antenna Architecture

by

Kaveh Fereidani

A thesis
presented to the University of Waterloo
in fulfillment of the
thesis requirement for the degree of
Doctor of Philosophy
in
Electrical and Computer Enginnering

Waterloo, Ontario, Canada, 2018

Examining Committee Membership

The following served on the Examining Committee for this thesis. The decision of the Examining Committee is by majority vote.

External Examiner:	Amir Mortazawi Professor, Dept. of Electrical Engineering & Computer Science, University of Michigan
Supervisor:	Safieddin Safavi-Naeini Professor, Dept. of Electrical Engineering & Computer Engineering, University of Waterloo
Internal Member:	John Long Professor, Dept. of Electrical Engineering & Computer Engineering, University of Waterloo
Internal Member:	Slim Boumaiza Professor, Dept. of Electrical Engineering & Computer Engineering, University of Waterloo

Internal-External Member:	James Martin Associate Professor, Dept. of Physics & Astronomy, University of Waterloo
Defense Chair:	Michael Mayer Associate Professor, Dept. of Mechanical and Mechatronics Engineering, University of Waterloo

I hereby declare that I am the sole author of this thesis. This is a true copy of the thesis, including any required final revisions, as accepted by my examiners.

I understand that my thesis may be made electronically available to the public.

Abstract

Mobile wireless communication scenarios can range from a simple indoor WiFi link to a satellite internet connection to an airplane. Virtually in all scenarios, dynamic changes in the propagation environment or the movement of transmitter and receiver are inevitable. Therefore, the wireless link often experiences quality degradation or even interruption.

Adaptive antenna arrays offer a promising solution to combat wireless channel impairments as they adaptively reshape their radiation pattern. For two-way communication, an antenna should be retro-directivemeaning its transmit and receive beams are aligned. To achieve retro-directivity, techniques based on direction-of-arrival and self-phasing can be used. The former usually calls for a complex calibration routine to estimate the direction of arrival and beamsteering; the latter relies on the received signal to generate the transmit beam, imposing several limitations on its adaptability.

In this thesis, a novel retro-directive phased array architecture is proposed that does not require calibration and which generates its transmit wave independently of its receive wave. Moreover, its radiation pattern can be adaptively shaped by a simple beamforming algorithm, while its transmitted and received beams remain aligned. Structurally, it is comprised of independent modules that can be placed in virtually any arrangement without any hardware modification.

The architecture uses the LO phase-shifting technique to steer its beams. The LO signals are generated with a novel frequency synthesizer; it creates a pair of LO signals for the transmission and reception paths to achieve retro-directivity. The proposed antenna architecture is demonstrated practically using a 10-element prototype, verifying its ability to steer the transmit and receive beams while keeping them aligned. In addition, two of the key circuit components of the LO synthesizer, a fractional frequency divider and a novel phase-conjugating phase shifter, are designed and successfully implemented on 65nm CMOS technology, paving the path for use in future applications.

Acknowledgements

First and for most, I would like to express my gratitude to my supervisor Prof. Safavi-Naeini for his great support and supervision. Secondly, my great committee members, Prof. Mortazawi, Prof. Long, Prof. Mansour, Prof. Boumaiza, and Prof. Marin for their valuable feedback and advice.

I had the privilege of working with an excellent research team here at the Centre for Intelligent Antenna and Radio Systems (CIARS), University of Waterloo. I learned and enjoyed working with all team members, and I would like to thank them all specially, Dr. Hussam Al-Saedi and Mr. Stanley Ituah for their valuable feedbacks and sharing their knowledge, and Dr. Aidin Taeb for his great support during these years without whom accomplishing critical parts of my project were next to impossible.

Dedication

This is dedicated to the memory of my brother and my dearest Mahboubeh.

Table of Contents

List of Tables

List of Figures

Chapter 1

Introduction

Mobile wireless communication scenarios can range from a simple indoor WiFi link to a satellite internet connection to an airplane. Virtually in all scenarios, dynamic changes in the propagation environment or the movement of transmitter and receiver are inevitable. Therefore, the wireless link often experiences quality degradation or even interruption. One solution is to employ adaptive antennas on either side of the wireless link, to maintain the link quality through adaptive beamforming. For example, in Figure 1.1 the link between the satellite and car may be compromised due to the relative motions of the car and satellite and any multipath reflections created from the surroundings. An adaptive antenna mounted in the car could steer its beam(s) to track the satellite and maintain the link and even use the multipath reflections to its advantage by forming secondary beams [1].

The focus of this work is the design and development of a novel Retro-Directive Phased Array (RDPA) antenna; an innovation which could greatly simplify the design and implementation of adaptive antennas. The term *retro-directive* means the transmitting beam of the antenna is always in alignment with its receiving beam. In this chapter, the applications of adaptive antennas in wireless communications are reviewed. Then, conventional adaptive antenna architectures and the basics of phased array antennas are presented. Finally, the shortcomings and challenges of the conventional architectures are discussed.

1.1 Adaptive antennas for wireless communication

The capacity of the modern wireless networks are limited by the amount of interference in the given area, [2, 3], which makes it important to transmit and receive with the least

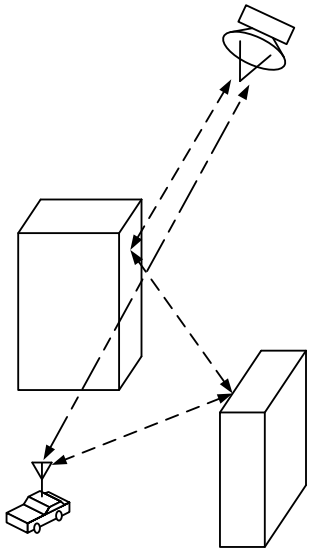

Figure 1.1: Two-way communication between satellite and car with multiple reflections from surroundings.

amount of interference. As shown in Figure 1.2, an adaptive antenna is able to optimize its radiation patterns to maximize the received signal while causing least amount of interference to others [4].

Another scenario which can benefit tremendously from adaptive antennas is point-to-point wireless links between mobile platforms. In these scenarios, the link capacity is mainly limited by the signal to noise ratio rather signal to interference ratio. Adaptive antennas can increase signal to noise ratio of a link by forming beam(s) toward the desired signal direction(s), and as a result, suppressing noise reception from other directions.

One of the more prominent examples of such a link is satellite on-the-move communication. There are growing research and development efforts aimed at providing global internet access using satellite links to mobile, nomadic [1], and fixed platforms [5].

Currently, most satellite data links are provided by geostationary orbit (GEO) satellites from 36000 km above the earth surface. Due to the great distance, a high gain antenna (e.g. 40dB) is required at the ground terminal. Providing such high gain antennas with beam steering capabilities is very challenging; as a result, solutions are costly and are limited in application (e.g. airplane connectivity).

[1] A platform that moves from one place to another but remains fixed while using the service

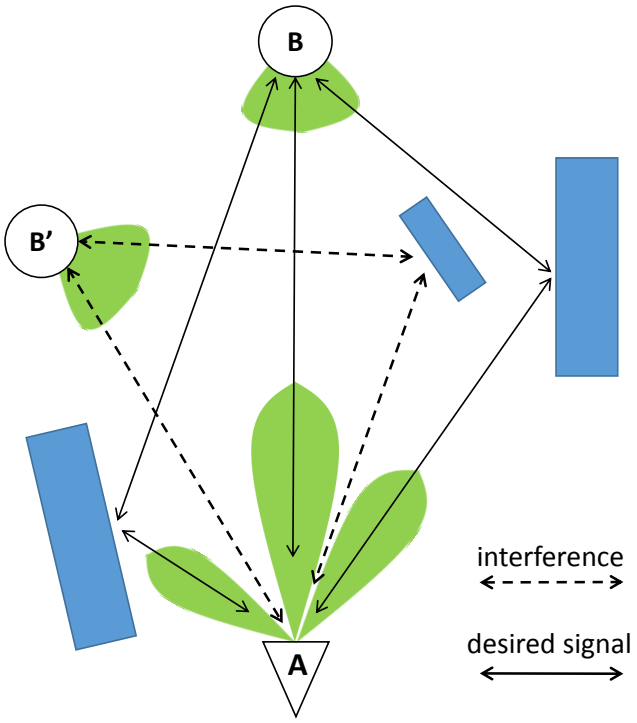

Figure 1.2: Adaptive antenna at node A optimizes radiation patterns for maximum transmission/reception to node B, and minimum interference to node B'.

Besides the already existing GEO satellite-based services, there is great potential to provide globe-wide internet access using medium and low orbit (MEO and LEO) satellite constellations [5]. To date, however, there are no widespread services using MEO or LEO due to the inherent technical challenges and high cost.

In recent years, however, two technological breakthroughs brought the prospect of ubiquitous satellite-based internet service closer: (i) advancements in satellite technology, such as the advent of CubeSats, and (ii) solutions for economical cargo delivery to LEO, such as reusable rockets. Moreover, thanks to the lower orbiting distance, LEO and MEO satellite links exhibit up to 100 times lower latencies than those of GEO satellite links (> 240 msec); making them suitable for real-time applications.

Now, the only missing part to enabling such a globe-wide internet service is a low-cost adaptive antenna at the ground station. Contrary to GEO satellite links, ground terminal antennas must be able to steer their beams to track a satellite, whether the ground terminal

is stationary or mobile. Fortunately, the required antenna gain is lower than that of GEO satellite-based services ($< 25\,\mathrm{dB}$); however, the antenna must be very low cost.

There are three large ongoing projects aimed at providing global space-borne internet access. SpaceX has proposed a 4425 LEO nano-satellite constellation, operating at Ku- and Ka-bands, that would communicate directly to end user ground terminals [6]. OneWeb's project proposal is based on a constellation of 720 Ku- and Ka-band LEO satellites that would link to larger ground terminals such as buildings. Local access to the end user would be provided by existing infrastructure (e.g. WiFi, cellular networks) [6, 7]. Finally, a company named O3b, is providing a medium latency (150msec) data link to internet service providers (ISP) through their MEO satellite constellations and a network of large mechanically-tracking reflector antennas [6, 8]. They have also proposed Ka- and V-bands LEO satellite constellations. All three companies have applied for frequency band licensing from FCC [1], but up to this date no frequency band has been granted. Once the frequency band is granted they have limited time to utilize it, otherwise the band will be licensed to others. Therefore, it is anticipated that there will be a great thrust to establish a satellite based internet in the near future, which will make related technologies such as adaptive antennas more interesting.

There are also attempts to provide internet service using an airborne platform including Google's Loon project, [9], and Facebook's Aquila project [10]. The former is based on flying balloons and the latter on high altitude solar-powered airplanes. High-gain antennas with tracking capabilities may not be necessary for these airborne scenarios; however, a low cost low-to-moderate gain adaptive antenna could improve the system performance considerably.

1.2 Adaptive antenna architectures

The essential parts of an adaptive antenna are shown in Figure 1.3. They include: (i) a flexible-beam antenna (usually a phased array antenna), and (ii) a beamforming algorithm. It worth mentioning that adaptive antennas that are mechanically-steerable have been commercialized, but they are bulky, prone to mechanical failure, and cannot deliver the level of agility required for emerging applications. Therefore, phased array antennas have become the ultimate choice for adaptive antenna systems.

As shown in Figure 1.3, the beamforming algorithm can monitor the received signal (RX) level and use it as feedback to find the optimal RX beamforming coefficients for

[1] Federal Communications Commission

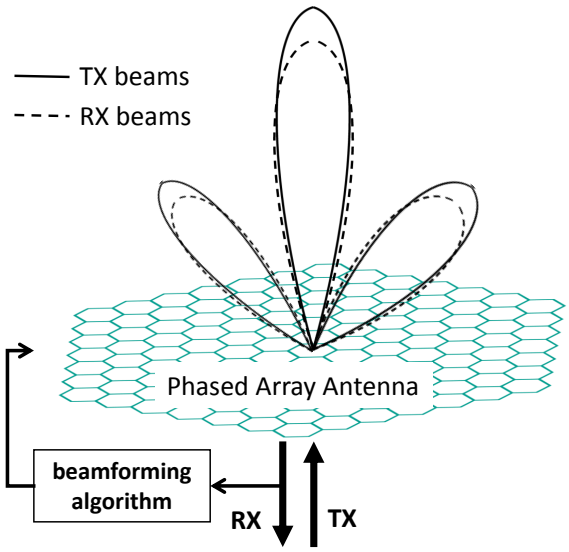

Figure 1.3: General block diagram of an adaptive antenna.

maximum reception, as in [11]. The algorithm is essentially an optimization algorithm whose variables are the complex coefficients of the array (i.e. phase and amplitude of the signal at each element), and whose goal is to maximize the received power (or SNR [1] or SIR [2]).

Figure 1.4 shows the general operation of a beamforming algorithm in receiving mode. The algorithm starts with an initial condition and changes the RX beamforming coefficients until the received signal characteristics (RSC) reach predefined values (DSC).

When transmitting, however, there is no information about the level of the transmitted signal (TX) that reaches the other end of the communication link. There are two conventional approaches for working around this problem: (i) estimating the direction of arrival (DoA) of the RX wave and steering the TX beam to that direction (e.g. [12]), and (ii) employing self-phasing techniques to generate a TX beam aligned with that of the RX (e.g. [13]). However, each approach has certain shortcomings, as discussed in the following sections.

[1] Signal-to-noise ratio

[2] signal-to-interference ratio

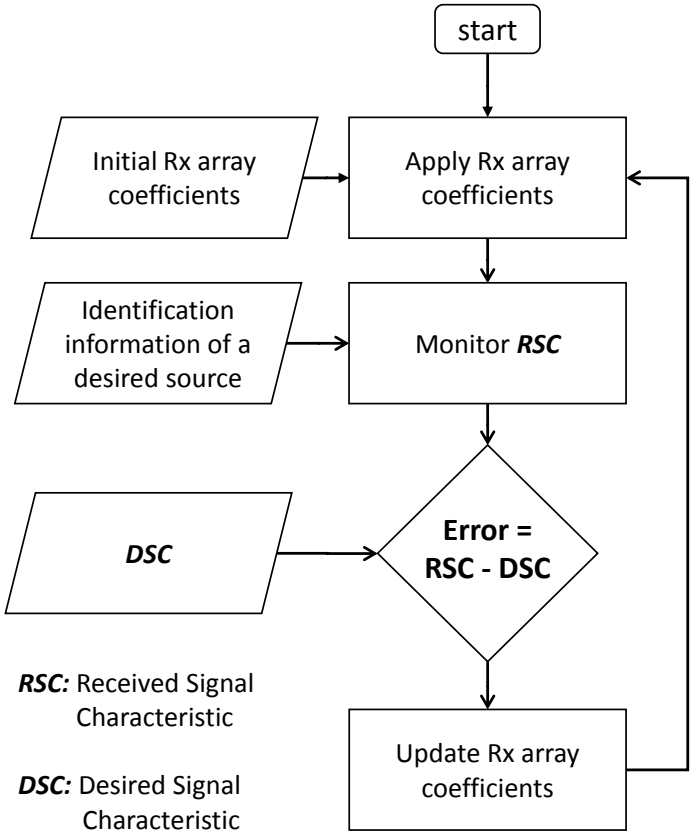

Figure 1.4: High-level flow chart of general operation of a beamforming algorithm in receiving mode.

1.2.1 DoA-based adaptive antennas

Figure 1.5 shows an operational diagram of a DoA-based antenna. The RX signal is utilized as feedback to optimize the RX beamforming coefficients for maximum reception. Then, based on those coefficients, the DoA of the RX wave is estimated. From the resulting DoA, the TX beamforming coefficients are generated. In the processes of DoA estimation and TX beamforming, it is essential to know the phased array antenna response (relation between the beamforming coefficients and the radiation pattern).

In practice, many secondary effects such as mutual coupling between the antenna array elements, uncertainty in the electronic components (especially phase shifters), and thermally induced mechanical and electronic variations, cause the response of the array to vary

dynamically. These effects necessitate the inclusion of a calibration routine that constantly estimates the phased array response to provide a set of beamforming calibration values. Moreover, it is assumed that the incoming wave has a well-defined DoA; an assumption that does not hold in the presence of strong multipath reflections [14].

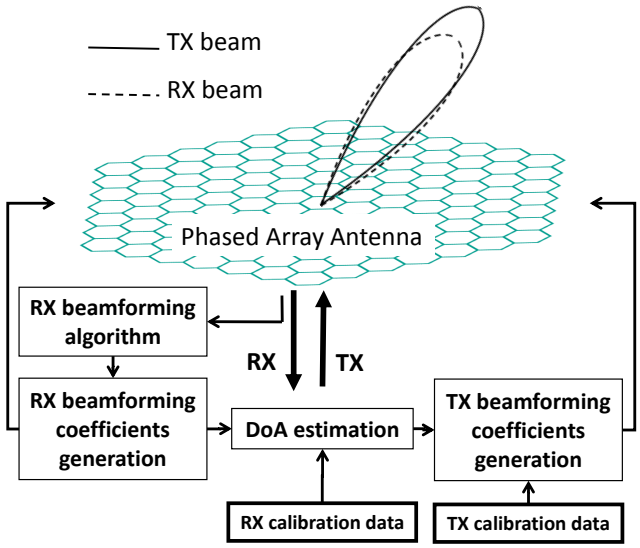

Figure 1.5: General block diagram of an adaptive antenna.

1.2.2 Self-phased antennas

In contrast to DoA-based antennas, self-phased antennas make no attempt to estimate DoA or to steer the TX beam. In fact, the TX wave is created from the RX wave in such a way that the TX wave travels in the opposite direction to the RX wave. Hence, these antennas can reply to the other side of the link only when they are illuminated by an RX wave. Figure 1.6 depicts an operational diagram of a self-phased antenna. The idea is to create a TX wave at the antenna aperture whose phase front is the conjugate of the RX phase front. The phase conjugation results in a TX wave that travels in the opposite direction to the RX wave [13]. In the following section, the main architectures of self-phased arrays and their operational principles and shortcomings are briefly reviewed.

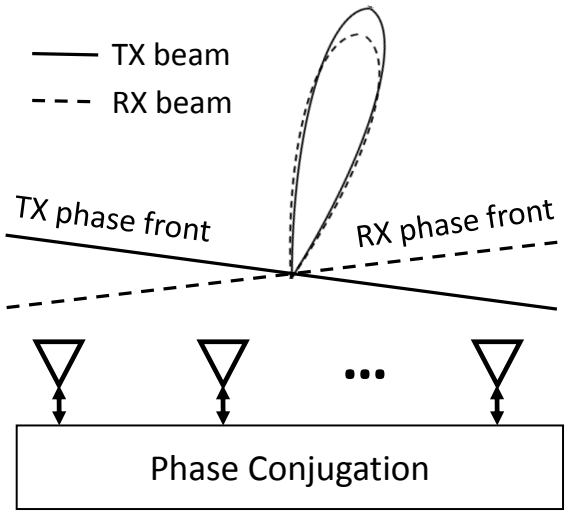

Figure 1.6: A self-phased antenna conjugates the phase front of the RX wave to create a TX wave traveling in the opposite direction.

Van-Atta array antenna

In the simplest case, a corner reflector can be considered as a self-phased antenna able to reflect the RX signal back to its source independently of the direction of illumination. The first self-phased array structure, known by the name of its inventor, was proposed by L.C. Van-Atta in 1959 [15]. As shown in Figure 1.7, a Van-Atta array is comprised of an array of antenna elements arranged along a straight line and connected by equal-length transmission lines. The specific connection between the antenna elements guides the wave received by the n^{th} antenna element to be reradiated by the $(N-n+1)^{th}$ element. As a result, the electric field of the reradiated wave (i.e. the TX wave) at the array aperture can be obtained from that of the RX wave by replacing x with $-x$, i.e.,

$$\mathbf{E}_{RX}(t, x, y=0) = \Re\big(e^{j\omega t} e^{-jk\hat{\mathbf{a}}_r.\mathbf{x}}\big) \tag{1.1a}$$

$$\mathbf{E}_{TX}(t, x, y=0) = \Re\big(e^{j\omega t} e^{jk\hat{\mathbf{a}}_r.\mathbf{x}}\big) \tag{1.1b}$$

where $\hat{\mathbf{a}}_r$ is the radial unit vector aligned with the direction of the incoming wave. Equations (1.1a) and (1.1b) clearly show that the field $\mathbf{E}_{TX}(t, x, y=0)$ creates a TX wave travels in the opposite direction to the RX wave.

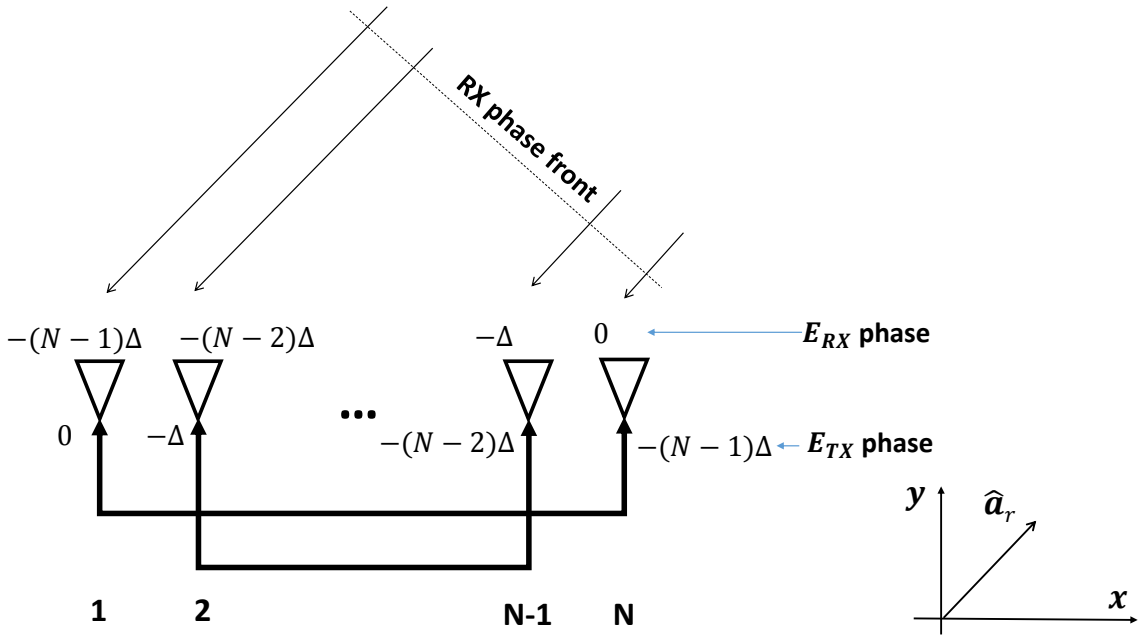

Figure 1.7: Van-Atta retro-directive array (recreated from [15]).

To amplify the amplitude of the reradiated wave and in some cases to modulate it with a message, bi-directional amplifiers and mixers are used between the antenna elements in the transmission lines of a Van-Atta array [16], [17].

Heterodyne self-phased array antennas

By examining (1.1) it is evident that instead of changing x to $-x$, one can obtain the same result as (1.1b) by replacing t with $-t$, i.e.,

$$\mathbf{E}_{RX}(t,x,y=0) = \Re\big(e^{j\omega t}e^{-jk\hat{\mathbf{a}}_r.\mathbf{x}}\big) \xrightarrow{t\to -t} \mathbf{E}^*{}_{RX}(t,x,y=0) = \Re\big(e^{-j\omega t}e^{-jk\hat{\mathbf{a}}_r.\mathbf{x}}\big) = \Re\big(e^{j\omega t}e^{jk\hat{\mathbf{a}}_r.\mathbf{x}}\big), \qquad (1.2)$$

where the asterisk denotes the time conjugation ($t \to -t$). As seen in (1.2), $\mathbf{E}^*{}_{RX}$ is equal to $\mathbf{E}_{TX}$ in (1.1).

For narrow-band signals, the time conjugation is equivalent to the phase conjugation ($e^{j\omega t} \to e^{-j\omega t}$), and can be easily performed by a phase conjugator circuit at each antenna element. The schematic of a phase-conjugating self-phased array is shown in Figure 1.8a.

In this configuration, the incident wave received by each antenna element passes through a phase conjugating circuit before being transmitted by the same antenna element. Note that in contrast to a *Van-Atta* array, the locations of the elements in a phase-conjugating array can be arbitrary because the phase conjugation of the wave phase fronts is performed in the time domain. To isolate the RX and TX signals, a circulator is used.

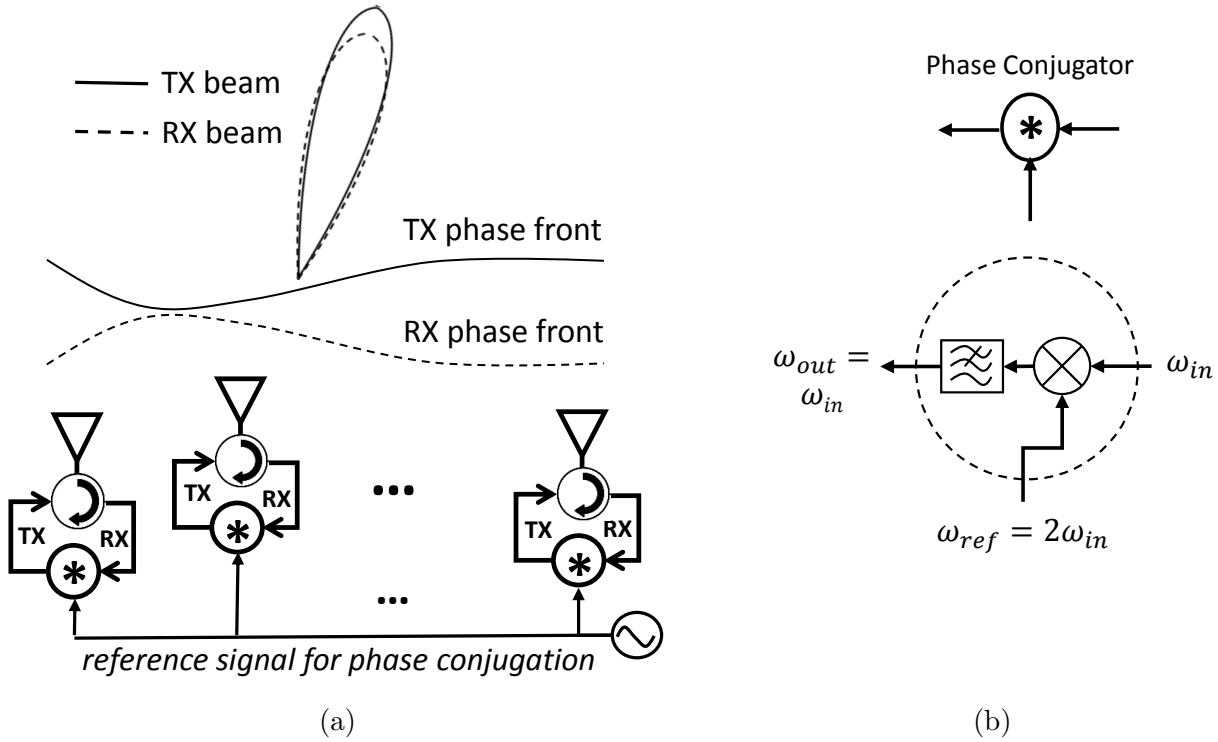

(a) (b)

Figure 1.8: (a) Phase-conjugating self-phased array. (b) Heterodyne phase conjugator.

A straightforward way to achieve phase conjugation is known as heterodyne phase

conjugation. This technique is based on the fact that in a frequency mixing such as,

$$S = A\cos(\omega t + \phi) \tag{1.3a}$$

$$S_{ref} = \cos(\omega_{ref} t + \phi_{ref}),\ \omega_{ref} > \omega \tag{1.3b}$$

$$S \times S_{ref} = \underbrace{\frac{A}{2}\cos((\omega_{ref} - \omega)t + \phi_{ref} - \phi)}_{\text{lower sideband}} + \underbrace{\frac{A}{2}\cos((\omega_{ref} + \omega)t + \phi_{ref} + \phi)}_{\text{upper sideband}}, \tag{1.3c}$$

the phase of the lower sideband, $\phi_{ref} - \phi$, is the conjugate of S phase, ϕ, with respect to the phase reference ϕ_{ref}. Note that in the self-phased array shown in Figure 1.8a, the same phase reference should be provided to all phase-conjugating circuits so that all phase conjugations are performed with the same reference.

By choosing $\omega_{ref} = 2\omega$, the lower sideband of the mixing product will have the same frequency as the input. This phase conjugation technique has been used in many self-phased arrays (e.g. [18, 19]). The internal circuitry of a simple heterodyne phase conjugating circuit is shown in Figure1.8b, where the low-pass filter is used to block the upper sideband of the mixing product. Subharmonic mixers have also been used to lower the required reference frequency [20, 21].

Self-phased antennas for communication

The simple phase conjugation of the RX wave merely reflects the RX information back to its source. In order to send the desired data using the TX wave, the phase of the RX carrier signal at each antenna element must be extracted first (Figure1.9). Then, the extracted carrier at each antenna element is phase conjugated and passed to a modulator to create a TX signal. The extracted RX carrier is also used to demodulate (or simply down-converted to baseband) the RX signal as shown in Figure1.9. Note that at each antenna element, the RX signal is demodulated using its extracted carrier, therefore, all the demodulated signals will be in-phase together and will coherently combine to create the final RX data.

The process of extracting the RX carrier phase depends on the modulation scheme of the RX wave and it can be very complex for phase modulated signals. For example, in [22], the carrier of the AM modulated RX signal is extracted by a simple clipper (Figure 1.10). However, this process is more complicated for phase modulated signals. For instance, in [23], the BPSK modulated RX signal is converted to the baseband at each antenna element,

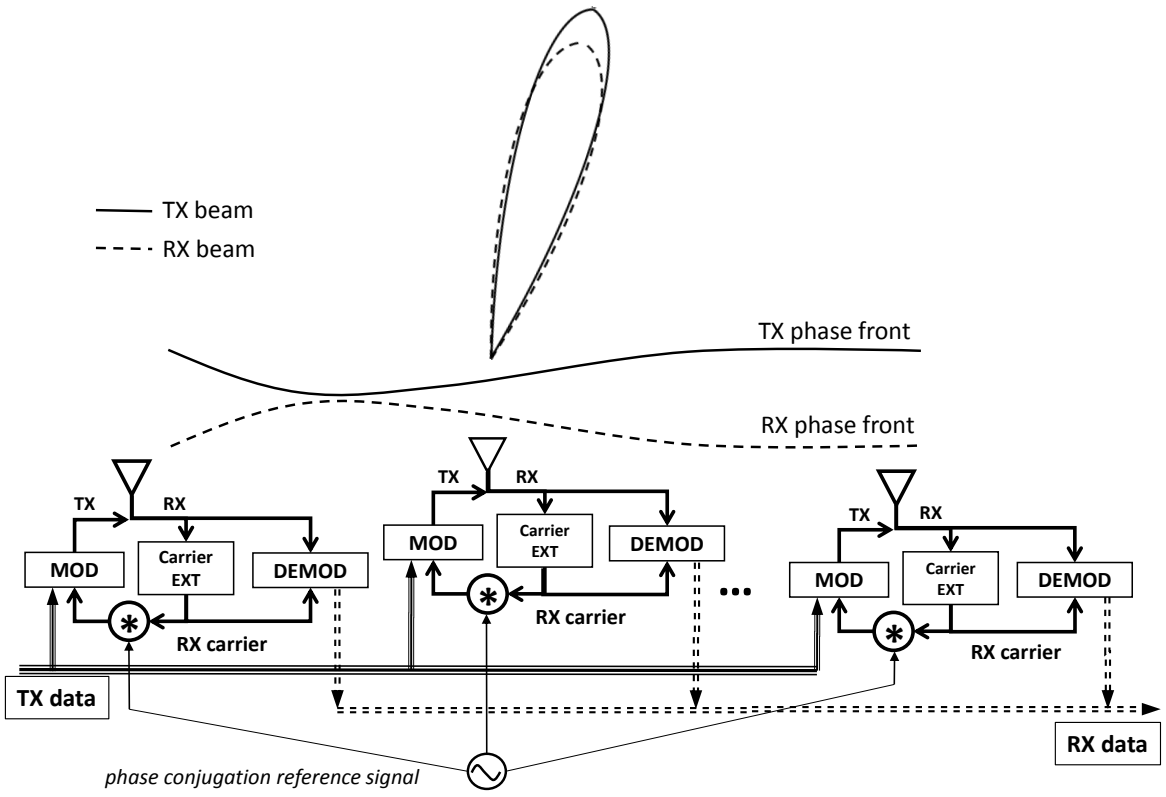

Figure 1.9: Self-phased array with carrier extraction to send desired TX data.

then the phase modulation of the BPSK data is removed by a digital processor to extract the phase of the RX carrier (see Figure 1.11).

Another approach to extract the RX carrier is to lock on the RX carrier using a tracking Phased Locked Loop (PLL). As an example, let us review the operation of a tracking PLL used in [13]. As shown in Figure 1.12, the VCXO2 is in a phased locked loop. The loop is designed in such a way that under the lock condition the phase difference between VCXO2 and LO oscillators is equal to the phase difference between the RX carrier at elements 1 and 2. In other words, the VCXO2 phase-locks on the RX carrier phase at element 2 with respect to the RX carrier phase at element 1. Then, the extracted carriers (outputs of LO and VCXO2) are phase conjugated and used for transmitting the TX data.

The phase detector in Figure 1.12 compares the phase of the RX signals from element 2 and 1. Since they both carry the same *data phase*, here caused by a QPSK modulation, the output of the phase detector will be proportional to the phase difference between the

RX carrier signals at element 1 and 2, and the *data phase* will have no effect. In addition to the complexity of the circuit, locking on a very low power signal received at one antenna element is very challenging. The VCOs at the different antenna elements may also be injection locked together due to unwanted coupling, especially in a larger array with high scan angles.

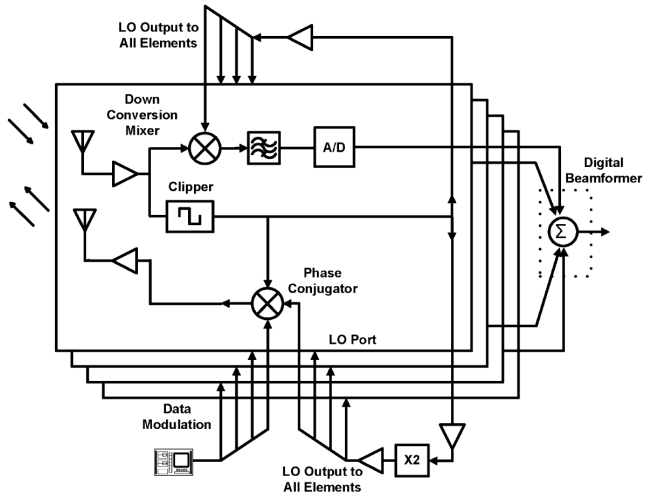

Figure 1.10: Self-phased antenna with carrier extraction of AM modulated RX signal. [22].

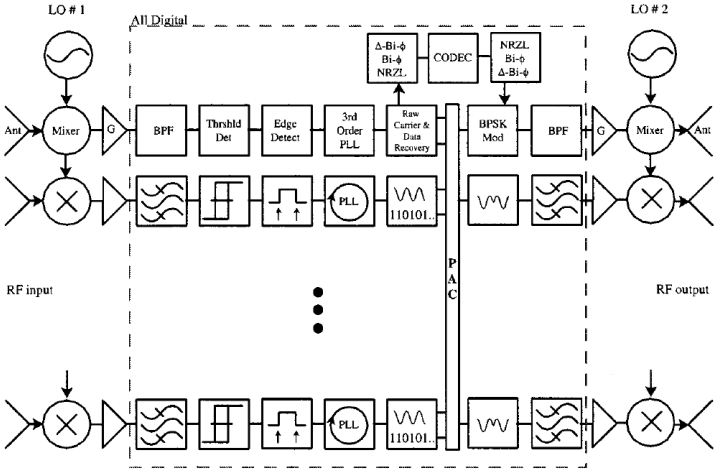

Figure 1.11: Self-phased array based on carrier extraction of BPSK modulated RX signal.[23].

As for the above examples, all self-phased antennas rely on the RX wave to generate a TX wave. Therefore, their performance is determined by the quality of the RX wave and

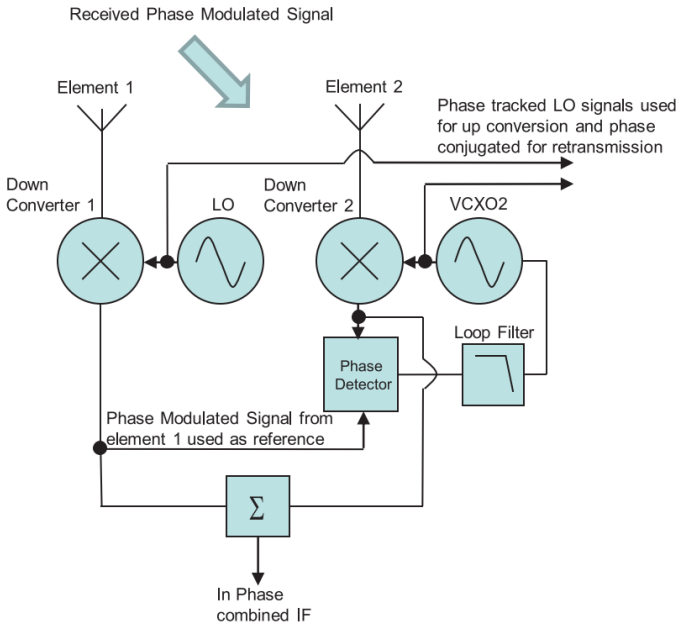

Figure 1.12: Diagram of tracking PLL to extract RX carrier in a self-phased array [13].

a transmission without reception is not possible. Moreover, depending on their specific architecture, they have one or more of the following limitations: (i) the antenna can only handle certain modulation schemes, (ii) the RX and TX frequencies should be identical or very close to each other to avoid beam misalignment, (iii) usually, the level of the RX signal at one antenna element is very small resulting in inaccurate and noisy carrier extraction.

1.2.3 Other antennas for adaptive antenna implementation

Mechanically-steered antennas

The simplest solution for an adaptive antenna is a mechanically-steered antenna that can be pointed to the desired direction. The antenna itself can be a reflector or a fixed-beam array antenna (see the examples in Figure 1.13). A reflector antenna can operate over a very large frequency span while its main lobe stays in the same direction. Therefore, such an antenna can be easily used for applications in which the TX and RX frequencies are far apart. On the other hand, fixed-beam array antennas are usually designed to operate at multiple frequency bands.

Figure 1.13: Mechanically-steered antennas developed by ViaSat [24]

In contrast to the relatively simple antenna part, a sophisticated mechanical assembly and control system is required for accurate mechanical steering. Mechanical-steering systems are bulky, have a longer response time in general, and are susceptible to mechanical failure. It is also worth noting that a mechanically-steered antenna can only perform single beamsteering, whereas a phased array antenna is able to generate complex multi-beam radiation patterns.

Fully passive phased array antennas

The structure of a fully passive phased array is shown in Figure 1.14. The phase shifters are passive, hence bi-directional, allowing for simultaneous transmission and reception. To have the TX and RX aligned together, the phase shifters must act as true-delay-lines, meaning their phase-frequency responses are linear over the RX to TX frequency range. Beamforming algorithms for a fully passive phase shifter can be very simple. It is only required to optimize the RX beam(s) and the TX ones follow naturally.

Low-loss and wide-band passive phase shifters are the key components in the above-mentioned antennas. However, phase shifter losses can limit the achievable G/T[1] and EIRP[2] of the antenna, and developing such phase shifters become more challenging at

[1]Gain over noise temperature
[2]Effective isotropic radiated power

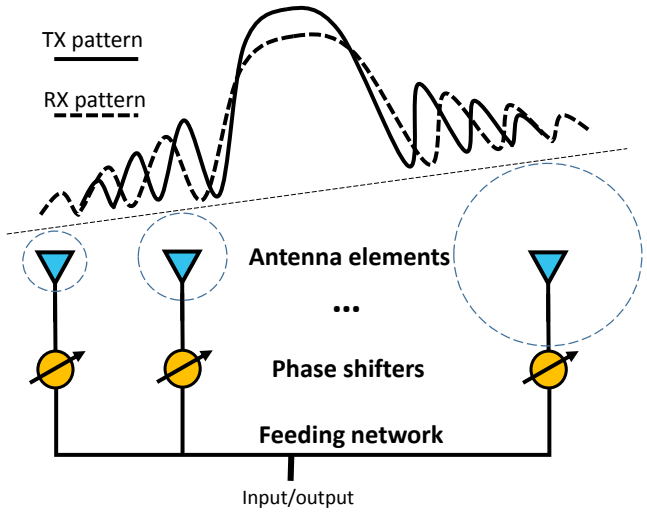

Figure 1.14: Fully passive phased array.

higher frequencies. It worth noting that a passive phase shifter not only attenuates the signal passing through it but also adds noise to the signal. For a phase shifter with L dB insertion loss, the noise figure is also L dB, [25], resulting in a two-fold decrease in the G/T of the antenna. Therefore, in comparison with conventional phased arrays that use low noise amplifiers (adding gain and suppressing the phase shifter noise figure), the G/T of a comparable fully passive phased array is much lower. Furthermore, the insertion loss of the phase shifter should be approximately constant for different values of phase shifts. Otherwise, an unwanted amplitude tapering over the antenna aperture would occur, distorting the radiation patterns.

There is ongoing research activities to develop both on-chip, [26], and off-chip low-loss and wide-band phase shifters [27], suitable for implementing a fully passive phased array for certain applications.

1.3 Active phased array (APA) antennas

As mentioned before, the antenna part of an adaptive antenna system is usually an active phased array (APA) antenna. In general, both the phase and amplitude of each antenna element of an APA can be controlled to generate various radiation patterns. The direction of maximum radiation is determined mostly by the phases of the antenna elements;

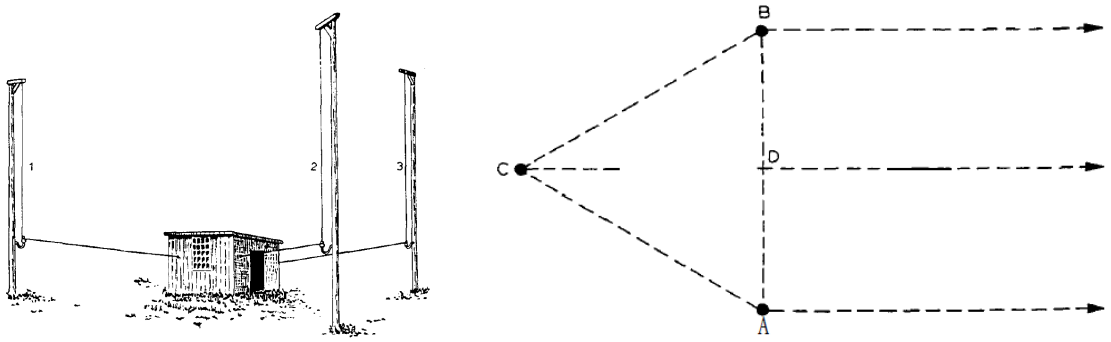

Figure 1.15: First active phased array antenna demonstrated in 1905 [28]. Left: outdoor assembly of three antenna elements. Right: top view of the antenna elements.

other parameters of the pattern, such as side-lobe-level, are determined by the elements amplitudes. In this section, the general structure, theory of operation, and implementation techniques of APAs are reviewed.

1.3.1 General structure of APA antennas

Practical beam steering with a phased array antenna was first demonstrated by Karl F. Braun in 1905 [28]. His phased array antenna was comprised of three antenna elements located at the corners of an equilateral triangle as shown in Figure 1.15. The antennas A and B are in-phase but antenna C is a quarter of a cycle phase delayed. Since the distance from antenna C to point D is chosen to be a quarter of the wavelength, the waves radiated by all antennas arrive at the same time at line A-B, forming an enhanced radiation along C-D line. By switching the quarter cycle phase delay between antennas, Braun was able to rotate the direction of maximum radiation 360° with 60° steps. After World War II, APAs were developed more intensively for radar applications, replacing slow mechanically-steered antennas with fast electronically-scanning APAs.

The conceptual structure of a modern APA is shown in Figure 1.16. By controlling the phase and amplitude of each antenna element, it is possible to generate various field distributions over the aperture of the array, each corresponding to a different radiation pattern. For example, a linear phase progression over the antenna array aperture steers the main lobe of the radiation pattern to a certain angle, and a uniform amplitude distribution over the aperture sets the side-lobe-levels $-13\,\mathrm{dB}$ below the main beam.

Despite their relatively simple operation, APAs are challenging to implement in prac-

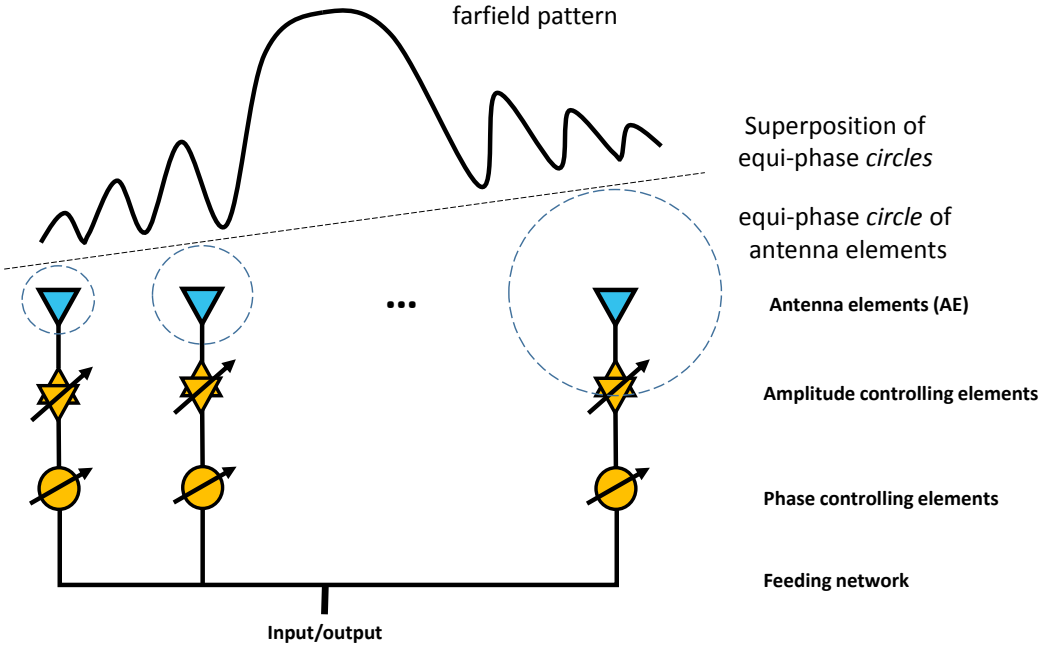

Figure 1.16: Conceptual diagram of a modern phased array antenna.

tice. The large number of antenna elements and related circuits (e.g. low noise amplifiers, power amplifiers, and phase shifters) must be integrated into tight spacing and fed by a feed network. Furthermore, to overcome unwanted mutual coupling between the antenna elements and electronic component imperfections, a calibration system may be required. However, the advancement of microwave monolithic circuit technology and digital signal processing has made it possible to develop APAs at lower costs for commercial applications.

1.3.2 Theory of operation of APA antennas

To analyze a phased array antenna, let us consider the arrangement of M antenna elements as shown in Figure 1.17. The following analysis is performed for transmitting antennas, but it can be shown that the same results will be true for receiving antennas, according to the reciprocity theorem [29].

Assuming the pattern of each antenna element is known, the electric field of the m^{th} antenna element can be represented by its effective length vector at far-field [29],

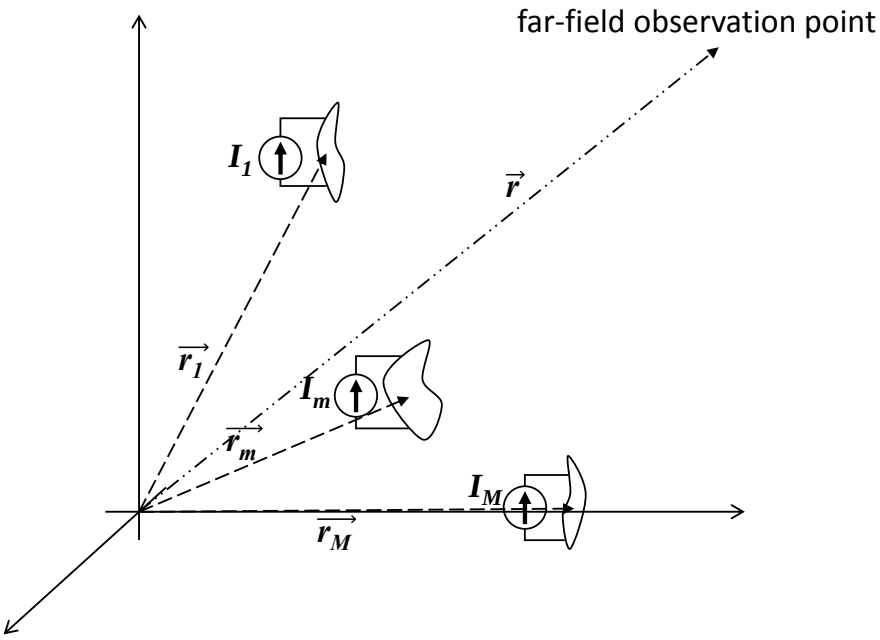

Figure 1.17: General configuration of a phased array antenna.

$$\mathbf{E_m} = jk\eta \frac{e^{jkr}}{4\pi r} \ell_{m(\hat{\mathbf{a}}_r)} I_m e^{jk\hat{\mathbf{a}}_r \cdot \mathbf{r}_m} \tag{1.4}$$

where $\hat{\mathbf{a}}_r$ is the radial unit vector of the coordinate system, $\ell_{m(\hat{\mathbf{a}}_r)}$ is the effective vector length of m^{th} antenna element, I_m is the phasor of the excitation current injected to the m^{th} element, and k and η are the propagation constant and impedance of free space, respectively.

Note that the patterns of the antenna elements in the array can be different from their patterns as stand-alone antennas due to mutual coupling between them. For simplicity, assume all antenna elements have the same effective length vector, $\ell_{m(\hat{\mathbf{a}}_r)} = \ell_{(\hat{\mathbf{a}}_r)}$. Given that the propagation environment (e.g. free space or air) is linear, the total electric field radiated by the antenna array is simply the summation of the field of each antenna element. Therefore, the electric field of the whole array at far-field is,

$$\mathbf{E} = \sum_{m=1}^{N} \mathbf{E_m} = \underbrace{jk\eta \frac{e^{jkr}}{4\pi r} \ell_{(\hat{\mathbf{a}}_r)}}_{\text{EP}} \underbrace{\sum_{m=1}^{N} I_m e^{jk\hat{\mathbf{a}}_r \cdot \mathbf{r}_m}}_{\text{AF}} . \tag{1.5}$$

The first part in (1.5) is in fact the antenna elements' radiation pattern, known as element pattern (EP). The summation in (1.5) is referred to as the array factor (AF), and shows the contribution of the array excitation coefficient, I_m currents, and the phase shift caused by the displacement of antenna elements, $e^{jk\hat{\mathbf{a}}_r.\mathbf{r}_m}$, to the total electric field along a certain direction, $\hat{\mathbf{a}}_r$.

Mathematically, AF is a summation of the complex numbers; hence, its magnitude is maximized when all of the complex numbers have the same phase. Therefore, one can choose the complex excitation coefficients, I_m, in such a way that they cancel the phases caused by the element displacements, $e^{jk\hat{\mathbf{a}}_r.\mathbf{r}_m}$. This maximizes the radiation along $\hat{\mathbf{a}}_r$.

The AF summation can be also be interpreted as a discrete Fourier transform of excitation currents, I_m s, with $e^{jk\hat{\mathbf{a}}_r.\mathbf{r}_m}$ as the basis functions. The Fourier transformation transforms spatial distribution of excitation currents to the far-field spatial field distribution. This interpretation is helpful for the synthesis of excitation coefficients for a given AF.

Yet another way of looking at an array antenna is as a spatial sampler of the electromagnetic fields. In the receiving mode, the array that samples the electromagnetic field over the aperture and in the transmitting mode generates a sampled version of the field over the aperture. Similar to the Nyquist sampling theorem in signal processing, if the distance between the consecutive samples (i.e. the inter-element distance) is smaller than a certain value, the samples can represent a continuous field over the antenna aperture. If not, an aliasing can occur that causes the emergence of grating lobes in the antenna far-field radiation pattern. For a linear array with inter-element distance d, operating at wavelength λ, with the off broadside scan angle θ_0, grating lobes appear at θ_{GL}, [30], where,

$$\frac{d}{\lambda} = \frac{n}{\sin(\theta_0) - \sin(\theta_{GL})},\ n = 1, 2, 3, ... \tag{1.6}$$

Depending on the parameters, several real values for θ_{GL} may exist, meaning that the radiation pattern exhibits peaks at those θ_{GL} (i.e. grating lobes), in addition to a peak at its scan angle θ_0. If no real values for θ_{GL} can be found, the pattern will be free of grating lobes for scan angles from 0 to θ_0. Figure 1.18 shows how the grating lobe angle changes with different scan angles and inter-element spacings. For example, for grating-lobe-free operation with maximum scan angle $\theta_0 = 90°$, the inter-element spacing should be smaller than $\lambda/2$.

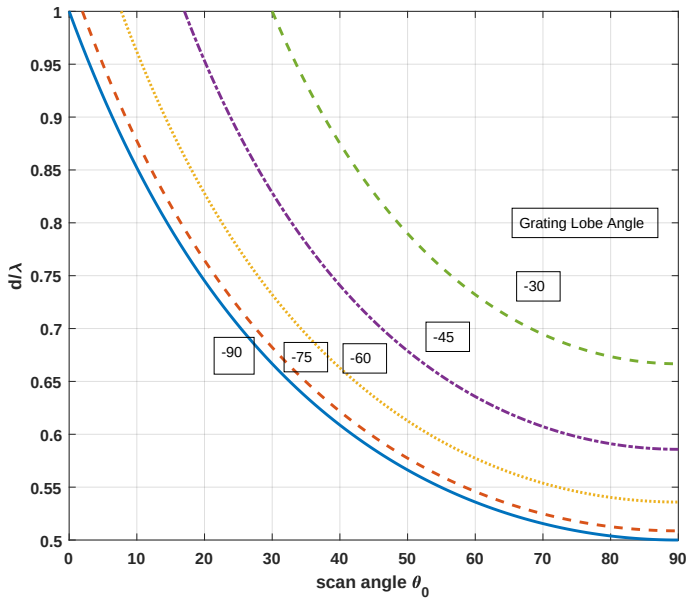

Figure 1.18: Grating lobe angles versus scan angle and inter-element spacing (recreated from [30]).

1.3.3 Implementation of APA antennas

According to (1.5), creating the complex excitation coefficients I_m and the summation are the two basic operations required to implement an APA. To create a complex I_m, a phase shifting mechanism is required in a part of the transceiver; it can be located in the RF, LO, IF, or even digital domains, as depicted in Figure 1.19. Depending on the application and the frequency of operation, one architecture may be more suitable than another. Note that Figure 1.19 shows a receiving APA implementation; similar structures can be used to implement a transmitting APA antenna.

In RF phase shifting, the beam is formed before the mixer; therefore, the interferences can be well suppressed before mixing. This property relaxes the dynamic range requirement on the mixer compared to the other architectures. On the other hand, the phase shifters contribute directly to the total noise temperature of the antenna in receiving mode. Therefore, it is preferable to use a low-noise phase shifter or to employ low noise amplifiers before the phase shifters. Furthermore, both in transmit and receive modes, the loss of the high-frequency RF phase shifters can vary at different phase shift states. High levels of loss variation should be compensated for by using variable gain amplifiers; if

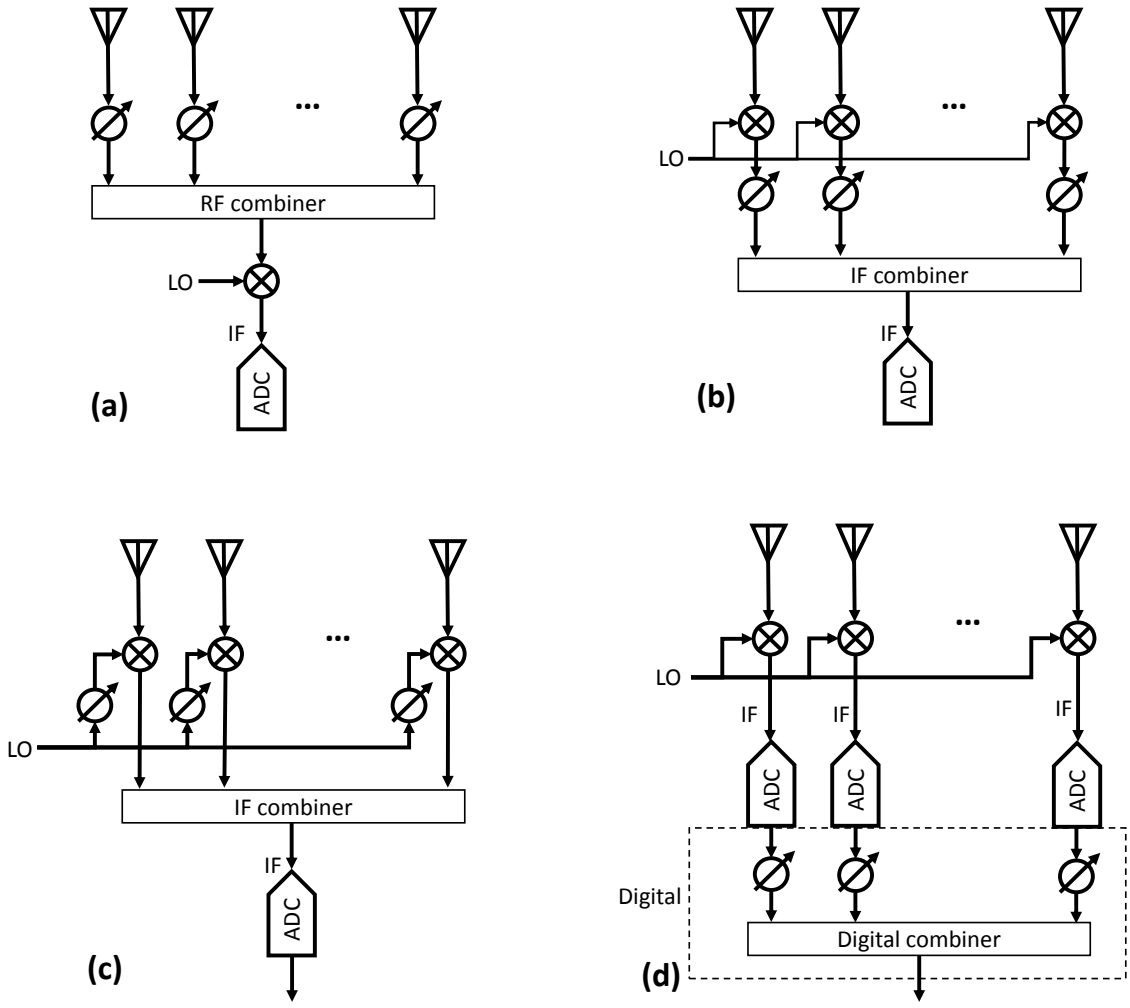

Figure 1.19: Four main categories of active phased array implementation. (a) RF phase shifting, (b) IF phase shifting, (c) LO phase shifting, and (d) Digital phase shifting.

not, the sidelobe level of the radiation pattern becomes dependent on the scan angle and pattern deformation may occur.

Alternatively, the phase shifting can be performed at lower IF frequencies where phase shifters with lower noise figures and lower loss variation are available. However, in this case, the mixers should have a larger dynamic range as the beam is formed after the mixers so more interferers and blockers are allowed to enter the mixers.

As displayed in Figure 1.19 (c), the phase shifts can be applied to the signals by the LO signals. During the mixing process, the phase of the LO signals adds to (or subtracts from) the RF signal; therefore, one can place the phase shifters in the path of the LO distribution network. Since the LO signal is locally generated, its phase and amplitude can be well controlled. Furthermore, the LO signal is a single tone, which makes the design and implementation of the phase shifter easier. However, the dynamic range of the mixer is important as the beam is formed after the mixers.

Finally, the phase shifting can be performed in the digital domain as shown in Figure 1.19 (d). This architecture requires a dedicated digital receiver at each antenna element; hence, the array can be very complex, costly, and power hungry. However, it is the most flexible architecture since the phase shifting occurs in a software. Thanks to the flexibility of the software, a digital APA can be a multi-functional antenna and it can be easily reconfigured for various types of array processing (e.g. MIMO[1], null steering, beam steering, etc).

Apart from the four commonly used architectures shown in Figure 1.19, alternative architectures, phase shifting, and beamforming techniques have been proposed in the literature, a short list of which is given in Table 1.1.

1.4 Conclusion

Adaptive antennas can greatly improve the performance of a wireless communication system by compensating for wireless channel impairments. Conventional approaches for implementing adaptive antennas are based on either DoA (direction-of-arrival) or self-phasing. The former relies on a well-defined incoming wave DoA that may not exist in an environment with strong multipath reflections, and usually requires a complex calibration routine to correctly steer the beams. The latter relies on the received wave to generate a transmit wave that imposes several limitations as explained earlier.

[1]Multi Input Multi Output

Table 1.1: A non-exhaustive list of alternative architectures based on unconventional phase shifting and beamforming techniques.

Ref	Phase shifting/beamforming technique	Remarks	Main achievement(s)	year
[31]	4-bit RF switched phase shifter	60 GHz, four element chip	Integration technology development	2012
[32]	RF phase shifting	76 & 100 GHz, 16 elements, single die transceiver	Integration of circuits and feed on a single die	2014
[33]	Holographic beam generation	X band, 400 element spatial fed array	Large array implementation, RF 1-bit phase shifter	2013
[34]	Holographic beam generation	aperture antennas array controlled by MEMS/Liquid crystal switches	Ka-band holographic beam generation for satcom[1] (under development)	2015
[35]	Mechanically rotating dielectric disks	X to Q band, commercially available	Beam steering for satcom applications	2012
[36]	Positive/negative-refractive-index phase shifter	2.4 GHz, series fed array, CMOS phase shifter	Developing a new phase shifter	2009
[37]	Integrated optic RF phase shifter	3 GHz@10 GHz RF phase shifting APA	Developing a new phase shifting technique	1993
[38]	Moving dielectric slab on microstrip lines	10-21 GHz, 4 element RF phase shifting using only one dielectric slab	Developing a new phase shifting technique	2002
[39]	I/Q mixers	60 GHz, subharmonic coupled-oscillator transmit array	Implementing a new phased array architecture	2006
[40]	Voltage-controlled ferroelectric material	X-band, reconfigurable flat lens	Implementing a new phase shifting technique	1999
[41]	Switched beam antenna	Metallic micro-fluidic switches	Developing a new reconfigurable antenna	2013

In the next chapter, a novel retro-directive (RX and TX beams always aligned) phased array (RDPA) architecture is proposed. In contrast to DoA-based and self-phased antennas, an RDPA antenna does not require calibration; generating the TX carrier signals locally at each antenna element independently of the RX signal. RDPAs are able to handle TX and RX signals with arbitrary modulation schemes and frequencies. Furthermore, they are comprised of independent modules that can be placed in different arrangements without any hardware modification.

Chapter 2

A novel retro-directive phased array antenna architecture

This chapter presents a novel retro-directive (TX and RX beams always aligned) phased array (RDPA) architecture. In contrast to DoA-based and self-phased antennas, RDPA antennas do not require calibration: they generate TX carrier signals locally at each antenna element independently of the RX signal, and they are able to handle TX and RX signals with arbitrary modulation schemes and different frequencies. Furthermore, RDPAs are comprised of independent modules that can be placed in different arrangements without any hardware modification. The RDPA antenna architecture is also submitted to US patent office, [42], and IEEE Microwave Theory and Technique journal [43].

First, the general RDPA architecture and its system level design will be explained in section 2.1 and 2.2, respectively. Then, the effects of implementation inaccuracies on the performance of RDPA antennas are investigated through statistical analyses in section 2.3.

2.1 RDPA architecture

2.1.1 RDPA conceptual structure

Figure 2.1 shows the conceptual design of the proposed RDPA antenna system, including a group of antenna modules in which phase shifts are added to the waves exchanged between the two ends of the communication link (nodes A and B). In practice, node A is a part of the RDPA antenna; whereas, node B is a remote node (e.g. satellite).

The system employs an LO phase shifting technique [44] to add certain phase shifts to the TX and RX signals. The optimal values of these phase shifts result in a retro-directive beam pair pointed toward node B, consequently maximizing the transmission and reception between nodes A and B.

In the TX mode, node A broadcasts the TX signal to all modules at TX-IF frequency f'_{TX}. Then, a mixer in each module converts the TX-IF signal to a TX-RF signal at frequency f_{TX}, and transmits it to node B by an RF antenna element. Similarly, in the RX mode, the wave transmitted by node B reaches each antenna module at RX-RF frequency f_{RX}. Then, the RX-RF signal is converted to an RX-IF signal at frequency f'_{RX} by a different mixer, and the resultant signal is transmitted to node A through an IF antenna element.

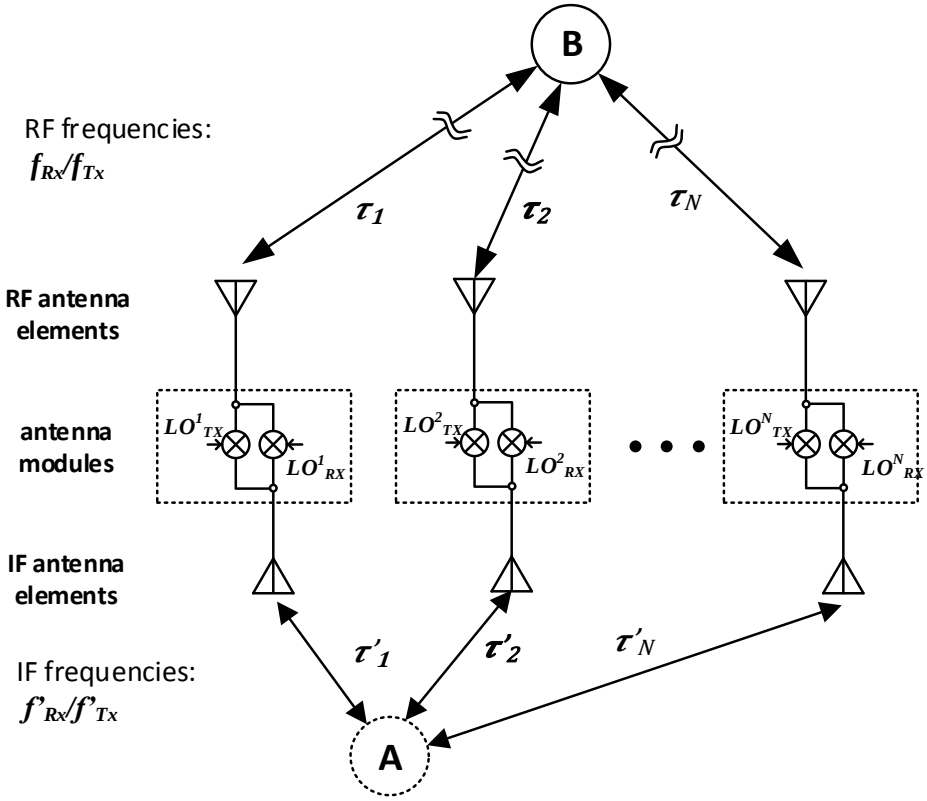

Figure 2.1: Conceptual configuration of proposed RDPA antenna system. Symbols τ_n and τ'_n are time delay between n^{th} RF and IF antenna elements and nodes A and B, respectively.

Let us define the n^{th} TX path from nodes A to B as the cascade of three segments: (i)

node A to the n^{th} IF antenna element, (ii) IF side of the n^{th} module to its RF side through the TX mixer, and (iii) the n^{th} RF antenna element to node B. Similarly, the n^{th} RX path from nodes B to A can be defined as a cascade of three segments: (i) node B to the n^{th} RF antenna element, (ii) RF side of the n^{th} module to its IF side through the RX mixer, and (iii) the n^{th} module IF antenna element to node A.

For maximum transmission from nodes A to B, the phase shift along all TX paths should be equal to a constant value. Similarly, for maximum reception from node B at node A, the phase shift of all RX paths should be equal to a constant. Mathematically, these two conditions can be expressed as follows:

$$TX:\ 2\pi f'_{TX}\tau'_n + \phi^n_{TX} + 2\pi f_{TX}\tau_n = \theta_{TX}\ \ n = 1:N \tag{2.1a}$$

$$RX:\ 2\pi f'_{RX}\tau'_n + \phi^n_{RX} + 2\pi f_{RX}\tau_n = \theta_{RX}\ \ n = 1:N, \tag{2.1b}$$

where $2\pi f\tau$ is the phase shift associated with the time delay τ at frequency f, and ϕ^n_{TX} and ϕ^n_{RX} are the phase shifts added by the n^{th} module. The quantities θ_{TX} and θ_{RX} are constant phase shifts between nodes A and B, which can be assumed to be zero without losing generality. Hence, (2.1) can be rewritten as (2.2),

$$TX:\ \phi^n_{TX} = -2\pi(\tau'_n f'_{TX} + \tau_n f_{TX}) \tag{2.2a}$$

$$RX:\ \phi^n_{RX} = -2\pi(\tau'_n f'_{RX} + \tau_n f_{RX}). \tag{2.2b}$$

Any change in the relative positions of node A, the antenna modules, or node B, results in a change in τ_n and/or τ'_n that in turn changes the values of ϕ^n_{TX} and ϕ^n_{RX} required for optimal transmission and reception. Therefore, the antenna modules can be rearranged and the array itself will compensate for the extra time delays without requiring a hardware modification. The procedure for finding optimal ϕ^n_{RX} and ϕ^n_{TX} is presented next.

2.1.2 RDPA beamforming scheme

As explained in section 1, the RX signal can be used as feedback to find the set of optimal values for ϕ^n_{RX}, as in [11], but there is no such feedback in the transmission path. In the proposed RDPA antenna, this problem is solved simply by a proper choice of IF frequencies. Note that while the RF frequencies, f_{TX} and f_{RX}, are given by the required operational

frequencies of the antenna, the IF frequencies, f'_{TX} and f'_{RX}, can be chosen arbitrarily. If f'_{TX} and f'_{RX} are chosen such that,

$$\frac{f_{TX}}{f_{RX}} = \frac{f'_{TX}}{f'_{RX}}, \tag{2.3}$$

then from (2.2) it can be concluded that,

$$\phi^n_{TX} = \frac{f_{TX}}{f_{RX}}\phi^n_{RX}. \tag{2.4}$$

Equation (2.4) states that the optimal values for ϕ^n_{TX} are proportional to the optimal values of ϕ^n_{RX} by a constant factor, independent of τ_n and τ'_n. Therefore, once the optimal ϕ^n_{RX} are reached in reception, it is only necessary to maintain the phase ratio of (2.4) in order to assure maximum transmission.

It is worth noting that no knowledge about the actual values of ϕ^n_{RX} or ϕ^n_{TX} are required to maximize the transmission and reception. This property greatly reduces the complexity of the TX beamforming and results in the advantages described in section 1. Specifically, there is no need for calibration or characterization of the antenna because the optimal values of ϕ^n_{RX} are directly used to find optimal values of ϕ^n_{TX}. In DoA-based antennas, however, the optimal ϕ^n_{RX} are first translated into a DoA, and then that estimated DoA is translated into the optimal set of values for ϕ^n_{TX}.

The following section details the internal structure of an antenna module in which the phase relation (2.4) is maintained for all values of ϕ^n_{RX}.

2.2 RDPA system-level design

Figure 2.2 displays a block diagram of the proposed RDPA antenna. All antenna modules receive a synchronizing signal, LO_C, from the common LO source, and a PHASE[n] control command. The RX beam controller monitors the final RX signal at node A and accordingly generates a set of phase control commands PHASE[1:N] for the antenna modules. The RF and IF antenna elements on both sides of the modules are dual-band antennas operating at f_{TX}/f_{RX} and f'_{TX}/f'_{RX}, respectively. Note that the RX beam controller can accept a "Node B Select" command to identify the desired node B when there are more than one (e.g. selecting a specific satellite from a constellation).

Figure 2.3 shows an antenna module's internal structure. The left and right diplexers split/combine the two IF signals and the two RF signals, respectively. The TX-IF signal

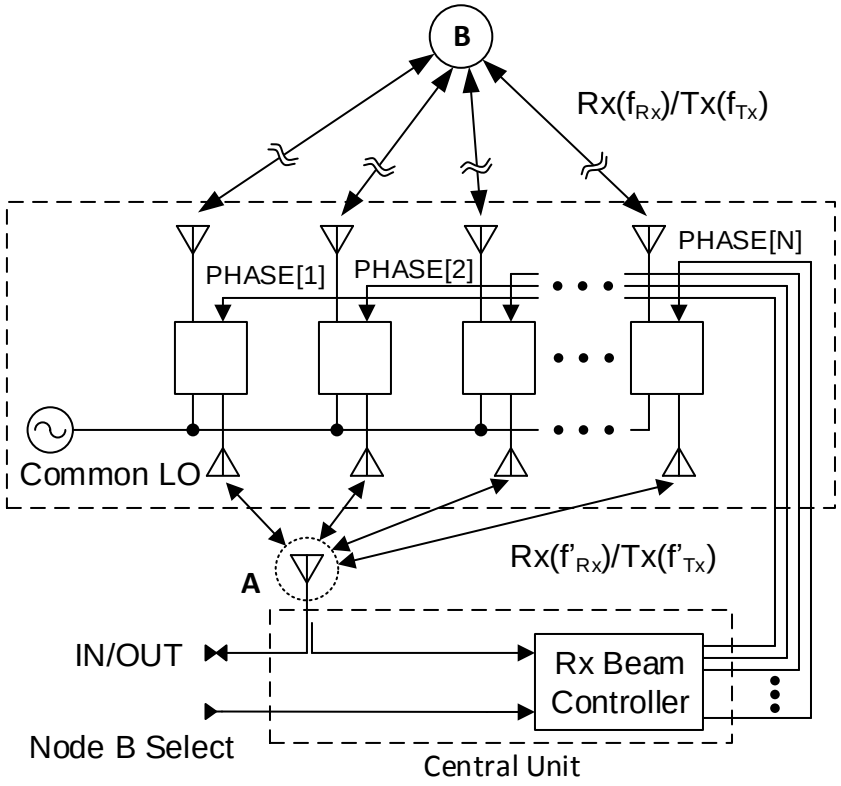

Figure 2.2: System-level block diagram of proposed RDPA antenna system.

passes through the upper branch mixer where its carrier frequency is converted from f'_{TX} to f_{TX}. Similarly, the RX-RF signal passes through the lower branch mixer and its carrier frequency is converted from f_{RX} to f'_{RX}. The LO_{TX} and LO_{RX} signals at each module are generated from LO_C by an LO generator block, explained in detail in section 2.2.2.

As shown in Figure 2.2 and 2.3, all antenna modules are fed by a common LO signal from which the LO_{RX} and LO_{TX} signals are generated. To provide a common phase reference to all antenna modules, the samples of the common LO signal arriving at each module must be phase synchronized together.

It is worth mentioning that the combination of a diplexer and a dual-band antenna at either side of the antenna module can be replaced by two separate single-band antennas: one for TX and one for RX. As long as the inter-elemental spacing between the TX antenna elements is the same as that of the RX elements, the RDPA array's behavior will not change.

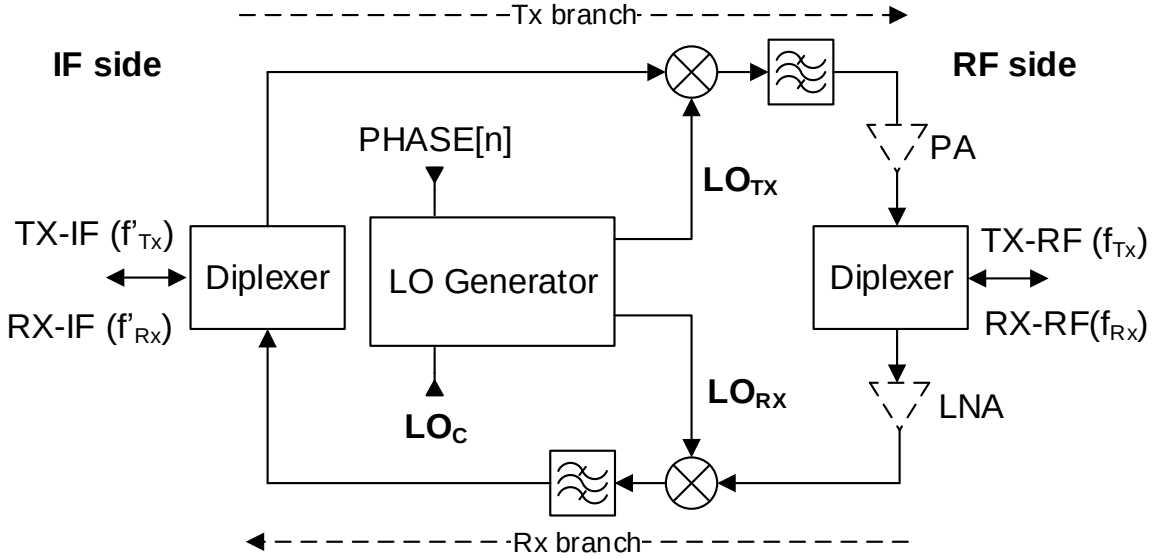

Figure 2.3: Block diagram of antenna module (LNA and PA are optional).

2.2.1 LO_{TX} and LO_{RX} required for maximum transmission and reception

To achieve maximum transmission and reception, the frequencies and the phases of the LO_{RX} and LO_{TX} signals must be the values given in Tables 2.1 and 2.2 (see App.A for LSB2 case). The frequencies of the LO_{RX} and LO_{TX} signals are determined by the required frequency translations ($f'_{TX} \leftrightarrow f_{TX}$ and $f'_{RX} \leftrightarrow f_{RX}$); their phases, ϕ^n_{LOTX} and ϕ^n_{LORX}, are determined according to the phases to be added to the RX and TX signals, ϕ^n_{TX} and ϕ^n_{RX} (2.2).

Note that the phase and frequency of a mixer's LO signal are added to those of the mixer's input to create the upper sideband (USB) of the output; a similar subtraction generates the lower sideband (LSB). The filters in the TX and RX branches of the antenna modules in Figure 2.3, allow for the selection of one of the sidebands. Therefore, depending on the chosen sideband, the phase and frequency of the LO signals will be one of the three cases listed in Tables 2.1 and 2.2. Any combination of f_{LOTX}/ϕ_{LOTX} and f_{LORX}/ϕ_{LORX} from these tables (i.e. one of nine possibile combinations), ensures maximum transmission and reception between nodes A and B.

Table 2.1: Required LO_{TX} for maximum transmission and reception

TX	$\boldsymbol{f_{LOTX}}$	$\boldsymbol{\phi^n_{LOTX}}$
USB	$f_{TX} - f'_{TX}$	$\phi^n_{TX} = 2\pi(\tau'_n f'_{TX} + \tau_n f_{TX})$
LBS1	$f'_{TX} - f_{TX}$	$-\phi^n_{TX} = -2\pi(\tau'_n f'_{TX} + \tau_n f_{TX})$
LBS2	$f_{TX} + f'_{TX}$	$\phi^n_{TX} + 4\pi\tau'_n f'_{TX} = 2\pi(\tau'_n f'_{TX} - \tau_n f_{TX})$

USB:$f_{LOTX} < f_{TX}$ & $f'_{TX} < f_{TX}$, LBS1:$f_{LOTX} < f'_{TX}$,
LBS2:$f_{LOTX} > f'_{TX}$

Table 2.2: Required LO_{RX} for maximum transmission and reception

RX	$\boldsymbol{f_{LORX}}$	$\boldsymbol{\phi^n_{LORX}}$
USB	$f'_{RX} - f_{RX}$	$\phi^n_{RX} = 2\pi(\tau'_n f'_{RX} + \tau_n f_{RX})$
LBS1	$f_{RX} - f'_{RX}$	$-\phi^n_{RX} = -2\pi(\tau'_n f'_{RX} + \tau_n f_{RX})$
LBS2	$f_{RX} + f'_{RX}$	$\phi^n_{RX} + 4\pi\tau_n f_{RX} = 2\pi(-\tau'_n f'_{RX} + \tau_n f_{RX})$

USB:$f_{LORX} < f_{RX}$ & $f'_{RX} < f_{RX}$, LBS1:$f_{LORX} < f_{RX}$,
LBS2:$f_{LORX} > f_{RX}$

2.2.2 LO generator circuit

To generate the LO signals given in Tables 2.1 and 2.2, the LO generator circuit shown in Figure 2.4 is devised. The LO generator accepts the common LO signal, LO_C, at frequency

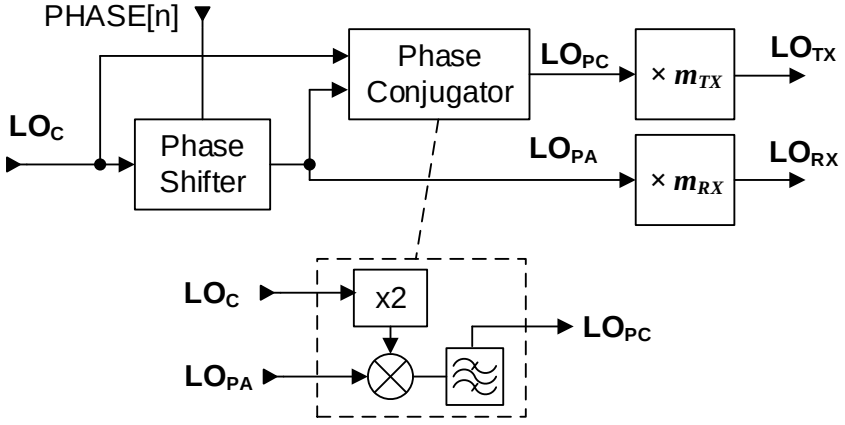

Figure 2.4: LO generating circuit which generates LO_{TX} and LO_{RX} from a single source using a single phase shifter.

f_0 and phase zero. Then, the phase shifter adds a phase shift, ϕ_p^n, to it to create LO_{PA}. In the lower branch, LO_{PA} passes through a $\times m_{RX}$ frequency multiplier to create LO_{RX}. In the upper branch, LO_{PA} first undergoes phase conjugation (flipping the phase shift from ϕ_p^n to $-\phi_p^n$) to create LO_{PC}, and then passes through the frequency multiplier ($\times m_{TX}$) to create LO_{TX}. Mathematically, the LO signals are:

$$\begin{array}{c|cc} & \text{frequency} & \text{phase} \\ \hline LO_{TX} & m_{TX} f_0 & -m_{TX}\phi_p^n \\ LO_{RX} & m_{RX} f_0 & m_{RX}\phi_p^n \end{array} \tag{2.5}$$

The phase conjugator consists of a mixer, a frequency doubler, and a low pass filter that blocks the USB of the mixing products. This structure is known as a heterodyne phase conjugator (see 1.2.2). The phase conjugation can be performed either in the generation of LO_{TX} or LO_{RX}, and is necessary for retro-directive operation of the antenna system.

Comparing the outputs of the LO generator circuit given in (2.5), to the nine possible mixer mode combinations given in Tables 2.1 and 2.2, shows that only two combinations [shown in (2.6)], allow for a physical implementation of the LO generator circuit. The eight

other combinations require either zero f_0 or negative m_{TX}, m_{RX}.

$$\begin{aligned}
&\text{TX (USB)}: \begin{cases} m_{TX} f_0 = f_{TX} - f'_{TX} \\ m_{TX} \phi_n^p = -2\pi(\tau'_n f'_{TX} + \tau_n f_{TX}) \end{cases} \\
&\text{RX (LSB1)}: \begin{cases} m_{RX} f_0 = f_{RX} - f'_{RX} \\ m_{RX} \phi_n^p = -2\pi(\tau'_n f'_{RX} + \tau_n f_{RX}) \end{cases}
\end{aligned} \tag{2.6a}$$

$$\begin{aligned}
&\text{TX (LSB1)}: \begin{cases} m_{TX} f_0 = f'_{TX} - f_{TX} \\ m_{TX} \phi_n^p = 2\pi(\tau'_n f'_{TX} + \tau_n f_{TX}) \end{cases} \\
&\text{RX (USB)}: \begin{cases} m_{RX} f_0 = f'_{RX} - f_{RX} \\ m_{RX} \phi_n^p = 2\pi(\tau'_n f'_{RX} + \tau_n f_{RX}) \end{cases}
\end{aligned} \tag{2.6b}$$

In each case of (2.6), if the TX phase expressions are divided by the RX phase expressions and the frequency ratio condition (2.3) is applied, the following expression of the frequency multiplication factors can be deduced:

$$\frac{m_{TX}}{m_{RX}} = \frac{f_{TX}}{f_{RX}} = \frac{f'_{TX}}{f'_{RX}}. \tag{2.7}$$

Equations (2.6) and (2.7) are the design equations needed for selecting the design parameters m_{TX}, m_{RX}, f'_{RX}, f'_{TX}, and f_0 for a given set of RF frequencies f_{TX}/f_{RX}. Note that these equations do not determine the design parameters uniquely; therefore, practical considerations can also be taken into account in choosing the final parameter values. Specifically, among the three cases in (2.6), (2.6a) results in the lowest IF frequencies, a potential practical advantage.

Design Example: For $f_{TX} = 3\,\text{GHz}$ and $f_{TX} = 2\,\text{GHz}$, using (2.7), the chosen values for m_{TX} and m_{RX} can be 3 and 2. The IF frequencies f'_{TX} and f'_{TX} should also be chosen with the same 3/2 ratio, such as 0.75 GHz and 0.5 GHz. Finally, the value of f_0 is determined by one of the cases in (2.6); for (2.6a) the f_0 is 0.75 GHz.

2.2.3 Synchronizing network

As mentioned above, the samples of the common LO signal arriving at each module must be phase synchronized. The simplest solution is to distribute the LO_C signal with a properly phased distribution network such as a corporate feed network. Alternatively, the LO_C

signal can be generated at each module with an oscillator that is phase synchronized with the other oscillators. Synchronizing the oscillators can be done through a low frequency reference signal; an easy approach to accurately distributing the signal between the antenna modules. In any case, a distribution network with the same delay from its input to all its outputs is required. In practice, however, each output may exhibit a different time delay due its different distance from the input.

The problem of different delays in conventional distribution networks is rooted in the fact that the signals are carried by a traveling wave along a piece of transmission line. For a standing wave, on the other hand, all points along the transmission line are either in-phase or anti- phase (see Figure 2.5) [45]. In the following section, a phase synchronizing network based on standing waves is explained. The main idea of this phase synchronizing network is proposed in [50].

Figure 2.5 shows a traveling wave and a standing wave in a transmission line at three different instants of time. It can be seen that the phase of the traveling wave changes with position, but the standing wave shows salphasic [1] behavior. To eliminate the 180° phase change, the length of the line can be limited to a half-wave length line, or the wave can be rectified.

In practice, however, a pure standing wave can be established only in a lossless line. Let us consider the terminated lossy transmission line in Figure 2.5 and analyze the phase of the voltage distribution. The total voltage in the line can be written as a summation of a forward traveling wave launched by the source and a backward traveling wave reflected by the termination [46]. In other words

$$V(z') = \widehat{V}\left(e^{\gamma z'} + \Gamma e^{-\gamma z'}\right) \tag{2.8}$$

where Γ and Γ_s are reflection coefficients at the load and source as defined in Figure 2.5, γ is the complex propagation constant of the line, and

$$\widehat{V} = \frac{Z_0}{Z_0 + Z_s} V_s \frac{1}{e^{\gamma l} - \Gamma\Gamma_s e^{-\gamma l}}.$$

The expression for $V(z')$ in (2.8) can be rearranged in the following form by replacing $\Gamma = |\Gamma| e^{j\angle\Gamma}$ and $\gamma = \alpha + j\beta$:

$$\begin{aligned} V(z') &= \widehat{V}\left(A^+ e^{j\beta z'} + A^- e^{-j\beta z'}\right) \\ A^+ &= e^{\alpha z'}, A^- = |\Gamma| e^{j\angle\Gamma} e^{-\alpha z'}. \end{aligned} \tag{2.9}$$

[1] A pattern of alternating in-phase and anti-phase regions

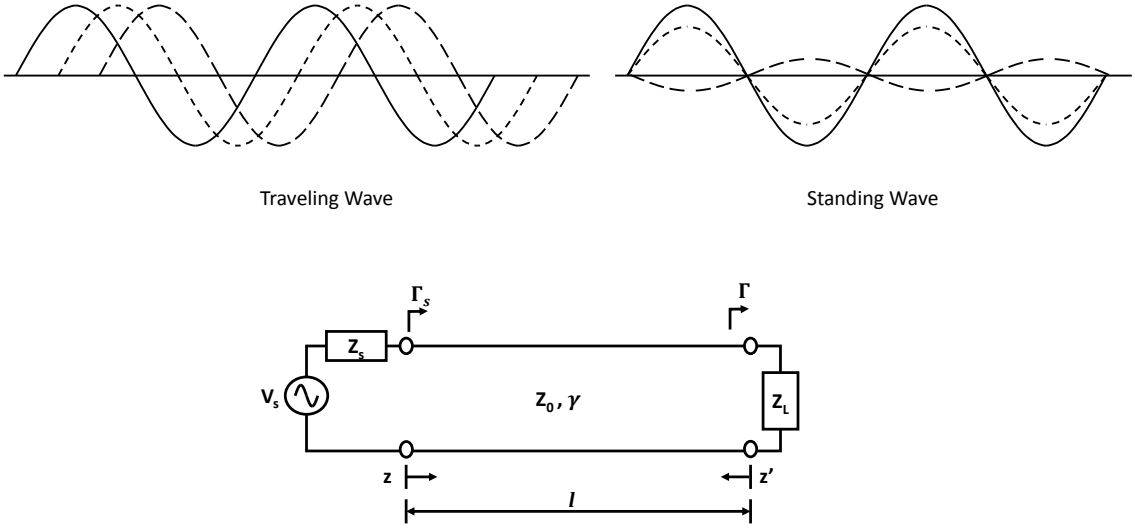

Figure 2.5: Top: Traveling and standing waveforms at different time snapshots along a transmission line. Bottom: Lossy transmission line terminated at one end and excited by a source at other end.

The voltage distribution in (2.9) can be rewritten as the summation of two terms: a standing wave term and a traveling wave term,

$$V(z') = \widehat{V}\big(\underbrace{A^+(e^{j\beta z'} + e^{-j\beta z'})}_{\text{standing wave}} + \underbrace{(A^- - A^+)e^{-j\beta z'}}_{\text{traveling wave}}\big). \tag{2.10}$$

In order to have a pure standing wave,

$$|A^+| = |A^-| \Rightarrow \alpha = 0, |\Gamma| = 1. \tag{2.11}$$

In other words, the load reflection coefficient must be unity and the transmission line must be lossless. The former condition can be easily satisfied with a high quality short circuit. For the latter, the line losses can be compensated for using the transconductance units embedded in the transmission line as shown in Figure 2.6. If the transconductance units are designed as amplifiers, their gain must be well controlled to compensate for the line losses without exceeding the losses. Alternatively, the transconductance units can be designed as oscillators. In this case, it is enough to have the linear transconductance value slightly higher than the line loss to ensure the oscillation starts. In the steady state regime, the transconductance becomes self-limited to a value exactly equal to the line loss

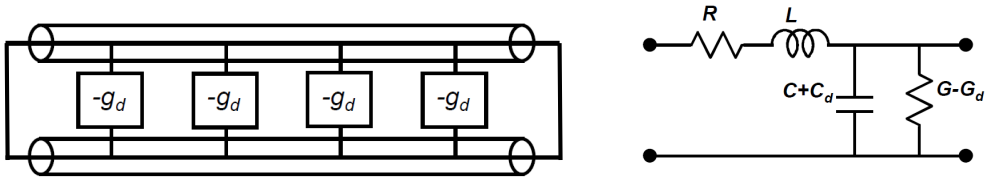

Figure 2.6: Compensating line losses by transconductance loading [47].

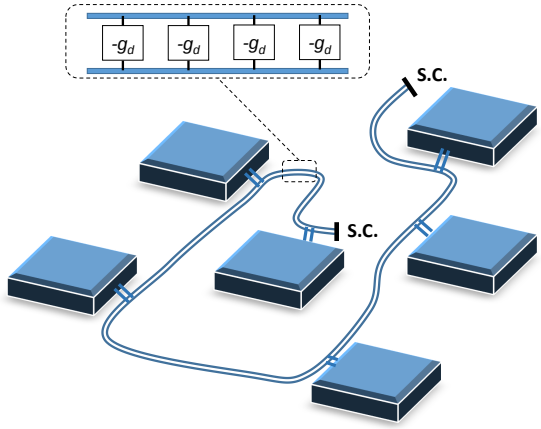

Figure 2.7: Using lossless terminated line as distributed oscillator to provide common LO signal to antenna modules in RDPA antenna.

[47]. Note that the separation between the transconductance loadings should be a fraction of a wavelength in order to form a uniform lossless transmission line.

The whole transmission line in Figure 2.6 acts as a distributed oscillator. It can be routed between the antenna modules, and will provide a signal phase reference independent of their location as depicted in Figure 2.7.

2.2.4 Performance of RDPA antennas with wide-band signals

In the last two sections, single-tone signals were used in the analysis of the RDPA antenna. In this section, the effects of a non-zero signal bandwidth on the performance of the array are investigated. According to (1.5) and Figure 1.17, the array factor of an N-element

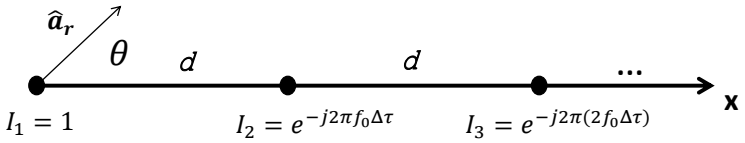

Figure 2.8: An RDPA in uniform linear array form.

array is,

$$AF = \sum_{n=1}^{N} I_n e^{j\frac{2\pi f}{c}\hat{\mathbf{a}}_r.\mathbf{r}_n}. \tag{2.12}$$

where $\hat{\mathbf{a}}_r$ is the radial unit vector of the coordinate system, $\mathbf{r}_n$ is the vector pointing to the n^{th} element location, and I_n is the complex excitation of the n^{th} element. Ideally, the complex excitation coefficient is created by passing a signal through a true delay line, mathematically delaying the waveform in time (i.e. $\cos(2\pi ft) \longrightarrow \cos(2\pi f(t-\tau)) = \cos(2\pi ft - 2\pi f\tau)$). Therefore, the ideal complex coefficient should be in the form of,

$$I_n = i_n e^{-2\pi f\tau_n}, \tag{2.13}$$

where τ_n is the delay of the signal at the n_{th} element. Therefore, the array factor in (2.12) can be rewritten as follows,

$$AF = \sum_{n=1}^{N} i_n e^{j\frac{2\pi f}{c}\hat{\mathbf{a}}_r.\mathbf{r}_n - 2\pi f\tau_n}. \tag{2.14}$$

Note that in the ideal case of (2.13), the phase of I_n is a linear function of the frequency. In the proposed RDPA architecture, however, the phase of I_n is fixed over the frequency,

$$I_n = i_n e^{-2\pi f_0\tau_n}, \tag{2.15}$$

where f_0 is the TX/RX frequency. To see the effect of such excitation more clearly, the array factor of an RDPA with a linear uniform array configuration can be written as shown in Figure 2.8. The element location vector is $\mathbf{r}_n = d(n-1)\hat{\mathbf{x}}$, $\hat{\mathbf{a}}_r = \sin\theta\cos\phi\hat{\mathbf{x}} + \sin\theta\sin\phi\hat{\mathbf{y}} + \cos\theta\hat{\mathbf{z}}$, and $I_n = i_n e^{-j2\pi f_0(n-1)\Delta\tau}$. Therefore, from (2.12) and (2.15), the array factor is,

$$AF = \sum_{n=1}^{N} i_n e^{j2\pi(n-1)(\frac{fd\sin(\theta)}{c} - f_0\Delta\tau)}. \tag{2.16}$$

The summation in (2.16) reaches its maximum when the phases of the terms $\frac{fd\sin(\theta)}{c} - f_0\Delta\tau$ are zero. Therefore, at frequency f_0, the value of $\Delta\tau$ should be equal to $\frac{d\sin(\theta_0)}{c}$ to create the scan angle θ_0; at the other frequencies, the scan angles are determined by the following equation,

$$\frac{fd\sin(\theta)}{c} = \frac{f_0 d\sin(\theta_0)}{c} \Longrightarrow \theta = \sin^{-1}(\frac{\sin(\theta_0)}{f/f_0}). \tag{2.17}$$

From (2.17), it is evident that for narrow-band signals ($\frac{f}{f_0} \simeq 1$), the actual beam angle is independent of the frequency (i.e. $\theta \simeq \theta_0$). For larger signal bandwidths, however, frequency beam scanning occurs, causing a scan angle deviation from the nominal angle, θ_0. Figure 2.9 shows this beam deviation as a function of the normalized frequency and the scan angle. For a fairly large instantaneous bandwidth of 10%, and at a large scan angle of 60°, the frequency scanning is around ±5° throughout the full frequency band; this may not be acceptable for some applications.

2.3 Effects of implementation inaccuracies on RDPA antenna performance

So far, it has been assumed that the antenna modules are identical and the ratio of the frequency multiplication factors are the same as the operating TX and RX frequency ratios. In practice, however, module-to-module variations and offsets in the frequency multiplication factors may occur, degrading the RDPA antenna performance. In the following sections, these implementation inaccuracy effects will be investigated.

2.3.1 Effect of module-to-module variations on RDPA performance

In reality, random variations between antenna modules may occur. Figure 2.10 shows three types of module-to-module variation, defined with respect to a reference module.

The first type of variation is a time delay difference between the IF and RF antenna elements and the antenna modules (i.e. $\triangle t_{IF}$ and $\triangle t_{RF}$). These time delays can be absorbed into τ_n and τ_n' in (2.1); therefore, not causing any problems in the operation of the RDPA.

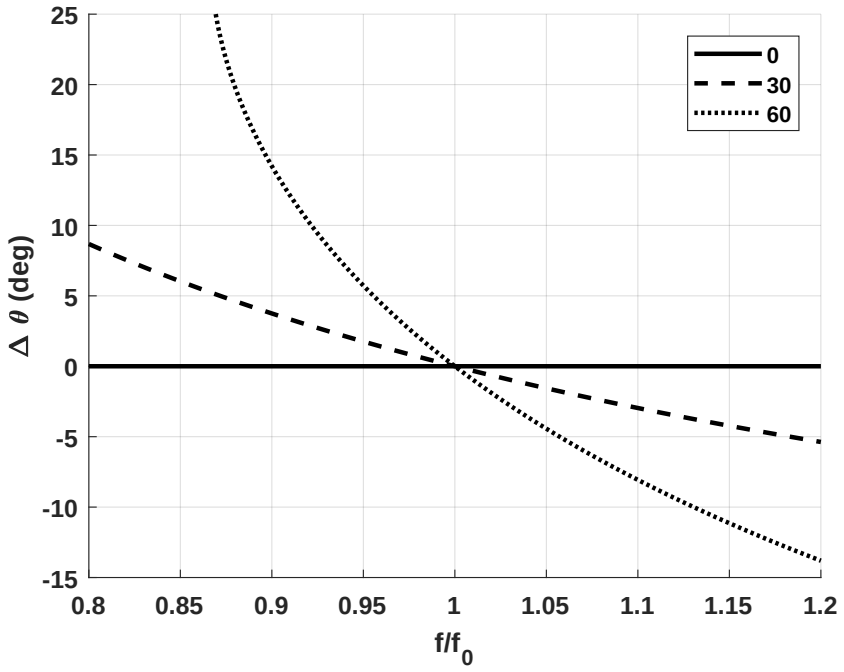

Figure 2.9: Undesired beam deviation caused by frequency scanning in RDPA with linear uniform array configuration. Solid line: scan angle $\theta_0 = 0$. Dashed line: scan angle $\theta_0 = 30$. Dotted line: scan angle $\theta_0 = 60$.

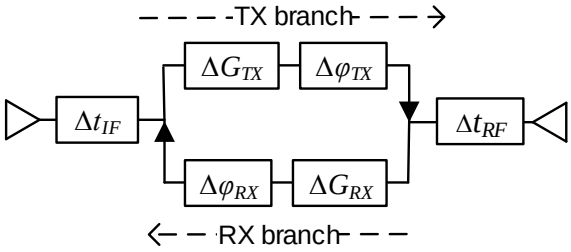

Figure 2.10: Antenna module with time and phase delay deviations.

The second type of variation is a gain variation in the TX and RX paths that causes random amplitude tapering over the antenna aperture. Such amplitude tapering has little effect on the direction of the main beam, but it can affect side-lobe-levels (SLLs) of the antenna. Fortunately, maintaining gain variations below a certain value is relatively simple.

The third type of variation is a phase difference between the TX and RX branches of an antenna module with respect to a reference module ($\triangle\phi_{RX}$ and $\triangle\phi_{TX}$ in Figure 2.10). These phase variations can cause undesirable effects and originate from uncertainties either in a module's implementation or in the in-phase distribution of the common LO signal between modules. The phase variations cause random phase tapering over the aperture, distorting the radiation pattern or even causing a misalignment between the TX and RX beams.

To quantify the effect of phase variations on the performance of an RDPA antenna, a Monte-Carlo simulation was performed. The RDPA array used in the simulation was a 10-module linear array similar to the prototype explained in chapter 3, with the design parameters given in the example in section 2.2.2. The phase errors across the array were taken from a normal distribution with an average of zero and standard deviation of 10° for both the TX and RX pattern simulations. Figure 2.11 plots the results of the Monte-Carlo simulation for 1000 trials at a 60° off broadside scan angle. The phase variation shows no significant degradation in the array gains or SLLs. The average beam misalignment yields a normal distribution with zero average and only 1.25° standard deviation.

The beam misalignment was also found to decrease for smaller scan angles and larger arrays. For the same parameters as listed above, the Monte-Carlo simulation was repeated for different numbers of modules and the average, μ, and standard variation, σ, of beam misalignment, SLL, and gain of the RDPA were extracted. Figure 2.12 shows how these parameters approach their theoretical values as the number of modules increases. The beam misalignment has an average of zero and its standard deviation continues to approach zero as the number of modules increases. The SSL and gain values curves were generated: one showing the average value plus the standard levitation ($\mu + \sigma$); the other showing the average value minus the standard levitation ($\mu - \sigma$). As can be observed from the figure, the SLL and gain reach their nominal values as the number of modules increases. The nominal values for a uniform array SLL is $-13\,\mathrm{dB}$, and its array factor gain is $10\log(\#ofmodules)$.

In implementation of an RDPA antenna for an specific application, there should be a quality control procedure to make sure that the amount of module-to-module variation is below a certain level. To establish the maximum level of acceptable variations, one can perform a similar Monte-Carlo simulation for a given level of tolerable beam misalignment.

2.3.2 Effects of offset in frequency multiplication ratio

The required frequency multiplication factors m_{TX} and m_{RX}, determined by (2.7), can assume large values depending on the RF frequency ratio. For example, for Ku-band satellite

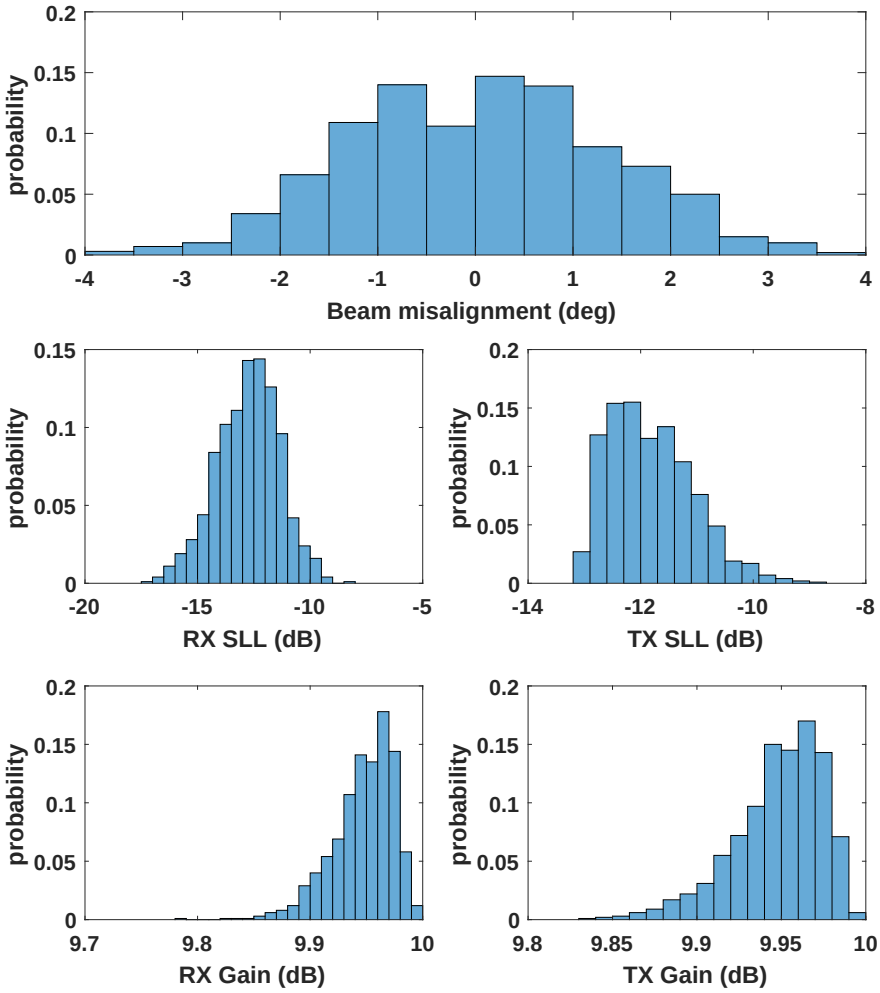

Figure 2.11: Results of Monte-Carlo simulation of a 10-module RDPA with random phase variations across modules.

links with $f_{TX} = 14.25\,\text{GHz}$ and $f_{RX} = 11.95\,\text{GHz}$, the smallest frequency multiplication factors are $m_{TX} = 285$ and $m_{RX} = 239$, respectively. Such factors are extremely difficult and inefficient to realize in practice. One solution is to approximate this ratio with another fraction with a smaller nominator and denominator (e.g. $\frac{239}{285} \approx \frac{5}{6}$). Such approximations result in a beam misalignment as explained in the following section. A better solution is to replace the two whole-number frequency multipliers with a fractional frequency multiplier (FFM) as described in section 2.4.1.

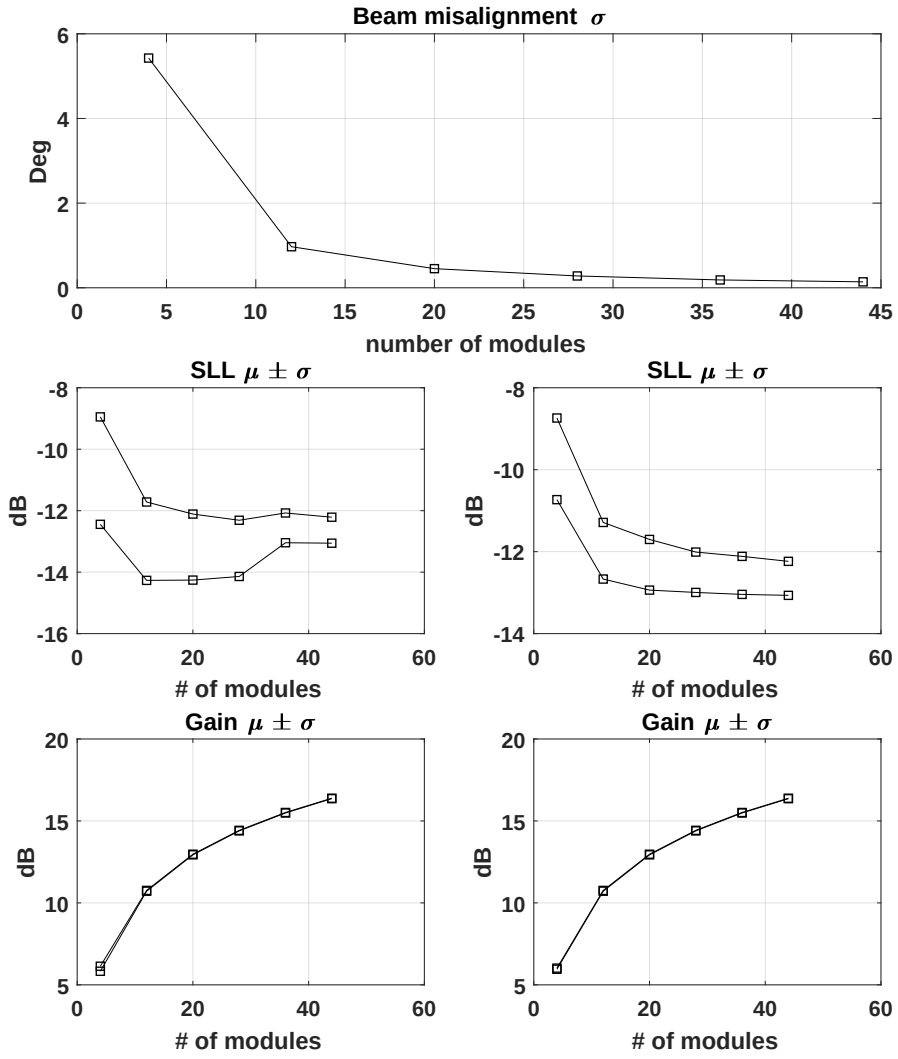

Figure 2.12: Phase variation effects on array key performance parameters decrease as number of elements in RDPA increase. Note that there are two curves tightly plotted on each of the *Gain* graphs.

The value of this beam pointing error can be easily found by comparing the tangential component of the wave-vector for the TX and RX beams. In Figure 2.13, assume that the TX and RX beams point at angles θ_{RX} and θ_{TX}, respectively. The tangents of the TX and

RX wave-vectors on the antenna aperture are,

$$|k_{TX}^{tan}| = \frac{2\pi f_{TX}}{c}\sin(\theta_{TX}) \tag{2.18a}$$

$$|k_{RX}^{tan}| = \frac{2\pi f_{RX}}{c}\sin(\theta_{RX}) \tag{2.18b}$$

where c is the speed of light in free space. We can divide (2.18a) by (2.18b), resulting in,

$$\frac{|k_{TX}^{tan}|}{|k_{RX}^{tan}|} = \frac{f_{TX}}{f_{RX}}\frac{\sin(\theta_{TX})}{\sin(\theta_{RX})} \tag{2.19}$$

The ratio $|k_{TX}^{tan}|/|k_{RX}^{tan}|$ is enforced by the phasing over the RDPA aperture, equal to m_{TX}/m_{RX}. Therefore, (2.19) can be rewritten as,

$$\frac{m_{TX}}{m_{RX}} = \frac{f_{TX}}{f_{RX}}\frac{\sin(\theta_{TX})}{\sin(\theta_{RX})}. \tag{2.20}$$

Using equation (2.20), the beam alignment is,

$$\Delta\theta \triangleq \theta_{TX} - \theta_{RX} = \sin^{-1}\left[\frac{m_{TX}}{m_{RX}}\frac{f_{RX}}{f_{TX}}\sin(\theta_{RX})\right] - \theta_{RX}. \tag{2.21}$$

For an approximate frequency multiplication ratio of $m_{TX}/m_{RX} = 6/5$ and $f_{TX}/f_{RX} = 14.25\,\text{GHz}/11.95\,\text{GHz}$, the corresponding beam alignment error is plotted in Figure 2.13. It can be seen that the error increases with scan angle. The maximum misalignment is 1.2° for a scan angle of 70°; potentially acceptable depending on the total beamwidth of the antenna.

2.4 LO generator circuit enhancements

2.4.1 Use of fractional frequency multipliers

As mentioned in section 2.3.2, a better solution for synthesizing LO frequencies is to use FFMs instead of regular whole number frequency multipliers. An FFM-based LO generator is explained in the following section. FFMs not only simplify the LO generator circuitry, they can be designed with a tunable multiplication ratio to enable the RDPA antenna to change its operational frequency bands on the fly.

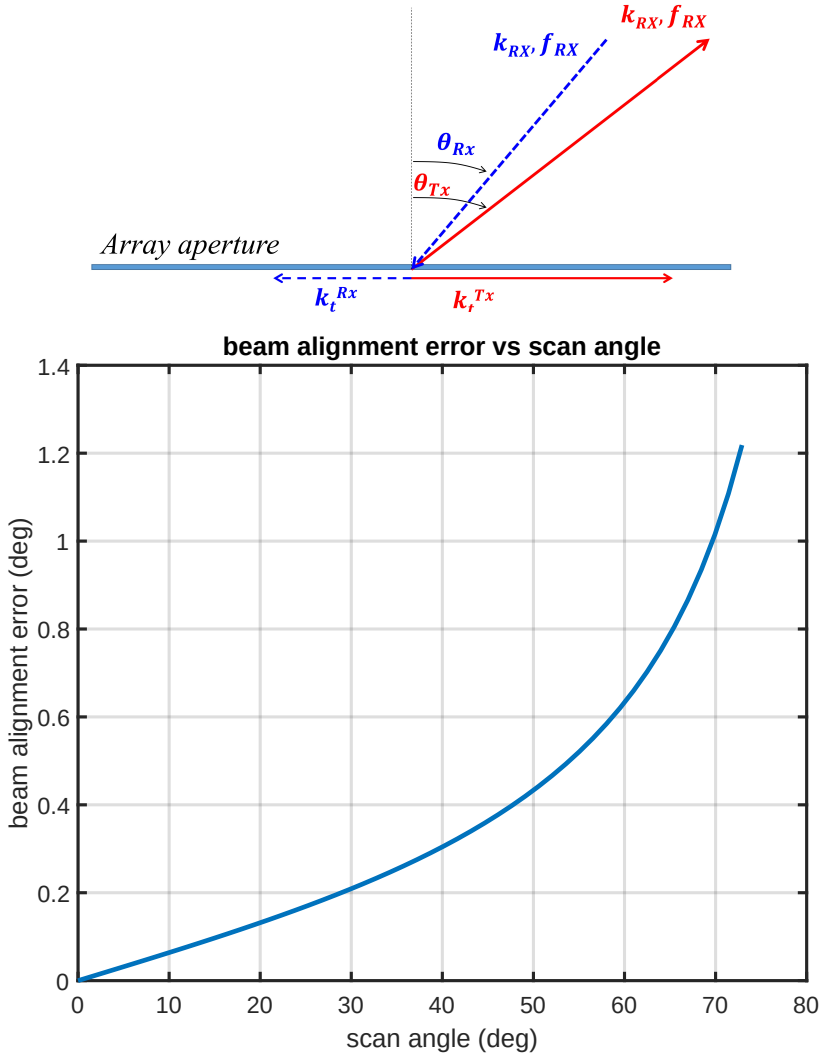

Figure 2.13: Top: misaligned TX and RX beams when m_{TX}/m_{RX} is not exactly equal to f_{TX}/f_{RX}. Bottom: beam pointing error versus scan angle for example presented in section 2.3.2.

Figure 2.14 illustrates how an FFM can be used instead of two frequency multipliers. An FFM with a multiplication factor of $\frac{m_{RX}}{m_{TX}}$ is used to generate the LO_{RX} signal, and no frequency multiplication is used to generate LO_{TX}. To determine the design parameters,

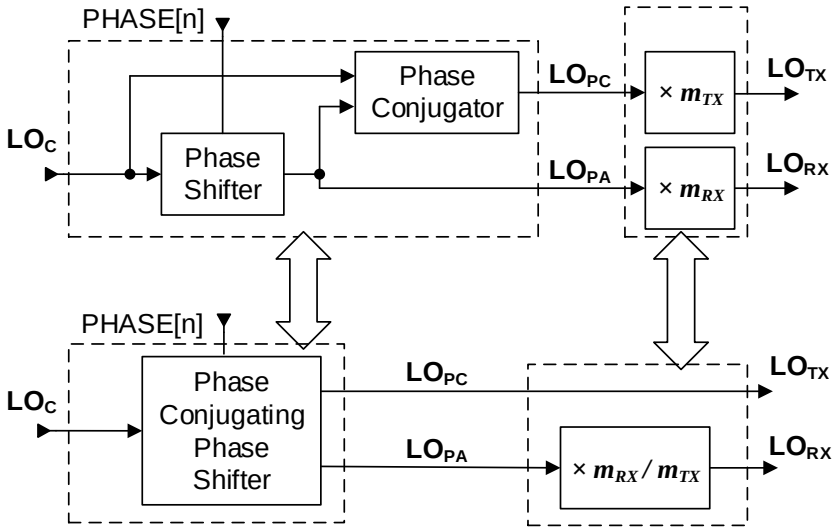

Figure 2.14: Top: original LO generator circuit. Bottom: alternative LO generator circuit using phase conjugating phase shifter and/or fractional frequency multiplier.

one needs to replace $m_{TX} \rightarrow 1$ and $m_{RX} \rightarrow \frac{m_{RX}}{m_{TX}}$ in the design equations (2.6) and (2.7). It is also possible to use a $\times\frac{m_{TX}}{m_{RX}}$ FFM to generate LO_{TX}, and no frequency multiplication to generate LO_{RX}. In this case, the design equations should be modified by the following replacements: $m_{RX} \rightarrow 1$, and $m_{TX} \rightarrow \frac{m_{TX}}{m_{RX}}$.

FFMs, such as [48], can offer a tunable multiplication factor which enables the RDPA system to operate at different RF frequency ratios. Moreover, by using a frequency multiplication factor less than one (i.e. dividing the frequency by a factor larger than one), the phase noise of the signal can be enhanced [49]. A regenerative FFM is presented in section 4.1.

2.4.2 Use of phase conjugating phase shifter

As shown in Figure 2.14, the phase shifter and phase conjugator can be replaced by a novel phase conjugating phase shifter (PCPS) to simplify the LO generator. The proposed PCPS is similar to a vector-sum phase shifter (e.g. [50]), except that the in-phase and quadrature signals are combined in two different ways to create two outputs whose phases are conjugates of each other. The operation of a PCPS is illustrated in Figure 4.8. First, the input signal is decomposed into differential in-phase and quadrature signals, $-I/+I$

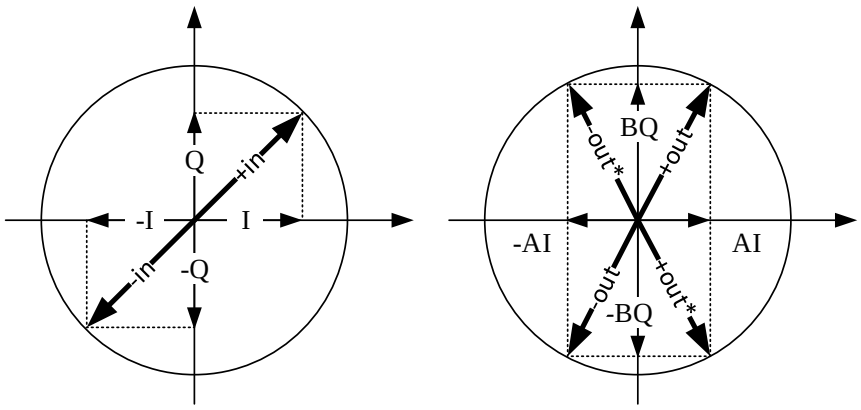

Figure 2.15: Concept of phase conjugating phase shifter. Left: input signal decomposed into in-phase and quadrature components. Right: phase shifted output and its conjugate (output*).

and $-Q/+Q$. Then, the amplitude of the I and Q signals are scaled by factors of A and B according to the required phase shift $\Delta\phi = \arctan(B/A)$. The summation of AI and BQ results in an output with a $\Delta\phi$ phase shift with respect to the input signal; whereas, the summation of AI and -BQ signals creates a conjugate output with a $-\Delta\phi$ phase shift. Details of operation and an integrated circuit implementation of such a PCPS are presented in section 4.2.

Another way to implement an LO generator is shown in Figure 2.16. Here a phased-locked loop (PLL) is used to perform frequency multiplication and phase shifting in the same time. By adding a control voltage to the output of the phase detector (PD), one can introduce a phase shift to the output of the voltage-controlled oscillator (VCO) as in [51]. A PLL provides a flexibility to synthesis frequencies with different ratios, as shown in Figure 2.16, as LO_{TX} and LO_{RX}. As in other topologies of LO generator explained before, a phase conjugator (PC) is required in either in LO_{TX} or LO_{RX} path. For a given frequency of f_0, the LO_{RX} and LO_{TX} are at frequencies $\frac{N_2}{M} f_0$ and $\frac{N_1 N_2}{M} f_0$.

Compared to the other topologies, using a PLL gives more flexibility and the PLL can be used as a part of the synchronization network as explained in section 2.2.3. One of the potential problems in having a VCO in each antenna module, is unwanted injection-locking between these VCOs caused by leakage of LO signal from one module to another. In the case of injection-locking between the antenna modules their VCOs run with a fixed phase relationship and will not respond to the phase shift commands. Therefor, careful design of antenna modules to avoid leakge of the VCO signals from one module to another is very

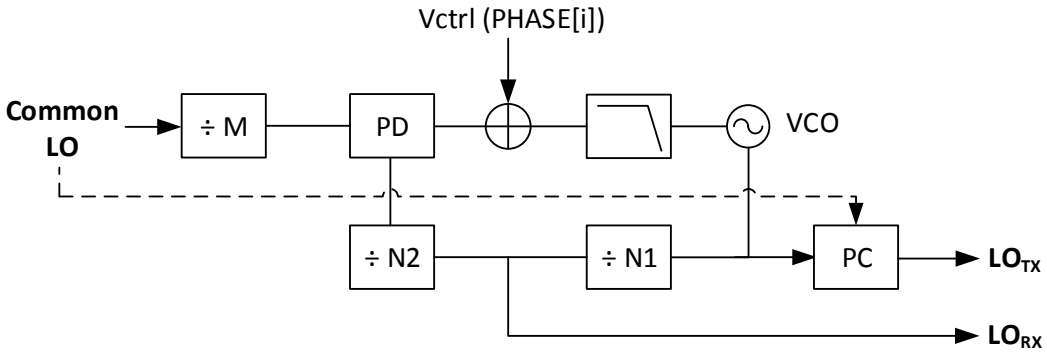

Figure 2.16: Alternative LO generator using a PLL.

important.

2.5 Conclusion

A novel RDPA concept has been presented. This antenna architecture is comprised of independent antenna modules, and its TX and RX beams can be optimized by a simple beamforming algorithm. Its radiation patterns are flexible, similar to a phased array antenna, and the TX and RX beams are always aligned; hence, it is also a retro-directive antenna. These two properties make the RDPA architecture a suitable choice for implementing an adaptive antenna: the beamforming algorithm controls only the RX beam for maximum reception, and the TX beam automatically follows the RX beam to maintain maximum transmission.

The effects of implementation uncertainties on the performance of the antenna were investigated by statistical simulation. The simulation results indicate that these effects are minimal due to the random nature of the uncertainties. In addition, they diminish as the number of antenna modules used in the antenna increases. The effect of other implementation errors and uncertainties were also investigated. The integral part of an RDPA architecture is its LO generator circuit. An enhanced substitute for the original LO generator was presented, and it will be explained in more detail in chapter 4.

Chapter 3

A proof-of-concept prototype

To demonstrate the validity of the proposed RDPA architecture, a proof-of-concept prototype was implemented using discrete electronic components and the design parameters given in the example in section 2.2.2, i.e.,

m_{RX}	m_{TX}	f_{RX}	f_{TX}	f'_{RX}	f'_{TX}	f_0
2	3	2 GHz	3 GHz	0.5 GHz	0.75 GHz	0.75 GHz

3.1 Prototype structure

Figure 3.1 displays the prototype consisting of 10 antenna modules configured into a uniform linear array with inter-elemental spacing of half a wavelength at f_{TX} frequency (50 mm equal to 1/3 wavelength at f_{RX}).

To simplify the prototype implementation, the IF antenna elements and the central unit antenna (shown in Figure 2.2) were replaced by coaxial cables and a 10-way power combiner/splitter. Given that the coaxial cables and the power combiner/splitter do not introduce significant frequency dispersion over the range of f'_{RX} to f'_{TX} ($0.5 - 0.75$ GHz), their combination is equivalent to the free-space propagation of the IF signals between the antenna modules and node A. On the RF side of the prototype, an array of 10 dual-band patch antennas generate the TX and RX beams of the RDPA prototype.

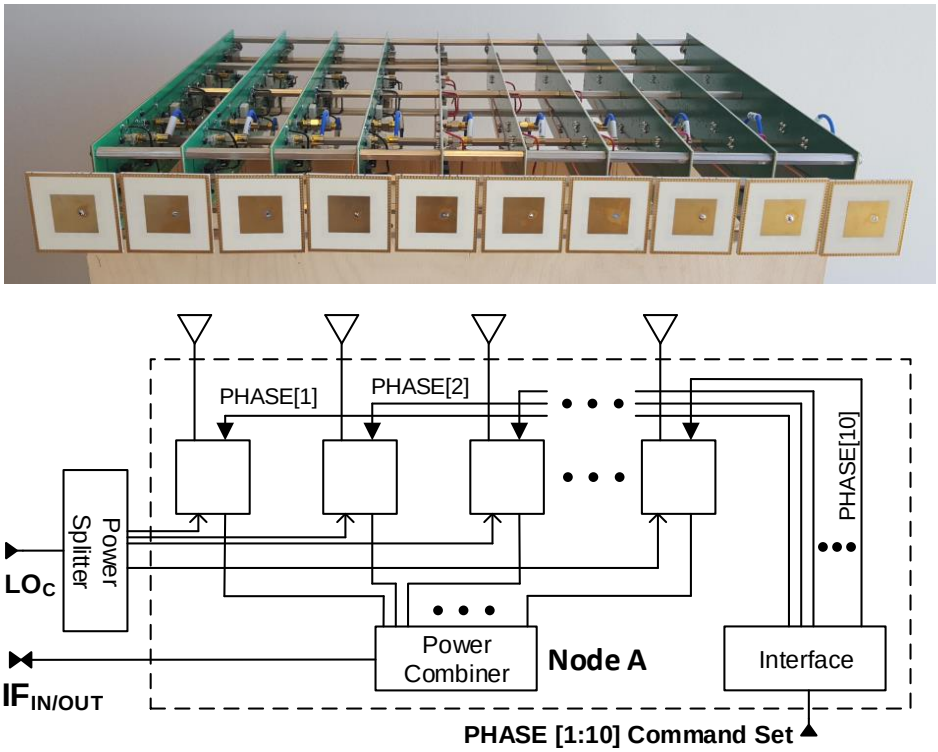

Figure 3.1: 10-element RDPA prototype.

3.2 Circuit test

Before measuring the radiation pattern of the full prototype, each antenna module was tested separately. First, the LO generation circuit of each antenna module was tested and then insertion gain and phase of each module were measured.

The outputs of each LO generator circuit, LO_{RX} and LO_{TX}, were measured in the time domain using an oscilloscope. To compare the measurement results with the theory, the frequency domain expressions for the LO generator outputs can be rewritten as given in (2.5) in the time domain (noting $\phi = 2\pi f\tau$),

$$LO^n_{TX} = \cos(m_{TX} 2\pi f_0 (t - \phi^n_p / 2\pi f_0)) \tag{3.1a}$$

$$LO^n_{RX} = \cos(m_{RX} 2\pi f_0 (t + \phi^n_p / 2\pi f_0)). \tag{3.1b}$$

Equation (3.1) indicates that LO_{TX} and LO_{RX} should have the same time delay, but with opposite signs, for the same value of ϕ^n_p.

Figure 3.2 displays the absolute value of time delay in the LO_{TX} and LO_{RX} signals with respect to the common LO signal, for different values of the phase shifter ϕ_p^n. For the whole range of ϕ_p^n, the error between the delay in LO_{TX} and LO_{RX} is smaller than 8%. Measurements confirmed that the time delays in LO_{TX} and LO_{RX} have opposite signs.

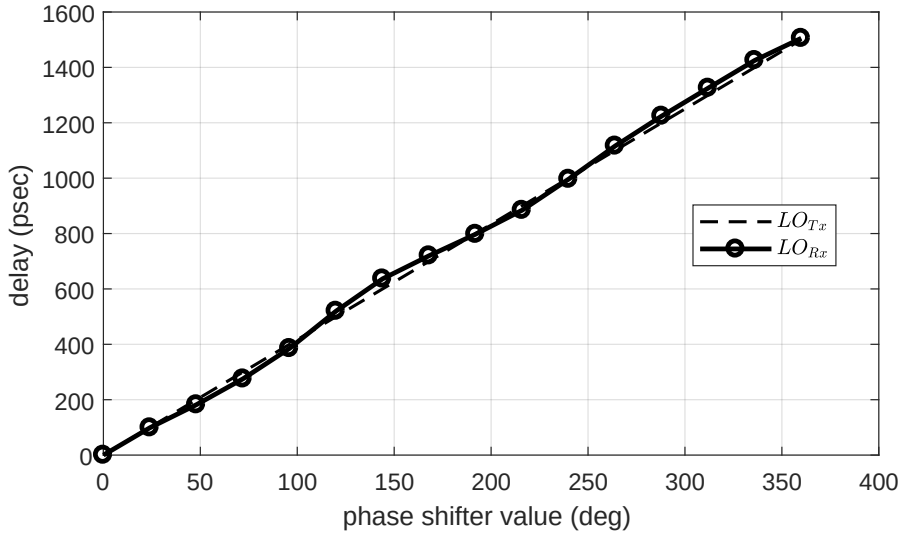

Figure 3.2: Typical measured time delay (absolute value) in LO_{TX} and LO_{RX} for different phase shifter values.

After measuring the LO generators, the insertion gain and phase of each module in both TX and RX branches were measured for a fixed PHASE[n] command. Figure 3.3 displays the insertion gain and phase measurement setup, including the IF 10-way power combiner/splitter; however, the RF antenna elements have been replaced by 50-ohm terminations except for the module under test.

The insertion gain and phase of each module were defined from the magnitude and phase scattering parameters seen by the network analyzer. Note that each module translates its input frequency from IF to RF in the TX mode and from RF to IF in the RX mode. Therefore, the scattering parameters cannot be measured directly; thus, external mixers are employed to up/down convert the frequencies as required.

Figure 3.4 displays the measured offsets in insertion gains and phases across the 10 modules with respect to the average insertion gain and phase. The offsets are within a range that should not cause significant beam misalignment as discussed in section 2.3.1. For more detail of the prototype circuit test see B.3.

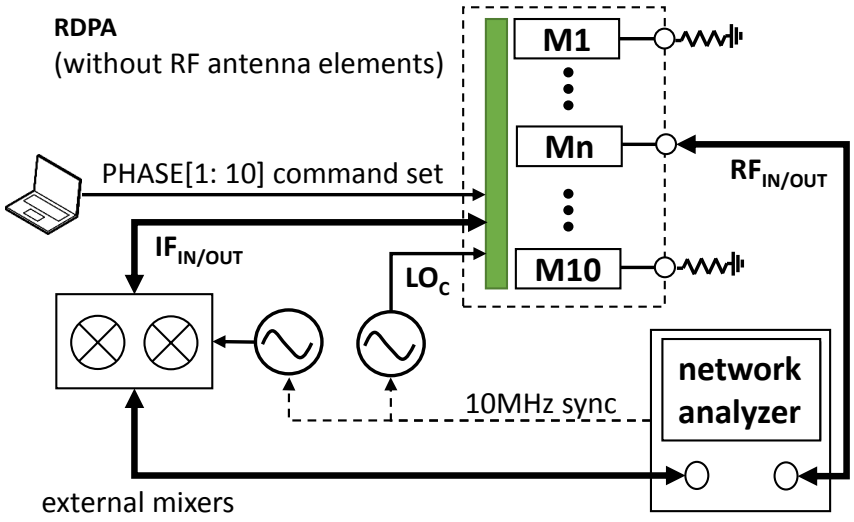

Figure 3.3: Circuit test setup for measuring module-to-module variations.

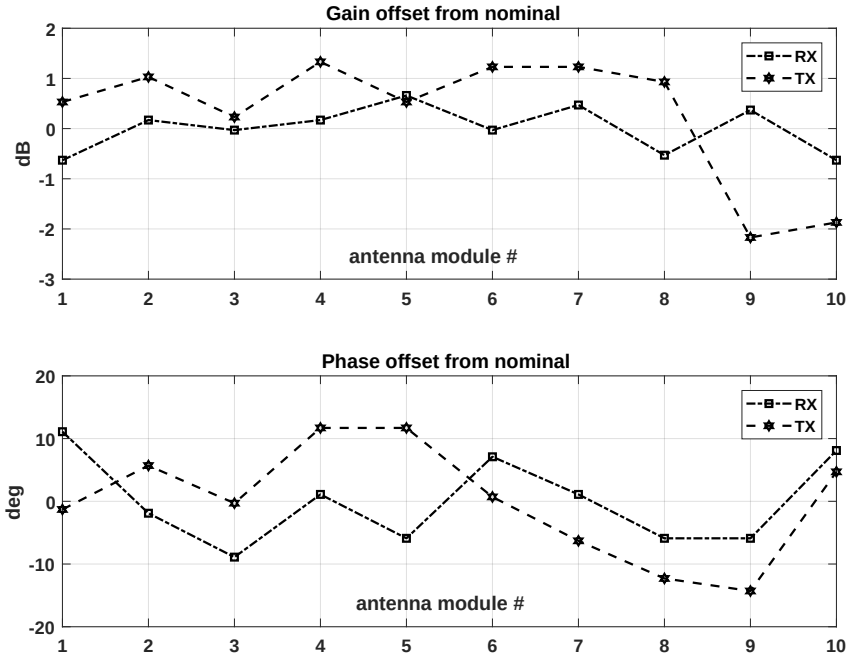

Figure 3.4: Variation in insertion gain (top) and phase (bottom).

3.3 Antenna test

The far-field radiation patterns of the RDPA prototype were measured in an anechoic chamber according to the setup displayed in Figure 3.5. The TX and RX patterns were measured for nine command sets, PHASE[1:10]; each set corresponding to a different scan angle ($\theta = -56.4°, -38.7°, -24.6°, -12°, 0°, 12°, 24.6°, 38.7°, 56.4°$). According to the retro-directivity property of an RDPA antenna, the TX and RX main lobes are expected to be aligned for the same command set.

First, the three-dimensional (3D) patterns of the RDPA antenna in TX and RX modes were measured to make sure there was no significant beam squint. This is important since the TX and RX beam alignment is being evaluated. Figures 3.6 and 3.7 display the 3D and 2.5D measured patterns, respectively. There is no significant beam squint, and it is evident that the TX and RX beams follow each other.

Two-dimensional (2D) radiation patterns of the antenna were obtained by cutting the 3D patterns along the line of the array. Each plot in Figure 3.8 shows the TX and RX patterns for the same command set with adequate alignment between the two beams for different scan angles.

To establish a baseline for evaluating the measured results, the array of RF antenna elements in the prototype was full-wave simulated, and the beam misalignment was extracted from the results. As shown in Figure 3.9, the simulated TX and RX beams are well aligned up to a 40° scan angle; they become slightly misaligned for higher scan angles. This misalignment is due to the difference between the RF antenna element patterns at TX and RX frequencies. In the measurement results, misalignments can also be caused by implementation and measurement inaccuracies; however, the results follow the simulation trends and are less than 8% of the total beamwidth. One can eliminate the misalignment caused by the RF antenna element by designing an element which has similar patterns at TX and RX frequencies. However, this misalignment naturally decreases as the number of antenna modules used in the RDPA increases. This is because the total radiation pattern is dominated by the array factor of the antenna. In other words, as one employs more antenna modules to create a narrower beam, the misalignment decreases naturally. The same is also true for beam misalignment caused by implementation errors as explained in section 2.3.1.

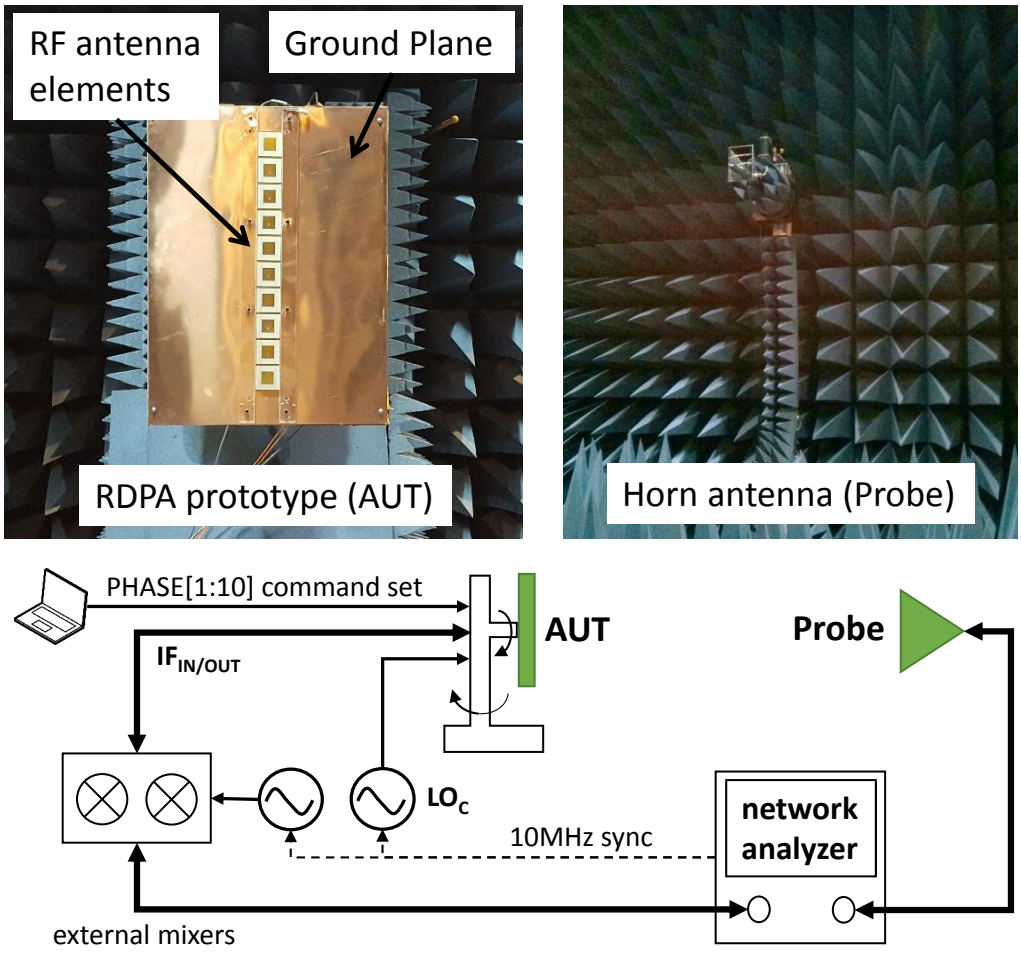

Figure 3.5: Far-field radiation pattern measurement setup. A ground plane, 45×60 cm, is added to the array antenna to shield the antenna modules. As with the circuit test setup in Figure 3.3, external mixers are used to make the RDPA frequencies compatible with the network analyzer.

3.4 Conclusion

A proof-of-concept prototype was fabricated and successfully tested, demonstrating the validity of the proposed RDPA architecture and its robustness against implementation uncertainties. In the next chapter, the implementation of a general antenna module using integrated circuitry is presented.

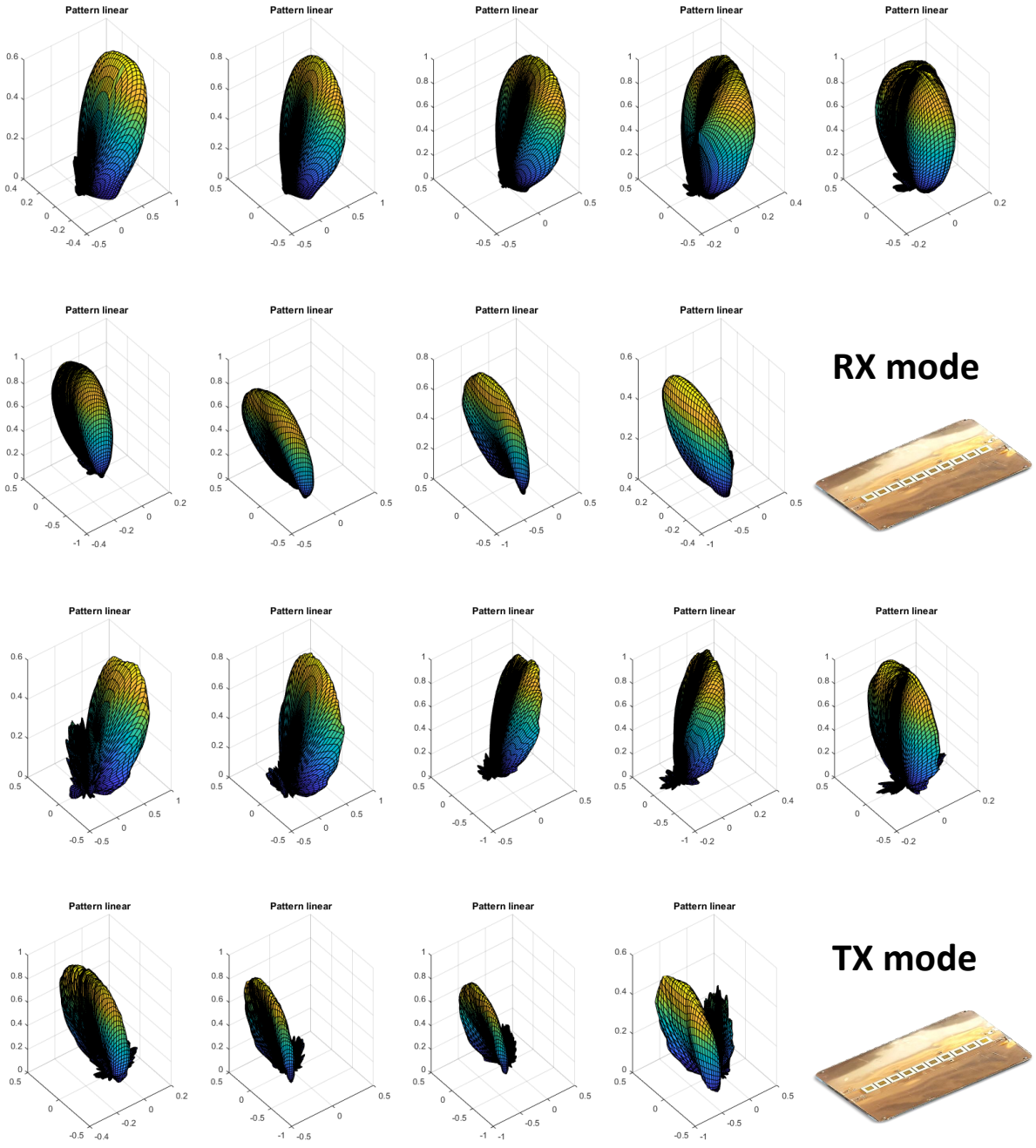

Figure 3.6: 3D patterns of RDPA antenna TX and RX modes for different scan angles.

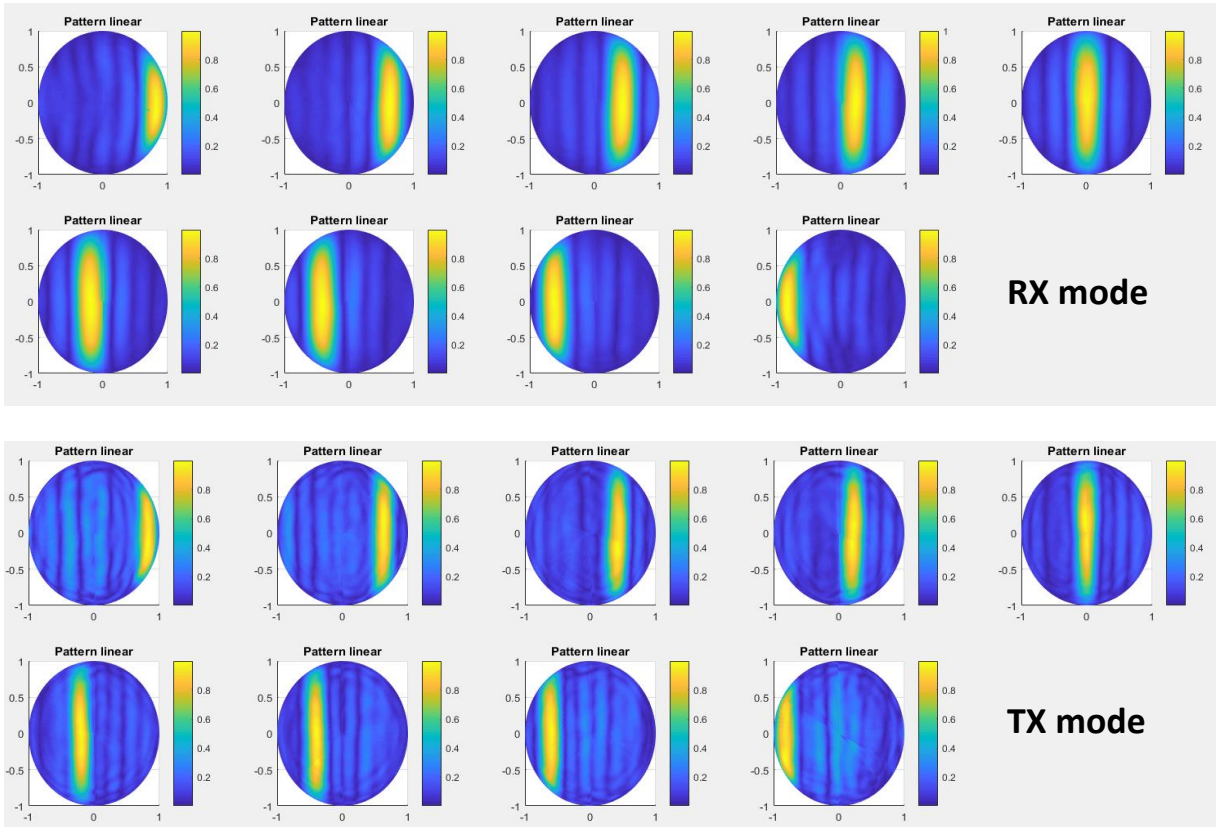

Figure 3.7: 2.5D patterns of RDPA antenna TX and RX modes for different scan angles (indicating main beams).

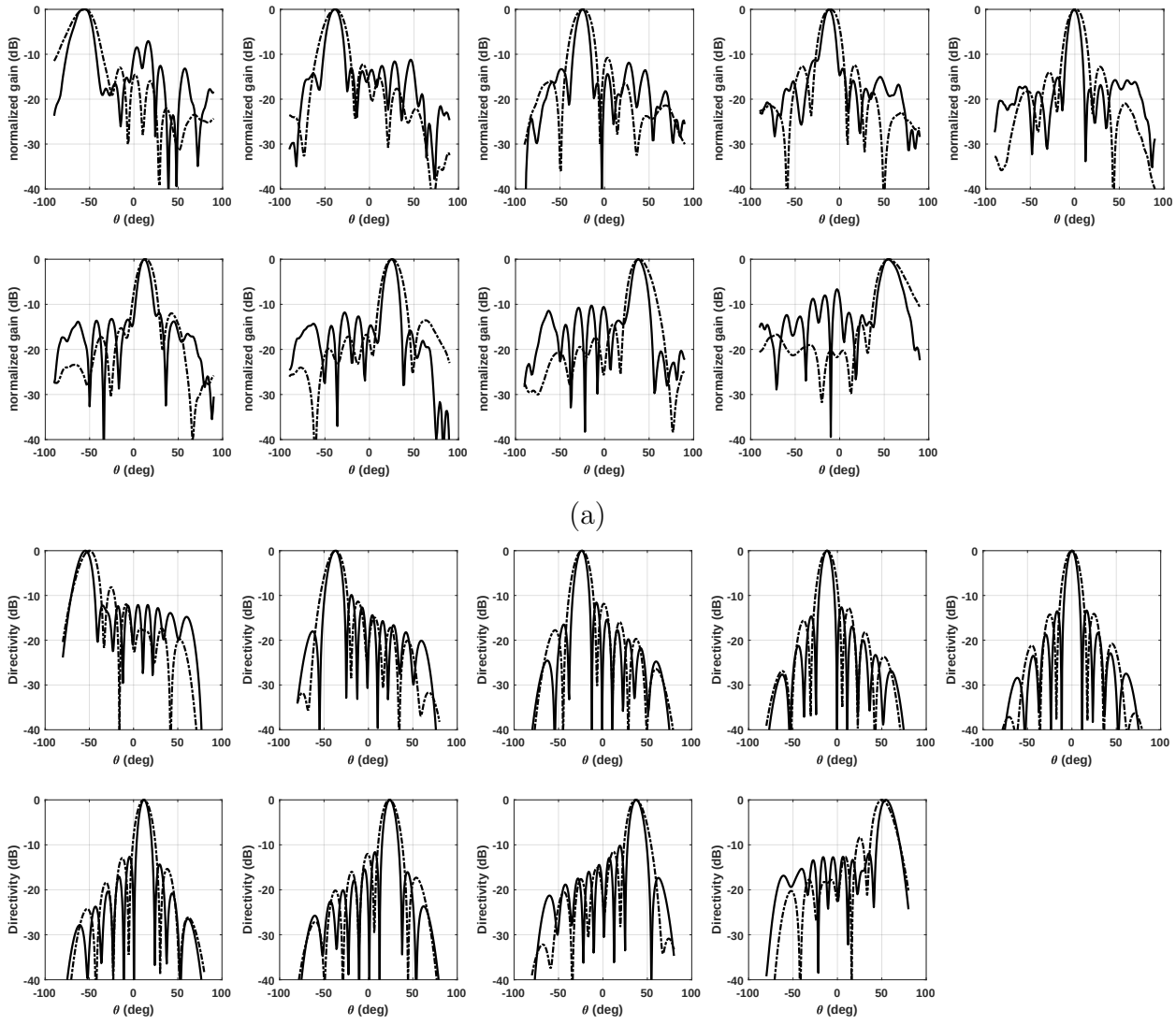

Figure 3.8: (a) Measured and (b) simulated TX (solid) and RX (dashed) radiation patterns (E-plane cut) at different off broadside scan angles.

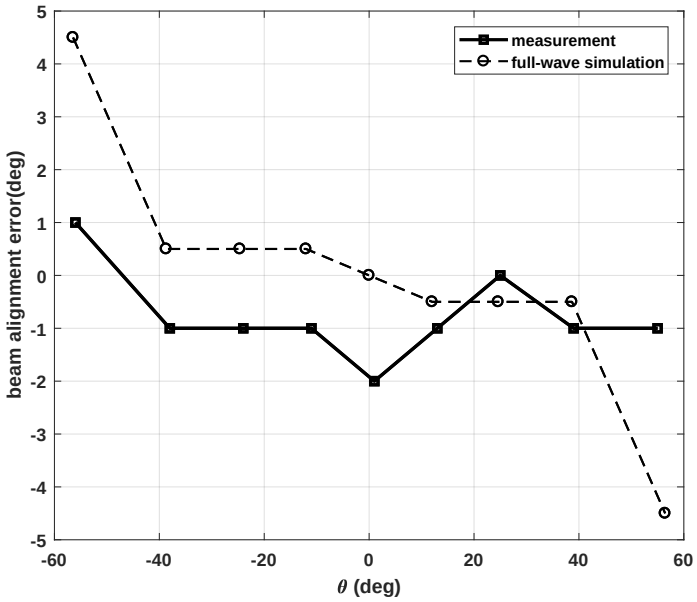

Figure 3.9: Misalignment between TX and RX main lobes at different scan angles for 10-module RDPA prototype.

Chapter 4

Integrated circuit implementation of key elements in antenna modules

The prototype in chapter 3 was implemented using general purpose discrete electronic components, so the performance of the individual components could not be optimized. Therefore, it is better to custom design the antenna modules at the transistor level using integrated circuit (IC) technology. Another reason for IC implementation is the antenna module space limitation; it is limited by the shortest wavelength of the RF frequencies. Moreover, the cost of an antenna module in the form of an IC drops dramatically in mass production whereas the cost of discrete components does not.

Among the antenna module components shown in Figures 2.3 and 2.4, most have well known IC implementations, except the LO generator. Hence, the author focused on the development of an efficient implementation of the LO generator block, using a fractional frequency multiplier (FFM) and a phase conjugating phase shifter (PCPS), as shown in Figure 2.14. The design frequency of these components was selected for an RDPA antenna for Ku-band mobile satellite communication where the uplink and downlink carrier frequencies are $f_{TX} = 14.25\,\text{GHz}$ and $f_{TX} = 11.95\,\text{GHz}$, respectively. According to design equations (2.6a) and (2.7), the system parameters can be chosen as:

m_{RX}	m_{TX}	f'_{RX}	f'_{RX}	f_0
5	6	$9.45\,\text{GHz}$	$11.25\,\text{GHz}$	$3\,\text{GHz}$

(4.1)

Note that there is a trade-off between the value of the synchronizing frequency, f_0, and the IF frequencies, f_{RX}/f_{LX}. Increasing the former decreases the latter, and vice versa,

according to (2.6a). Here, a relatively low f_0 is chosen to simplify the distribution of the synchronizing signal at the expense of higher IF frequencies. For the design parameters given in (4.1), and according to the block diagram of Figure 2.14, the FFM multiplication ratio should be 5/6 (converting 3 GHz to 2.5 GHz), and the PCPS operating frequency should be 3 GHz. In the following sections, the IC design and implementation of such a FFM and PCPS are presented.

4.1 Fractional frequency multiplier

FFMs based on phase interpolator [52], [48], and single side band (SSB) mixers [53, 54, 55], have been reported; however, each category has certain design and implementation challenges. The former requires generating copies of the input signal at several known phases as well as accurate time multiplexing, which often demands a calibration circuit. Similarly, the latter involves generating in-phase and quadrature signals for SSB mixer operation. These requirements increase the design complexity and process variation susceptibility. By contrast, this section introduces a regenerative FFM, based on a double side band (DSB) mixer with LC loads. It does not involve generating signals with known phases or time multiplexing. As a result, it is simpler to design and less susceptible to process variation.

4.1.1 Regenerative FFM

Figure 4.1 provides a block diagram of the proposed divider. For the output frequency f_{out}, the $\div N$ block generates a frequency of f_{out}/N that mixes with the input frequency, f_{in}, in the DSB mixer to create two side-bands at $f_{in} - f_{out}/N$ and $f_{in} + f_{out}/N$. Given that the upper side-band ($f_{in} + f_{out}/N$) is attenuated enough by the LC tank, the output frequency is $f_{out} = f_{in} - f_{out}/N$ (i.e., $f_{out} = \frac{N}{N+1} f_{in} = \frac{5}{6} f_{in}$). Here, $N = 5$ is chosen to achieve a frequency multiplication ratio of $\times\frac{5}{6}$. Moreover, for proper regenerative operation of the divider, the loop-gain in Figure 4.1 must be larger than one. To satisfy this condition, the input power should be larger than a threshold value (Ptr), which reaches its minimum at the LC tank resonance frequency [56].

4.1.2 Regenerative $\times 5/6$ FFM on 65nm CMOS

The proposed divider schematic is displayed in Figure 4.2. The mixer is a Gilbert cell with two LC tank loads, and varactors are used to tune the tanks by applying the *Vtune*

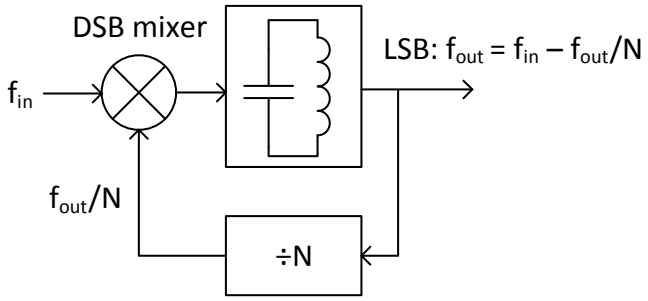

Figure 4.1: Block diagram of proposed regenerative frequency multiplier.

voltage. A differential input signal is applied to the mixer RF pins (gates of $M_{5,6}$) to mix with the LO signals (gates of M_{1-4}) and create the IF signal ($+Vo/-Vo$). A single-ended tap from the IF signal is connected to the ÷5 digital frequency divider through a resistive voltage divider ($R_{1,2}$). The ÷5 divider is implemented by using three D-flip-flops and a combinational circuit to reduce the number of flip-flop states from 8 to 5. The voltage divider ($R_{1,2}$) sets the DC level of the tapped IF signal to half of the V_{DD} value; this helps the divider to trigger with low input voltage swings. The complementary outputs of the ÷5 divider (Q, NQ) are fed back to the Gilbert cell as LO signals (gates of M_{1-4}). In the end, a buffer picks up the IF signal to avoid loading on the tanks.

The whole divider is fabricated in 65 nm CMOS technology. The divider itself consumes 6 mW at 1 V supply, and the buffer uses 11 mW at 2.5 V. Figure 4.3 displays the test setup and the fabricated die photo. The die is wire-bonded directly on a printed circuit board, and the differential input is provided by a transformer. The role of the 0-1V step voltage is to start the circuit as explained in 4.1.3. The SET/RESET commands of the D-flip-flops in the ÷5 section are both set at the disable state (connected to 1V).

4.1.3 Measurement results

Figure 4.4 shows the measured threshold input power (Ptr) for two cases: (i) fixed Vtune=1.2 V, and (ii) variable Vtune=$0 - 2.5$ V. The operating bandwidth of the divider for the fixed Vtune voltage is around 19%, and increases to 30% by changing the Vtune voltage proportionally to the input frequency. It was observed that the accuracy required in the $Vtune$ voltage at each input frequency was around ±0.2 V; fine-tuning the voltage merely decreased Ptr by a few dB. Therefore, it is not necessary to tune the tank at the exact desired output frequency.

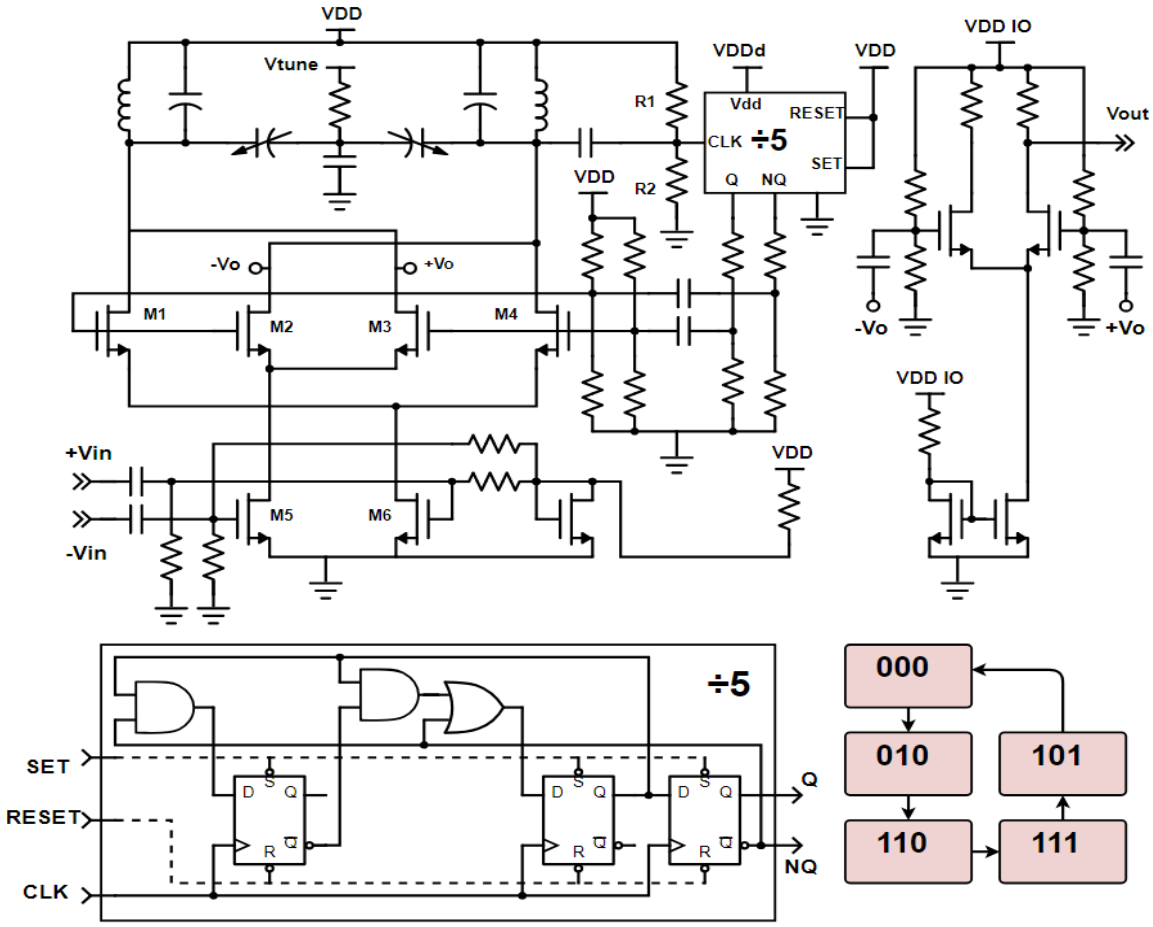

Figure 4.2: Schematic of proposed regenerative fractional frequency multiplier.

The spectrum and phase noise of the output signal were measured using a spectrum analyzer, while a 3 GHz −5 dBm signal was applied to the input. In Figure 4.5, the spectrum shows the desired output at 2.5 GHz with a power of −17 dBm. In addition, the 3.5 GHz upper side-band and the 3GHz input leakage appear at 15 dB and 19 dB below the desired output, respectively. The average result of 40 phase-noise measurements for both 2.5 GHz output and 3 GHz input signals are plotted in Figure 4.6. The input and output phase noises follow a similar trend, indicating good performance of the circuit. At 100 Hz offset, the phase noise of the output is 1.4 dB less than that of the input. However, it approaches the input phase noise at larger frequency offsets and goes above that by 10 dB at the 1 MHz offset, meeting the noise floor of the output. It is worth noting that the

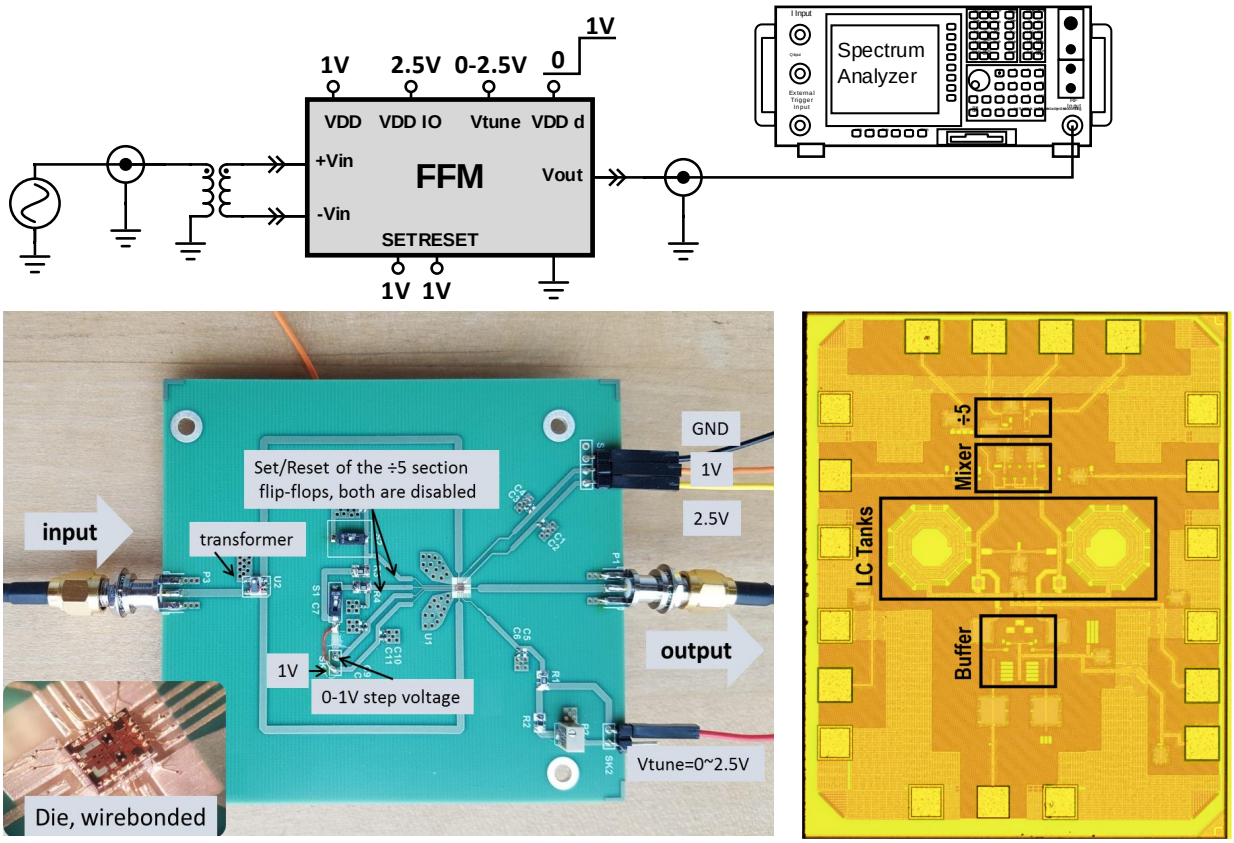

Figure 4.3: Test setup and fabricated die $1.5 \times 1.2mm^2$.

theoretical phase noise reduction after $\times\frac{5}{6}$ frequency multiplication is $20\log(1.2) = 1.58\,\text{dB}$ at small offsets from the carrier frequency [49].

Startup procedure

The proposed divider requires a kick to start it because the amplitude of the thermal noise at the input of the ÷5 divider is not large enough to trigger it. In this work, the kick is a 0 to 1 V step voltage, with a rise time of less than 40 nsec, applied to the supply pin of the ÷5 divider (*VDDd* pin in Figure 4.2), while the rest of the circuit is powered on. This step voltage changes the output of the ÷5 divider from its off-state ($Q = 0, NQ = 0$) to its on-state $Q = 1, NQ = 0$ (or $Q = 0, NQ = 1$), consequently switching on $M_{3,4}$ (or $M_{1,2}$). As a result, the drain currents of M_5 and M_6 start to flow through the LC tanks, causing an

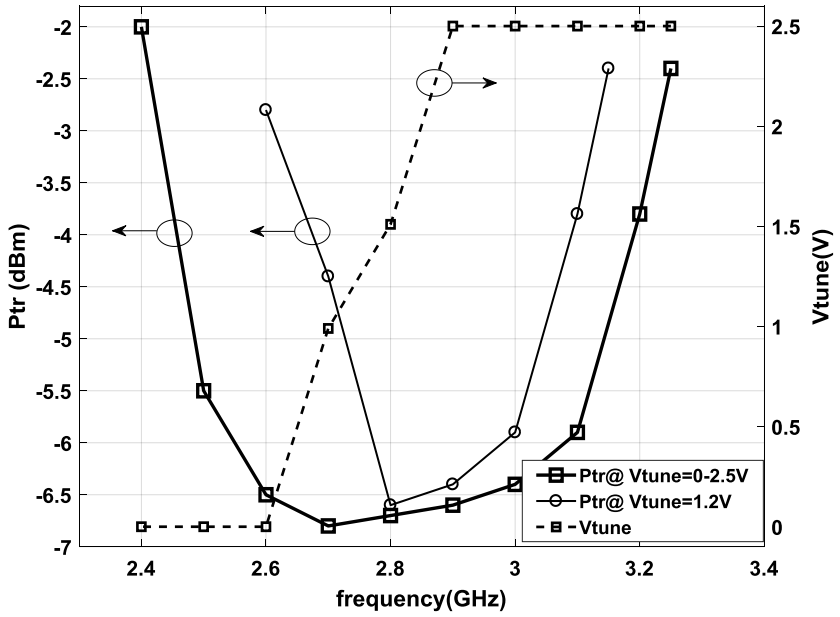

Figure 4.4: Measured Ptr and tuning voltage.

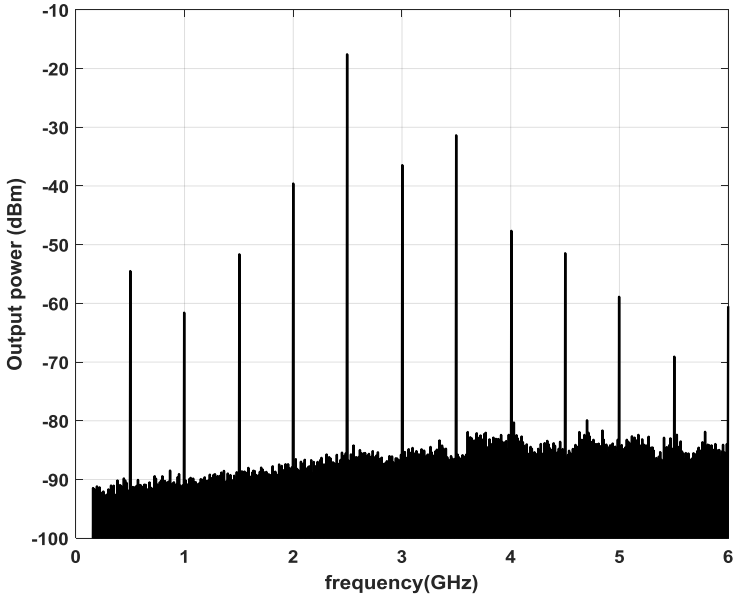

Figure 4.5: Measured output spectrum for 3GHz input.

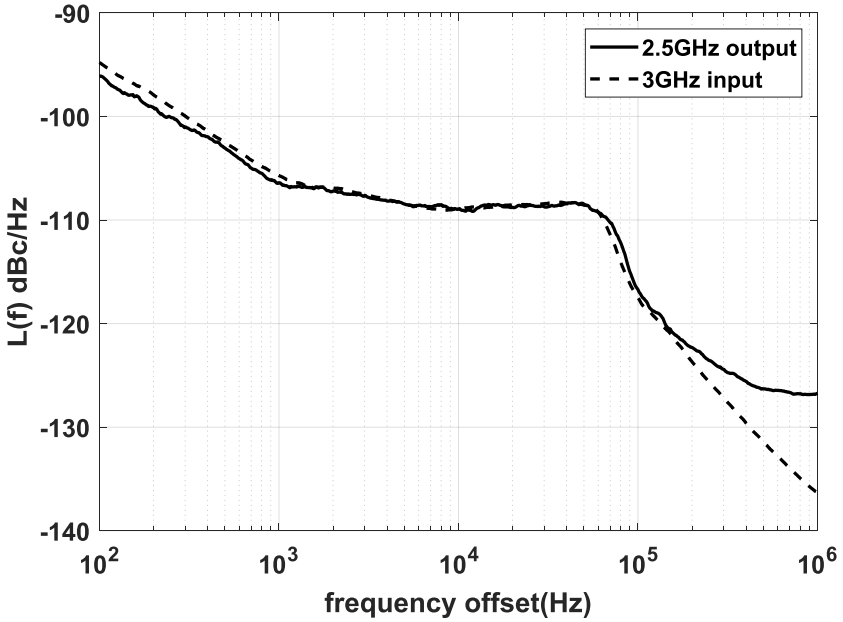

Figure 4.6: Measured phase noise of input and output signals.

oscillation at the tank's resonance frequency ($\frac{5}{6}f_{in}$). If the quality factor of the LC tanks is high enough to maintain this oscillation for at least five cycles, the $\div 5$ divider toggles the state of Q/NQ signals, thereby starting regenerative operation. Figure 4.7 displays the different waveforms in the FFM during startup.

4.1.4 Remarks

The main specifications of the proposed FFM are compared with similar designs reported in the literature in Table 4.1. In contrast to other works, the proposed divider does not require generating signals with known phases or time multiplexing, making its design simpler and less susceptible to process variation. Moreover, its operating bandwidth is extended by rough tuning of the LC tanks. On the other hand, the level of the largest harmonic in the output is only 15 dB less than the desired signal, mainly due to the relatively low quality-factor of the LC tanks. Furthermore, the tanks' inductors occupy half of the silicon area. However, the relatively high level of harmonics is not critical in RDPA applications because the output of the FFM will be used to drive a mixer.

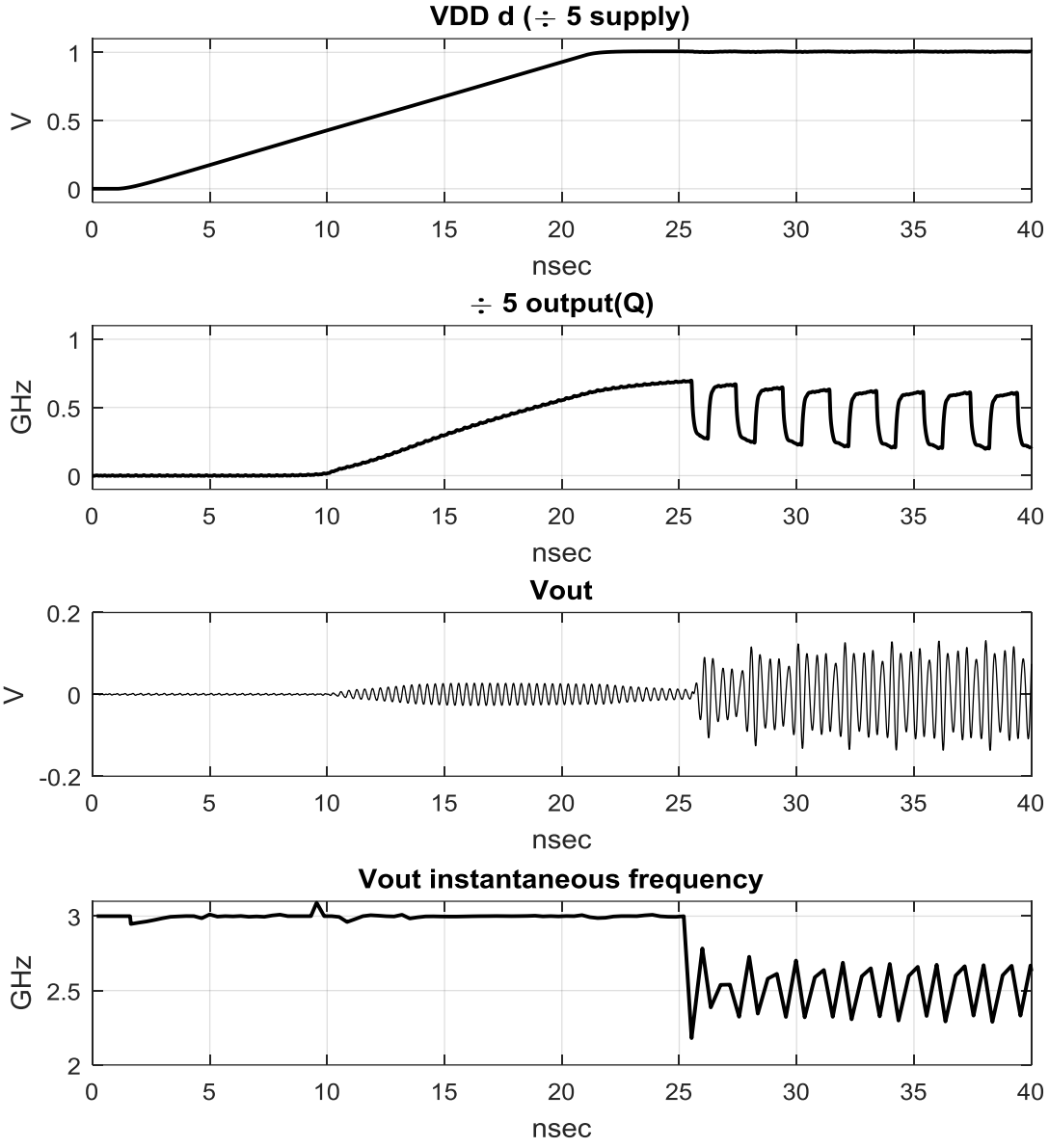

Figure 4.7: Simulated dynamic behavior of fractional divider during startup. The step voltage in VDDd forces the output of ÷5 divider from its off-state (Q=0/NQ=0) to its on-state Q=1/NQ=0 (or Q=0/NQ=1). This transition switches the LO MOSFETs in the mixer and consequently a current flows in the LC tank. Part of this current resonates at the tank frequency (2.5 GHz), starting the regenerative frequency division.

Table 4.1: Performance summary and comparison to prior works (*N and M are integers, **level of highest harmonic relative to the desired output).

	This Work	[52]	[48]	[53]	[54]	[55]
Input Frequency (GHz)	2.4-3.25	7.2-9.2	0.025-1.6	3.96	0.75-2.2	7.128
Frequency Division	1.2	3.5, 4.5	(N+M/32)*	7.5	3, 2, 1.5	4.5
Suppression** (dB)	<-15	NA	NA	-20	<-42	<-29
DC voltage (V)	1	1.2	0.9	1.8	1.2	1.8
DC power (mW)	6	3	<3.1	18	12	7.3
Process CMOS	65nm	65nm	20nm	0.18um	0.13um	0.18um

4.2 Phase conjugating phase shifter

Table 4.2 summarizes the on-chip phase shifting techniques in three categories. The first category of techniques rely on a varying the property of material, e.g. the dielectric or ferroelectric constant of a thin film , or a varactor capacitance, to directly change the transmission phase shift across input and output of the phase shifter. The properties of any material can only be changed in a limited range due to its physical properties, which can limit the phase shift range. The second problem is the frequency dependency of the material properties that results in frequency dependency of the phase shifter group delay, and consequently limiting its bandwidth. The third problem, is variation of losses of the phase shifter for different states of the phase shifter due to the behaviour of the material that its property is being changed.

The second approach for phase shifting are based on switching between a cascade of phase delay element, e.g. a lumped circuit or a piece of transmission line. This approach can achieve large phase shifting range by cascading more phase shifting sections in the expense of the higher losses. It can also achieve a constant group delays over a wide frequency range by using transmission lines as phase shifting element, in the expense of higher losses and larger chip area.

The third approach is based on changing the gain of an amplifier to change the phase. Generally speaking, changing signal amplitude is easier to do than changing its phase, and it can be changed from zero to a certain value with higher accuracies. The group of phase shifters known as vector-sum phase shifters use this technique and can achieve full 360° phase range. In a vector-sum phase shifter, the input signal is first decomposed into in-phase (I) and quadrature (Q) components and the I and Q components are scaled by two variable-gain-amplifiers (VGA) according to the required phase shift, and finally the scaled I and Q signals are summed together to create the output of the phase shifter.

Table 4.2: On-chip phase shifting techniques

	Ref	Technique	Frequency (GHz)	Phase shift range	Loss variation range (dB)
category 1	[57]	varying dielectric constant	10	240	3
	[58]	varying a varactor	5	180	5
category 2	[59]	switched (transmission lines)	58-62	270	2.5
	[60]	switched (lumped elements)	2.4	360	3.5
category 3	[61]	vector-sum phase shifter	5-18	360	2.8

The challenge in designing such phse shifter is designing the VGA in such a way that it can maintain its linearity over the gain variation range. In terms of bandwidth, the phase shifter performance is limited by the bandwidth of I and Q decomposing circuit (usually a poly-phase filter).

The idea of vector-sum phase shifters can be modified to create a phase conjugating phase shifter (PCPS) for RDPA antenna modules. The PCPS is able to perform phase conjugating and phase shifting in the same time which can greatly simplify the LO generator circuit used the RDPA antenna modules. Since the phase shifting is performed in the path of a narrow band LO signal, the bandwidth requirements are relaxed as well as the variation in phase shifter loss versus phase state.

The proposed PCPS is similar to a vector-sum phase shifter (e.g. [50]), except that the in-phase and quadrature signals are combined in two different ways to create two outputs whose phases are conjugates of each other.

The operation of a PCPS is illustrated in Figure 4.8. First, the input signal is decomposed into differential in-phase and quadrature signals, $-I/+I$ and $-Q/+Q$. Then the amplitude of the I and Q signals are scaled by factors of A and B according to the required

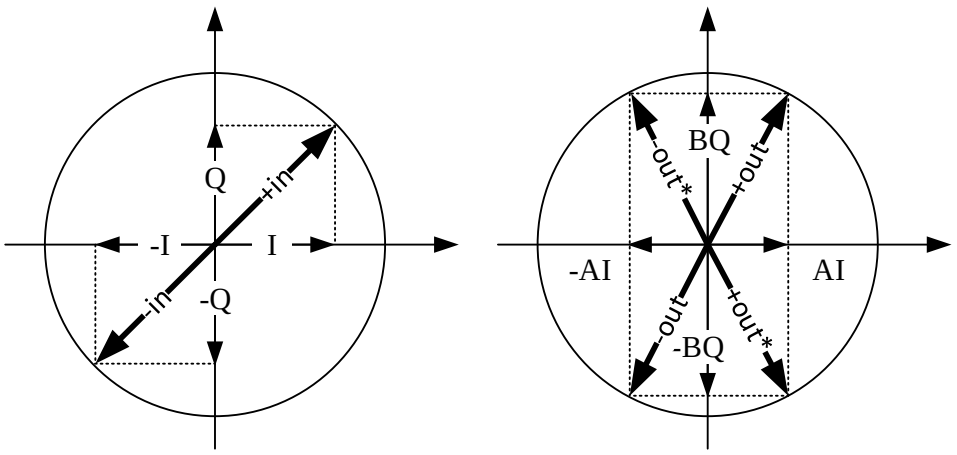

Figure 4.8: Concept of phase conjugating phase shifter. Left: input signal decomposed into in-phase and quadrature components. Right: phase shifted output and its conjugate (output*).

phase shift, $\Delta\phi = \arctan(B/A)$. The summation of AI and BQ results in an output with a $\Delta\phi$ phase shift with respect to the input signal; the summation of AI and -BQ creates a conjugate output with a $-\Delta\phi$ phase shift. To reach all four quadrants in the phasor diagram of Figure 4.8, scaling factors A and B should be varied from a negative value to a positive value. Moreover, it is desirable to keep the amplitude of both outputs, which is proportional to $\sqrt{A^2 + B^2}$, constant across the whole range of phase shifts. Therefore:

$$A^2 + B^2 = constant,\ while \begin{cases} -G_0 < A < G_0 \\ -G_0 < B < G_0. \end{cases} \tag{4.2}$$

Figure 4.9 shows an operational block diagram of the proposed PCPS. First, a balun converts the input signal into a differential pair, driving a polyphase filter to generate four copies of the input signal with phases 90° apart (i.e. $+I, -I, +Q, -Q$). Then, the differential signals $-I/+I$ and $-Q/+Q$ are scaled with gain A and B, respectively, by the variable gain amplifiers *VGA I* and *VGA Q*. Each *VGA* receives two commands; one to adjust its gain magnitude and the other to determine the gain sign. Finally, *SUM amp* adds the scaled in-phase signal to the scaled quadrature signal to create the phase shifted version of the input signal (i.e. *output*), and *SUM amp** subtracts them to generate the phase conjugate of the output (i.e. *output**).

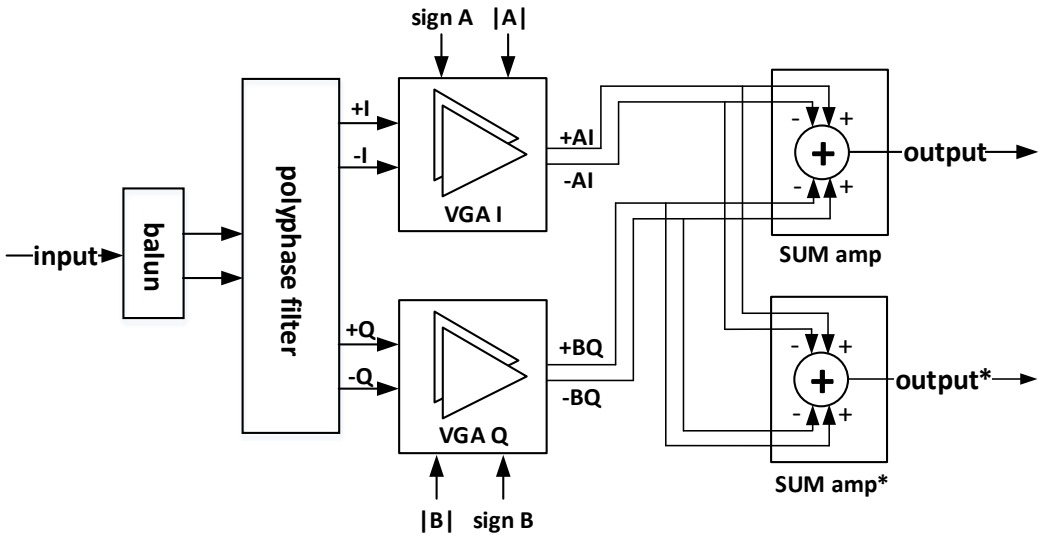

Figure 4.9: Operational block diagram of proposed PCPS.

4.2.1 A PCPS on 65nm CMOS

A PCPS was designed and fabricated in 65nm CMOS technology for an operating frequency of 3GHz. Since it was intended to be used to shift an LO signal, a relatively narrow operational bandwidth was required, making its design and implementation easier. The transistor level implementation of the blocks in Figure 4.9 are detailed in the next section. Performance measurement results for the PCPS IC follow.

Single to differential balun

To create a differential signal from the single-ended input, an active balun (similar to [50]) was designed. As shown in Figure 4.10a, it consists of a common gate (CG) MOSFET, M_1, and a common source (CS) MOSFET, M_2. The former provides a positive voltage gain of, while the latter yields a negative gain. In practice, a small phase shift would occur in the CG amplifier as the channel resistance, r_{ds}, and M_1 capacitances, C_{gs} and C_{ds}, form a parasitic RC phase shift network. M_1 is biased through R_{b1}, and R_{b2} and C_2 provide an AC short at the gate.

With the first degree of approximation, and ignoring the transistors channel resistance

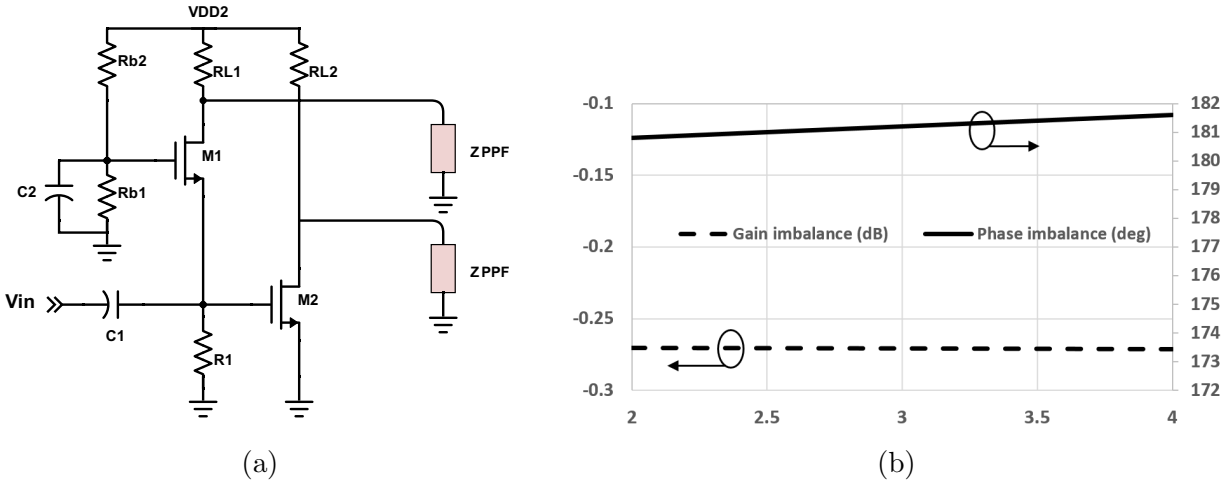

(a) (b)

Figure 4.10: (a) Active balun. (b) Active balun response.

and parasitic capacitances, the voltage gain and output impedance of the CG and CS amplifiers are:

$$CG:\ A_1 = g_{m1}R_{L1}||Z_{ou1}, Z_{out1} = R_{L1}||Z_{PPF} \tag{4.3a}$$

$$CS:A_2 = -g_{m2}R_{L2}||Z_{out2}, Z_{out2} = R_{L2}||Z_{PPF} \tag{4.3b}$$

Where g_m is the transistors transconductance, and Z_{PPF} is the single-ended input impedance of the poly-phase filter. First, let us assume that the balun is not loaded with the poly-phase filter. As explained in the following section, the poly-phase filter was designed in such a way that it provides the best impedance matching between the balun and the *VGAs*.

Ideally, $A_1 = -A_2$, $Z_{out1} = Z_{out2}$, and the input impedance seen at Vin would equal 50 Ω. The transistors M_1 and M_2 are both $24 \times 0.06um$, and R_{L1} and R_{L2} are chosen to be 100 ohms. Adjusting $R1$ controls the input impedance of the balun as well as the biasing of M_1 and M_2. The value of $R1$ and the biasing voltage at the gate of M_1 are adjusted for input matching and to make $Z_{out1} \approx Z_{out2}$. After optimizing $R1$ to 75 Ω, the balun shows a good phase and gain balance between its two outputs (Figure 4.10b), and input matching better than 10 dB.

Poly-phase filter

As shown in Figure 4.11, a first order poly-phase filter (PPF) is comprised of a cascade of four RC filters with differential excitation. At its resonance frequency $s = 1/RC$, the

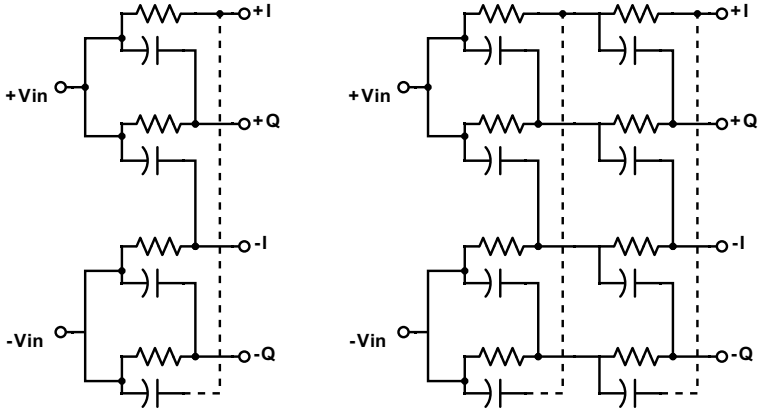

Figure 4.11: Left: first order poly-phase filter. Right: second order poly-phase filter.

output phases of the cascaded filters are 90° apart and their amplitudes are the same. At frequencies other than the resonance frequency, there is a phase and amplitude imbalance between the outputs. To increase the bandwidth of the filter, another PPF stage is added to form a second order PPF as shown in Figure 4.11.

The optimal R and C impedance values of a PPF for a given source (Z_s) and termination (Z_L), are derived in [62]. Here, the source impedance is the output impedance of the balun, and the termination impedance is the input impedance of the *VGAs*. According to the balun simulation, $Z_s = Zout_{1,2}$ is around $84 - j3\Omega$ and the termination impedance $|Z_L| = |Zin_{VGA}|$ varies between $880 - 912\Omega$ [1]. According to [62], for a double-stage PPF, the optimal value of resistance at the first stage, $R1$, is:

$$R1 = \sqrt{\frac{|Z_s||Z_L|}{K_{2R}}} \tag{4.4}$$

where k_{2R} is the ratio of the resistors in the second stage to the first stage. For $k_{2R} = 1$, and the values of Z_s and Z_L as given above, the value of R is 276.5Ω; for a 3 GHz resonance frequency, the value of C is 192 fF.

Variable gain amplifiers

As *VGA I* and *VGA Q* are the same, only *VGA I* will be discussed. As shown in Figure 4.12, the VGA is implemented by two differential pairs, $M_{1,2}$ and $M_{3,4}$, whose gains are

[1] VGA input impedance changes as its gain is varied

varied by adjusting their bias current from $0 - 3\,\text{mA}$. The bias currents are supplied by M_5 and M_6 and set by the bias voltage VA. The complementary switches at the gates of $M_{5,6}$ allow either the outer differential pair $M_{1,2}$ or inner pair $M_{3,4}$ to be turned on. If the outer pair gain is biased, a positive gain of A is created at the output; if the inner pair is biased, a negative gain of $-A$ is achieved. The transistors' sizes are $M_{1,2,3,4} = 18 \times 0.06\,\text{um}$ and $M_{5,6} = 21.2 \times 0.18\,\text{um}$, and the drain loads are 125Ω.

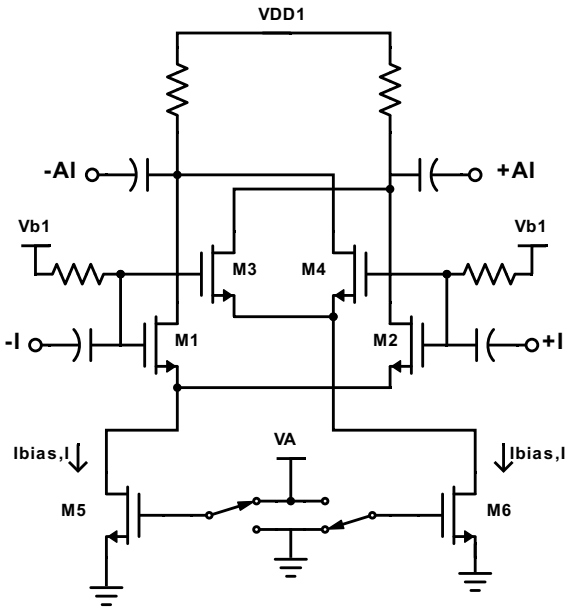

Figure 4.12: VGA with positive and negative gains.

In the saturation region of a MOSFET's operation, the drain current can be approximated by:

$$I_D = \frac{1}{2}\mu_n c_{ox}\frac{W}{L}(V_{GS} - V_{TH})^2[1 + \lambda(V_{DS} - V_{Dsat})]. \tag{4.5}$$

Therefore, the transconductance is:

$$g_m = \frac{\partial I_D}{\partial V_{GS}} = \mu_n c_{ox}\frac{W}{L}(V_{GS} - V_{TH})[1 + \lambda(V_{DS} - V_{Dsat})]. \tag{4.6}$$

Using (4.5), the transconductance in (4.6) can be rewritten in terms of the bias current:

$$g_m = \sqrt{2\mu_n c_{ox}\frac{W}{L}[1 + \lambda(V_{DS} - V_{Dsat})]I_D},\ I_D = \frac{I_{bias,I}}{2}, \tag{4.7}$$

The voltage gain of each differential pair in Figure 4.12 is linearly proportional to the transconductances of its transistors (i.e. $A \propto g_m \propto \sqrt{I_{bias,I}}$); similarly $B \propto \sqrt{I_{bias,Q}}$. Therefore, the constant output amplitude condition in (4.2) can be translated to the following:

$$(\sqrt{I_{bias,I}})^2 + (\sqrt{I_{bias,Q}})^2 = I_{bias,I} + I_{bias,Q} = constant,\ while \begin{cases} 0 < I_{bias,I} < I_0 \\ 0 < I_{bias,Q} < I_0 \end{cases} \tag{4.8}$$

Summing amplifiers

Both summing amplifiers, *SUM amp* and *SUM amp**, are the same. Only *SUM amp* will be described below. The SUM amp blocks should be able to add differential signals; therefore, two differential amplifiers and a current combiner are used as shown in Figure 4.13. Each differential pair is loaded with a current mirror that copies the current i_1 (i_7), to the drain of M_4 (M_8). The copied current i_1 (i_7) adds to i_2 (i_6), and the resultant current flows to the load. Therefore, the output voltage is:

$$Vout = Z_{load}(i_1 + i_2 + i_6 + i_7) \tag{4.9a}$$
$$i_1 = g_{m1}V_{in1} \tag{4.9b}$$
$$i_2 = g_{m2}V_{in1} \tag{4.9c}$$
$$i_6 = g_{m6}V_{in2} \tag{4.9d}$$
$$i_7 = g_{m7}V_{in2} \tag{4.9e}$$

Where g_{mn} is the transconductance of the M_n transistor, and Z_{load} is the output impedance of the current mirror in parallel with the matching network C_1, C_2, L_1 and any external load connected to the output node. If all g_{mn} are the same, (4.9) results in:

$$V_{out} = 2g_m Z_{load}(V_{in1} + V_{in2}). \tag{4.10}$$

To match the output to 50Ω, the values of $C_1 = C_2 = 3.7\,\text{pF}$ and $L_1 = 3\,\text{nH}$ are chosen. The sizes of the transistors are $M_{1,2,6,7} = 32 \times 0.06\,\text{um}$, $M_{3,4,8,9} = 97 \times 0.06\,\text{um}$, and $M_{5,10} = 97 \times 0.12\,\text{um}$.

Biasing DAC

As mentioned above, the bias currents of the VGAs must satisfy the condition (4.8) in order to achieve a constant output voltage across the whole phase shift range. To generate

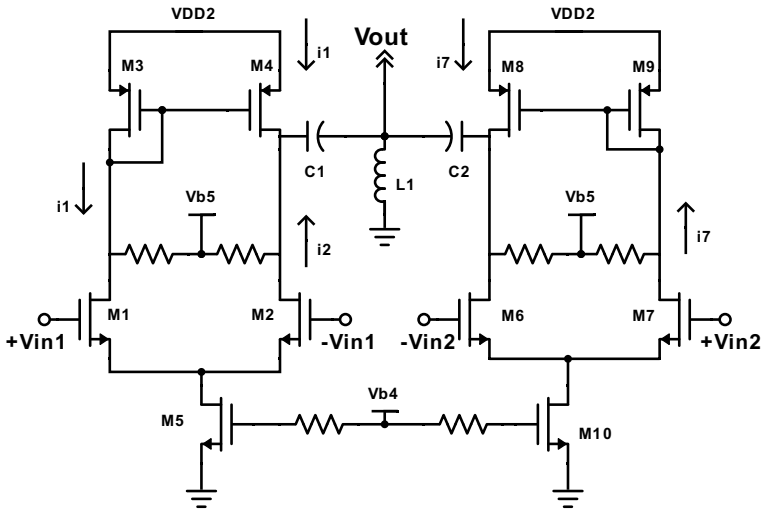

Figure 4.13: Schematic of *SUM amp*.

such bias currents, the biasing DAC shown in Figure 4.14 is used (the design is borrowed from [63]). First, a bias current of I_0 is generated by M_1 and is distributed between a group of transistors with different sizes but the same bias voltage, set by V_{REF}. In other words, the current I_0 is distributed between the transistors proportional to their relative sizes. Then, the current of each transistor is conducted to either M_2 or M_3 through the SPDT (Single-Pole Dual-Through) switches. A simple application of KCL to the circuit, shows that the summation of the currents in M_2 and M_3 must be equal to the current flowing in M_1 (i.e. $I_0 = I_{bias,I} + I_{bias,Q}$). Hence, the condition in (4.8) is satisfied independently of the states of the SPDT switches. Finally, the currents of M_2 and M_3, are copied to the VGAs' current sources through voltages *VA* and *VB*, respectively.

Remember the output phase is determined by the relative gain of the VGAs as $\Delta\phi = \arctan(B/A)$, $A \propto \sqrt{I_{bias,I}}$, and $B \propto \sqrt{I_{bias,Q}}$. Therefore, the relation between the biasing currents and output phase is $\Delta\phi = \arctan(\sqrt{I_{bias,I}/I_{bias,Q}})$, which is a nonlinear dependency. To linearize this dependency, the relative sizes of the transistors are chosen as shown in Figure 4.14. The transistors are sized such that an increment in code word $B_3B_2B_1$ results in a 11.25° phase increment. Note that the DAC accepts only three external bits, $B_{3,2,1}$; a correction bit, $B_c = B_3'B_2B_1 + B_3B_2'B_1$, is created locally.

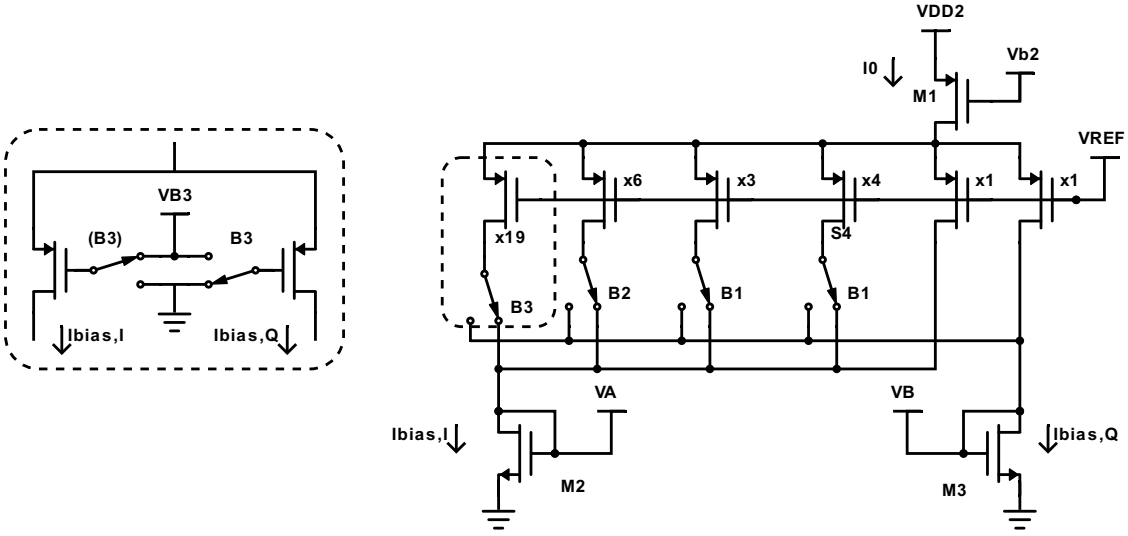

Figure 4.14: 3-bit biasing DAC.

Complete PCPS schematic and test setup

The complete schematic of the proposed PCPS is depicted in Figure 4.15. The full 360° phase shift is achieved by a 5-bit resolution: three bits controlling the biasing DAC ($B_{3,2,1}$), and two bits controlling the sign of the gains in *VGA A* and *VGA B* ($B4, 5$). The circuit has two supply voltages: *VDD1*= 1 V and *VDD2*= 1.4 V. The input balun, the biasing DAC and the sum amplifiers use *VDD2*; the rest of the circuit is supplied by *VDD1*. An external reference voltage, $V_{REF} = 0.9$ V, biases the transistors in the biasing DAC.

4.2.2 Measured performance of PCPS prototype

Figure 4.16 shows the fabricated PCPS and its test setup. The fabricated die is wire-bonded directly on a printed circuit board and its input and outputs are provided through coaxial connectors. The three-port S-parameters of the input (port #3), output (port#1), and output* (port#2) were measured by a network analyzer for 32 (5-bit) states of the phase shifter.

Measurement results showed that the circuit consumed 3.2 mW from its 1 V supply pin and 85.6 mW from its 1.4 V supply pin. These results closely match the simulated numbers 3.1 mW and 84 mW. Figure 4.17 shows the PCPS's matching, insertion loss, and

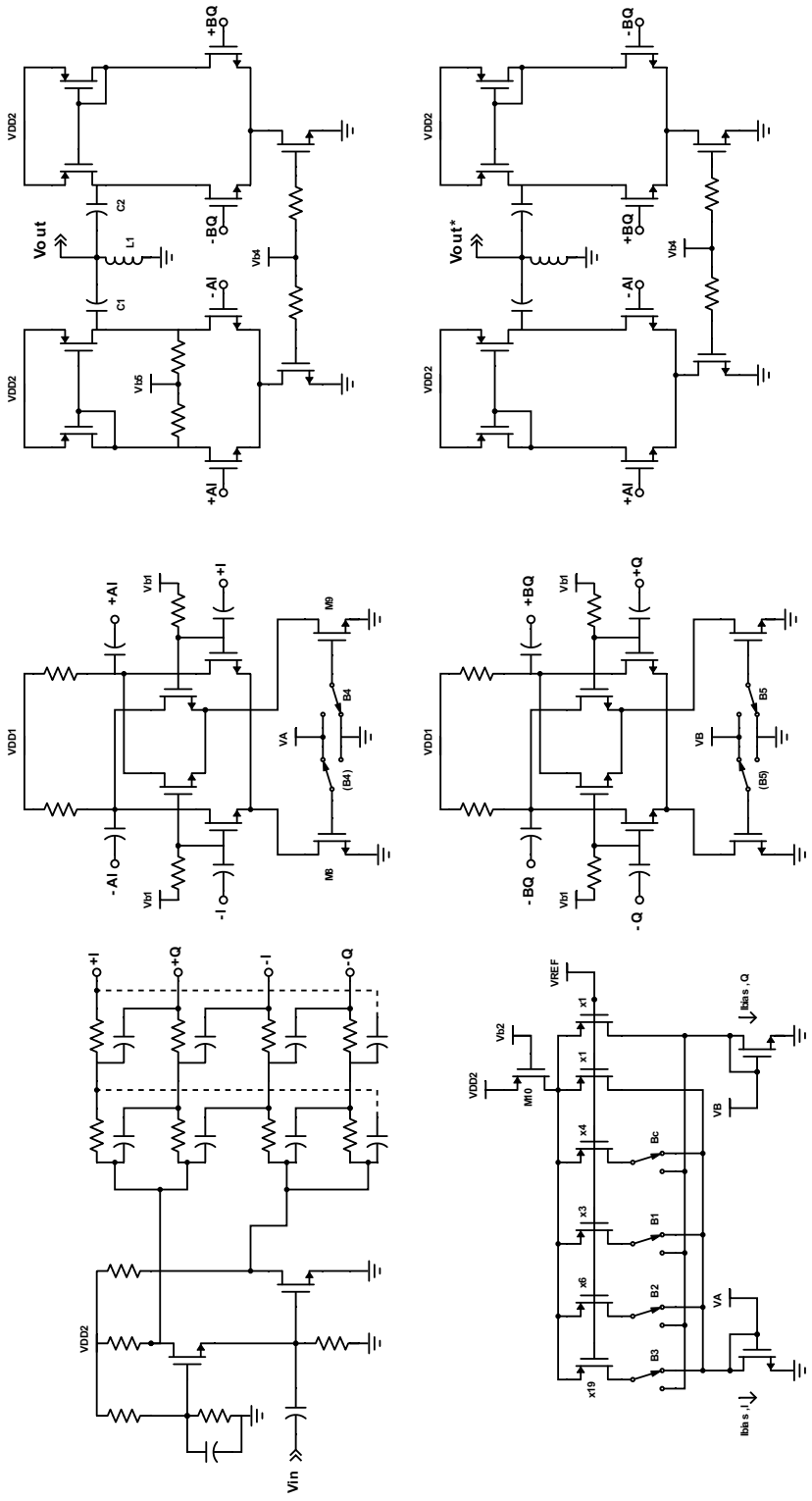

Figure 4.15: Schematic of fabricated PCPS.

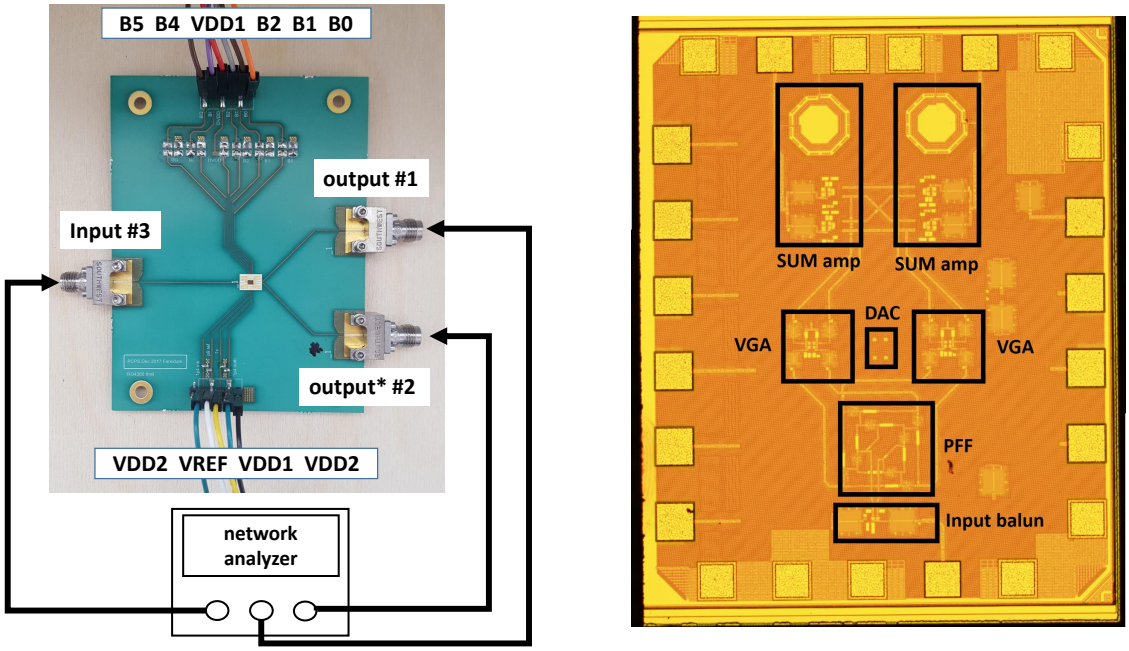

Figure 4.16: Left: PCPS test setup. Input power chosen to be $-10\,\text{dBm}$ ($P_{in,1dB} = 0\,\text{dBm}$). Right: Fabricated die $1.5 \times 1.2mm^2$.

the isolation between the output ports. The input and outputs matchings are better than $10\,\text{dB}$ over the range of $2 - 5\,\text{GHz}$. The measured insertion loss at $3\,\text{GHz}$ varies between $8.1\,\text{dB}$ to $9.8\,\text{dB}$, and the isolation is better than $25\,\text{dB}$. In the simulation, however, the numbers for insertion loss and isolation were $4.8 - 6.5\,\text{dB}$ and $> 50\,\text{dB}$, respectively. The difference can be attributed to losses in the connectors, printed circuit board transmission lines, and the wire-bonds.

Figure 4.18a shows the measured PCPS response. The polar plots show how the complex S_{13} and S_{23} vary with the state of the phase shifter at three different frequencies. As it can be seen for each circle (signal *output*), there is a cross (signal *output**), and the amplitude of the outputs are fairly constant across different phase shift states. Figure 4.18b plots the phase shifts seen at the two outputs of the PCPS, one increasing and the other decreasing, with the phase shifter state. A phase error is defined as the summation of the phase shift at the two outputs. Ideally, the phase error should be zero for all states of the phase shifter, meaning that the outputs' phases are conjugates of each other. Measurement results, however, show there was a small phase error (less than $\pm 5^\circ$) over the whole phase

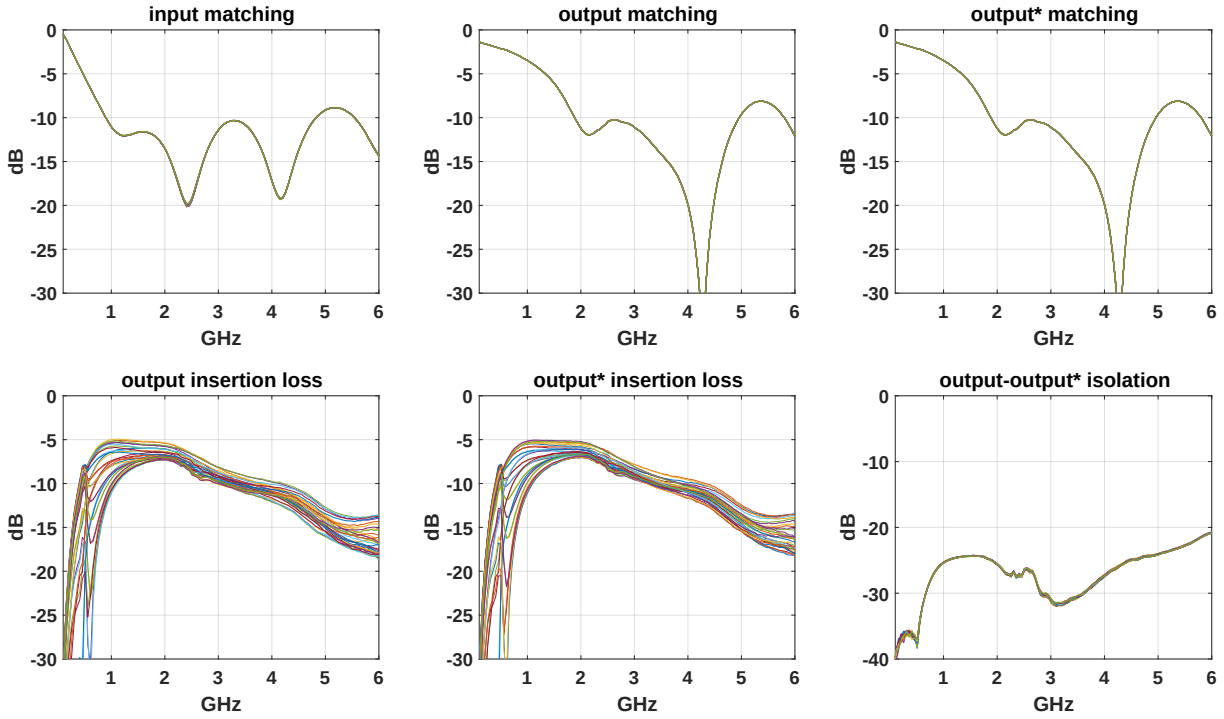

Figure 4.17: Top: Measured port matching for 50Ω: input, S_{33}; output, S_{11}; and output*, S_{22}. Bottom: Measured insertion losses S_{13} and S_{23}, and isolation between output ports, S_{12}.

range as plotted in Figure 4.18b. To evaluate the phase conjugating performance of the PCPS, the absolute value of the phase error versus frequency phase shifter states are shown in Figure 4.18c. The best performance is seen around 2.6 GHz.

4.3 FFM/PCPS-based LO generator

For real-world applications, the response time of an adaptive antenna is important [12]. The response time is defined as the time required for an antenna to form a new radiation pattern and it is limited by two separate mechanisms: (i) the time required for the beamforming algorithm to respond to changes in the RX signal and generate a new set of RX beamforming coefficients, and (ii) the time required for the antenna hardware to respond to the new RX coefficients (see Figure 1.3). The first or second mechanism may

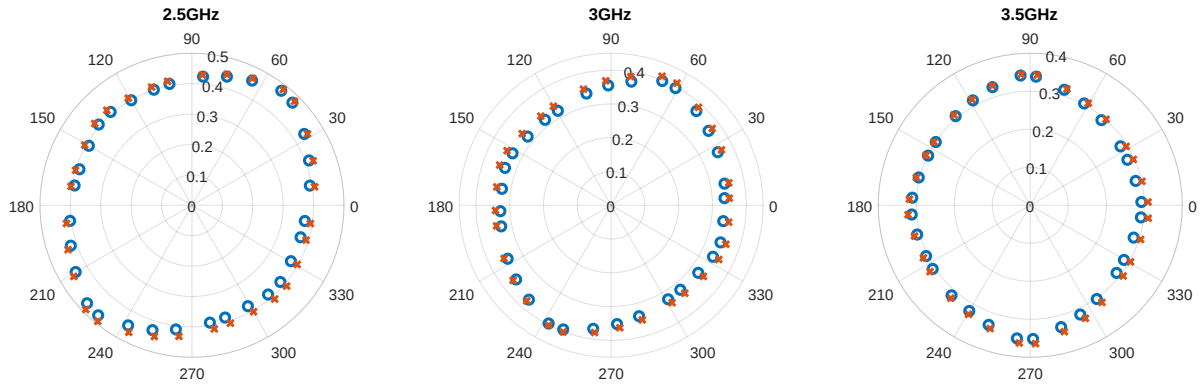

(a)

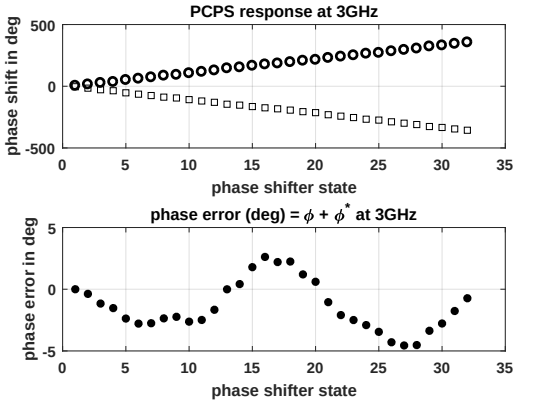

(b)

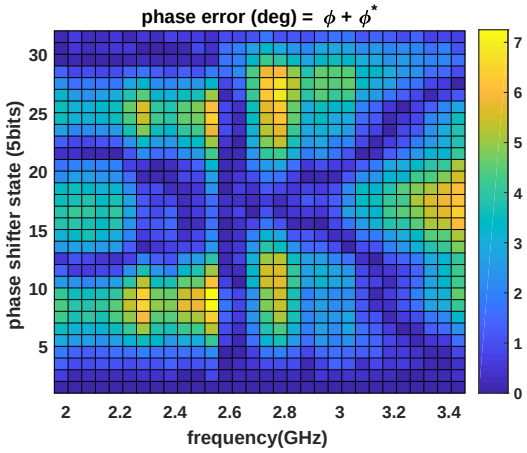

(c)

Figure 4.18: Measured PCPS responses: a) Polar plots of output (circle markers) and output* (cross markers); b) Phase response and phase error at design frequency for different states; and c) Phase error for different frequencies and states.

be dominant, depending on the complexity of the beamforming algorithm, the available processing power, and the specifications of the antenna hardware.

In an RDPA antenna the phase shifts are generated by the LO generator, therefore, it is important to evaluate the LO generator's transient performance when a new phase shift command is applied. As a metric, let us define the settling time the LO generator as the time required to produce LO_{TX} and LO_{RX} signals with steady phases once the phase

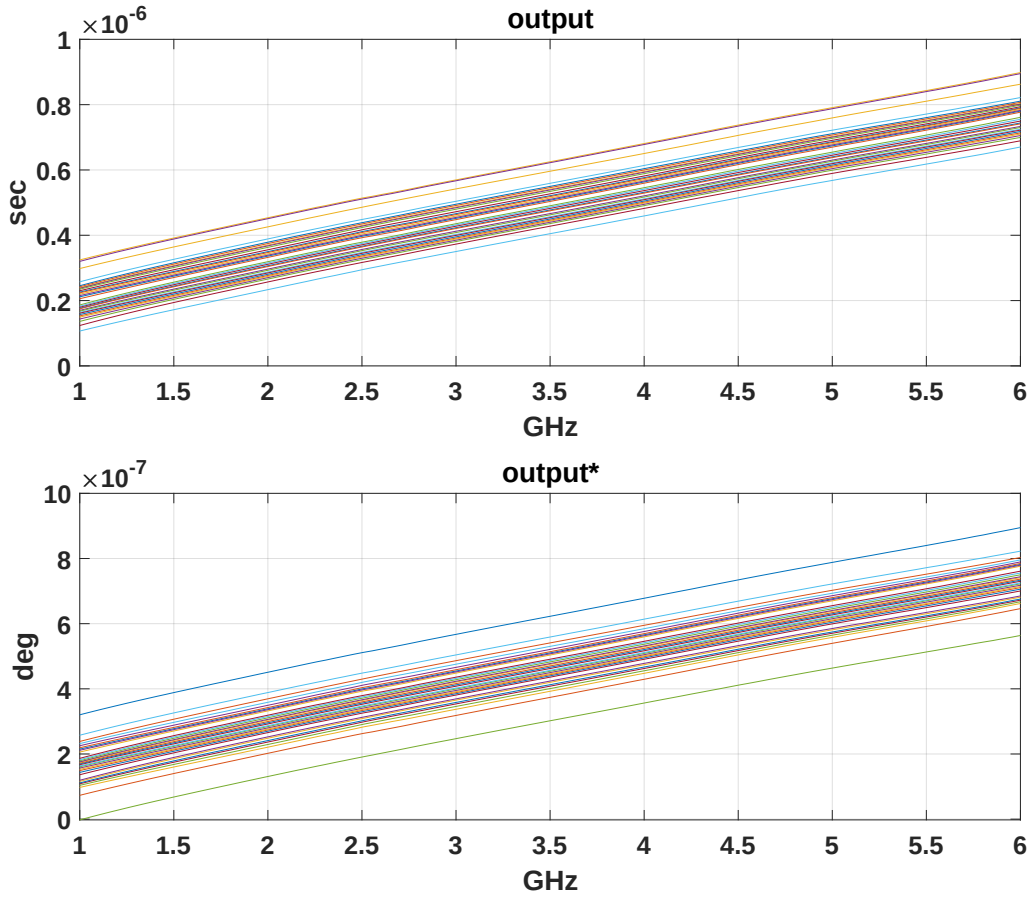

Figure 4.19: Group delay versus frequency for different states of PCPS.

shifter in the LO generator has changed 180°.

4.3.1 Settling time of FFM/PCPS-based LO generator

According to the block diagram in figure 2.14, an LO generator based on the proposed FFM and PCPS was made. To find the settling time of the LO generator, it was simulated in the following condition: a sinusoidal 3 GHz signal was injected to the input of the generator and the LO_{TX} and LO_{RX} waveforms were monitored. Then, a step phase command (t_{rise} = 1 psec) was applied to the PCPS to change its phase $\phi_p = 0 \rightarrow 180°$. As plotted in Figure 4.20, it took approximately 1 nsec and 1.5 nsec for the LO_{TX} and LO_{RX} signals to reach

their steady states. This amount of settling time should be more than enough for most of the targeted applications, leaving a large amount of headroom for other sources of delay. For example, for satellite on-the-move applications, the whole response time of the adaptive antenna should be in the range of a few msec.

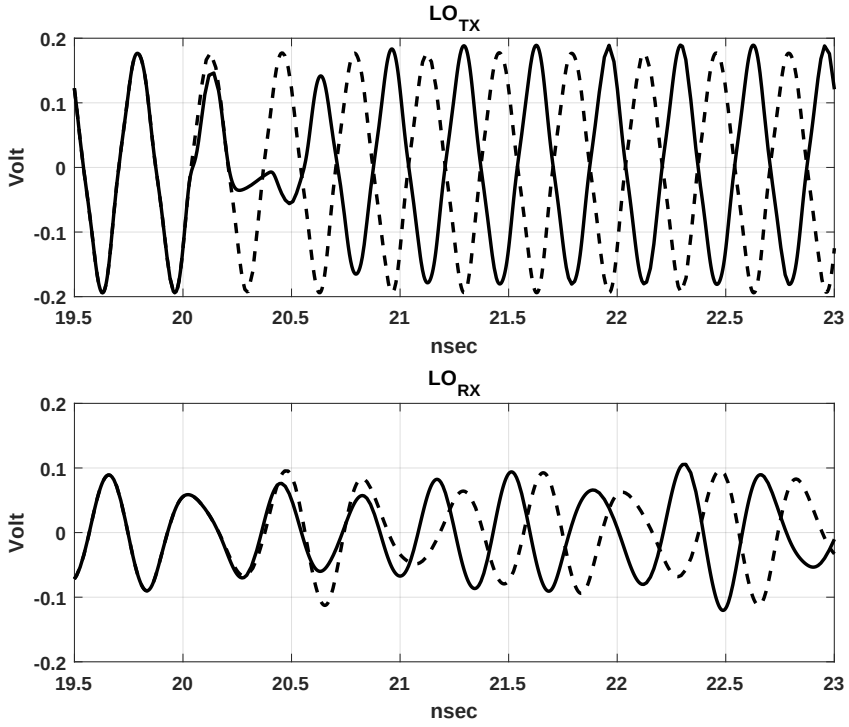

Figure 4.20: Transient response of LO generator based on proposed FFM and PCPS. Dashed line: reference waveforms for $\phi_p = 0$. Solid line: waveforms after changing phase shifter ($\phi_p = 0 \rightarrow 180^\circ$ at t=20 nsec).

Chapter 5

Conclusions and future work

5.1 Conclusions

A novel concept of retro-directive phased array antenna (RDPA) has been presented. The antenna architecture is comprised of independent antenna modules and its transmit and receive beams can be optimized by a simple beamforming algorithm. Its radiation patterns are flexible, similar to a phased array antenna, and the TX and RX beams are always aligned; hence, it is also a retro-directive antenna. These two properties make the RDPA architecture a suitable choice for implementing an adaptive antenna in which the beamforming algorithm controls only the RX beam (for maximum reception), and the TX beam automatically follows the RX beam to maintain maximum transmission.

The effects of implementation uncertainties on the performance of the antenna were investigated by statistical simulation. The simulation results indicated that these effects were minimal due to the random nature of the uncertainties; they also diminished as the number of the antenna modules used in the antenna increased. A proof-of-concept prototype was fabricated and successfully tested, demonstrating the validity of the proposed RDPA architecture and its robustness against implementation uncertainties. Finally, two key components of an RDPA antenna, a fractional frequency divider and a phase conjugating phase shifter, were designed and successfully implemented on 65nm CMOS technology; paving the path for future applications.

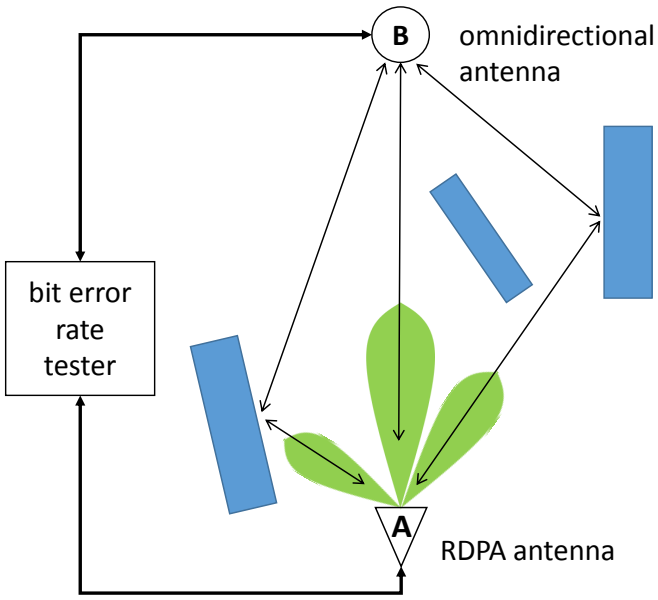

Figure 5.1: Experimental setup for evaluating RDPA antenna (at node A) in multipath environment.

5.2 Future works

There are substantial research and development opportunities to further explore the potentials and challenges of the proposed RDPA architecture; in the author's opinion, the following areas of research would seem indicated:

5.2.1 RDPA antenna performance in presence of multipath reflection

Exploring the potential use of RDPA antennas to combat multipath fading would be an important step forward; it would require simulation and measurement. It has been shown already that adaptive antennas can mitigate multipath fading by beam optimization in RX [1]. Since the RDPA TX pattern is a replica of its RX pattern, two-way multipath mitigation should be possible with an RDPA, theoretically. In other words, in RX the multipath is mitigated; in TX, the multipath is used to our advantage (see Figure 5.1).

An experiment could be performed using the prototype explained in chapter 3, a simple

beamforming algorithm (e.g. [11]) at node A, and a single antenna transceiver at node B, as depicted in Figure 5.1. In the experiment, a two-way data link between nodes A and B would be established and the bit error rate (BER) of the link measured. The location of node B could be changed to evaluate the beamforming capability of the antenna to maintain a low BER. The minimum BER for the A-to-B link and for B-to-A link should occur at the same location of node B, indicating retro-directive performance in a multipath environment. To provide a baseline for comparison, the RDPA antenna could be replaced by an omnidirectional antenna[1] and a set of similar measurements performed. The RDPA antenna would be expected to enhance the BER of the link compared to the omnidirectional antenna.

5.2.2 Development of a Ku-band antenna module

As mentioned in chapter 4, a fractional frequency multiplier, and phase conjugating phase shifter were developed for a Ku-band prototype LO generator. In the future, the rest of the antenna module should be developed and integrated with the LO generator. This integration could be in the form of a system-in-package (SIP) module or a monolithic integrated circuit containing a complete antenna module.

5.2.3 Development of a Ku-band RDPA prototype for LEO satellite links

Another challenging task is the design and implementation of a Ku-band RDPA prototype for LEO satellite links. As explained in section 1.1, there is a significant potential market for ground terminal antennas for emerging satellite-based internet services.

Important steps towards the realization of such a prototype, would be to integrate the antenna modules into a frame and distribute a synchronized signal between them, adding a beamforming algorithm to the antenna system. In addition to revealing the implementation challenges, the prototype would be a showcase of RDPA architecture for further commercial development. Figure 5.2 depicts a conceptual illustration of such a Ku-band prototype.

[1] with comparable EIRP and G/T as the RDPA antenna

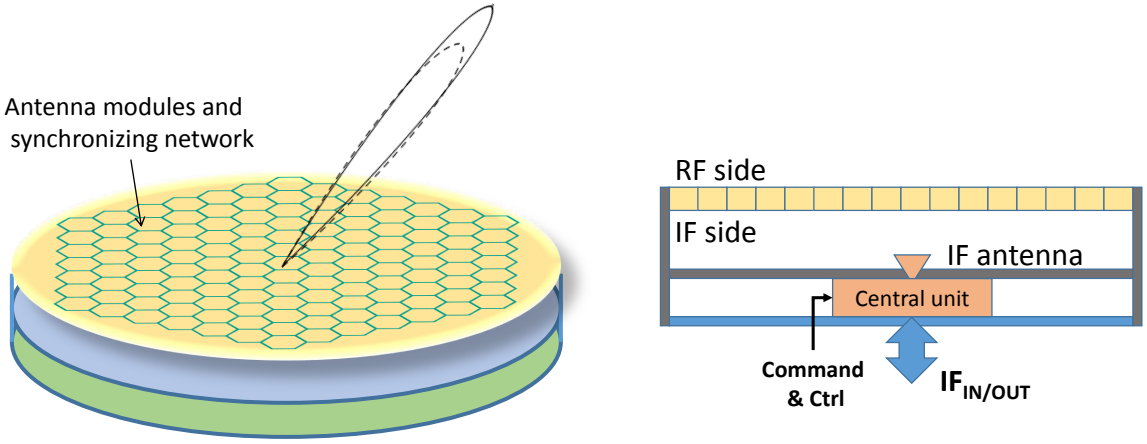

Figure 5.2: High-level illustration of potential Ku-band prototype.

APPENDICES

Appendix A

Derivation of required LO phases

As mentioned in section 2.2.1, the phases of the LO signals depend on the mode of the mixers. For USB and LSB1 modes, finding the required phase of the LO signals is easy. However, finding the required phase of the signal for mode LSB2 requires a lengthier derivation. For TX mixer at LSB2 mode,

$$\phi^n_{RFTX} = \underbrace{\phi^n_{LOTX} - \phi^n_{IFTX}}_{\text{what we have}} = \underbrace{\phi^n_{IFTX} + \phi^n_{TX}}_{\text{what we want}} \Rightarrow \phi^n_{LOTX} = 2\phi^n_{IFTX} + \phi^n_{TX}. \tag{A.1}$$

If we consider node A as the time reference in transmission, $\phi^n_{TXIF} = 2\pi\tau'_n f'_{TX}$, and take the expression for ϕ^n_{TX} from (2.2), (A.1) can be rewritten as,

$$\phi^n_{LOTX} = 2\pi(\tau'_n f'_{TX} - \tau_n f_{TX}). \tag{A.2}$$

Similarly, for the RX mixer at LSB2 mode,

$$\phi^n_{IFRX} = \underbrace{\phi^n_{LORX} - \phi_{RFRX}}_{\text{what we have}} = \underbrace{\phi^n_{RFRX} + \phi^n_{RX}}_{\text{what we want}} \Rightarrow \phi^n_{LO} = 2\phi_{RXRF} + \phi^n_{RX} \tag{A.3}$$

If we consider node B as the time reference in reception, $\phi^n_{RXRF} = 2\pi\tau_n f_{RX}$, and take the expression for ϕ^n_{RX} from (2.2), (A.1) can be rewritten as,

$$\phi^n_{LORX} = 2\pi(-\tau'_n f'_{RX} + \tau_n f_{RX}) \tag{A.4}$$

Appendix B

Details of RDPA prototype

B.1 Antenna modules used in RDPA prototype

The prototype antenna modules were designed and implemented using off-the-shelf discrete components. The schematic of the antenna modules and their bill of materials are displayed in Figures B.1, B.2 and B.3, and a sample of fabricated antenna module is shown in Figure B.4.

B.2 RF antenna elements used in RDPA prototype

The RF antenna element used in the prototype described in chapter 3 is a dual-band microstrip patch antenna. Its structure and specifications are displayed in Figure B.5. The top patch is probe fed and provides a resonance at 3 GHz, while the lower patch is proximity fed and resonates at 2 GHz.

In the prototype, 10 RF antenna elements on a ground plane are used to form a uniform linear array. The array is formed along the E-plane of the antenna element patterns to minimize mutual coupling between them. Figure B.5 displays the structure of the single element and 10-element E-plane array and the measured input matching of all ten elements. Figure B.6 shows the simulated radiation patterns and active impedances (seen at all 10 ports) for different scan angles.

B.3 Details of prototype circuit measurements

The typical spectrum of LO_{TX} and LO_{RX} signal from the LO generator circuit of an RDPA module and the $TX-RF$ and $RX-IF$ signals of the same module are displayed in Figure B.7. The level of these signals across 10 antenna modules are also shown in Figure B.8. Each antenna modules draws around 800 mA from a 15 V switching power supply.

B.4 Derivation of phases used in full-wave simulation for beam steering

In the prototype, the antenna modules are placed at uniform spacings in a row to create a uniform linear array. The angle of the array factor of the array can be easily calculated from [29],

$$\theta = \arcsin(\frac{\Delta\phi}{2\pi f}\frac{c}{d}), \tag{B.1}$$

where $\Delta\phi$ is the phase shift between each consecutive antenna element, f is frequency, c is the speed of light, and d is the inter-element distance. In the RDPA prototype d is 5 cm and f is 3 GHz and 2 GHz for the TX and RX modes, respectively. Therefore, $\Delta\phi$ for the TX mode should be $\times 1.5$ that of $\Delta\phi$ for the RX mode to achieve the same array factor beam angle for both modes. By choosing $\Delta\phi_{TX} = -150^\circ : 37.5^\circ : +150^\circ$ and $\Delta\phi_{RX} = -100^\circ : 25^\circ : +100^\circ$, the array factor beam angles are $\theta_0 = [-56.4^\circ, -38.7^\circ, -24.6^\circ, -12.0^\circ, 0^\circ, 12.0^\circ, 24.6^\circ, 38.7^\circ, 56.4^\circ]$.

B.5 RDPA prototype fixture

The 10-module prototype was assembled according to the block diagram of Figure 3.1. Figure B.9 displays the 10-module prototype with its fixture and a 45 cm ground plane.

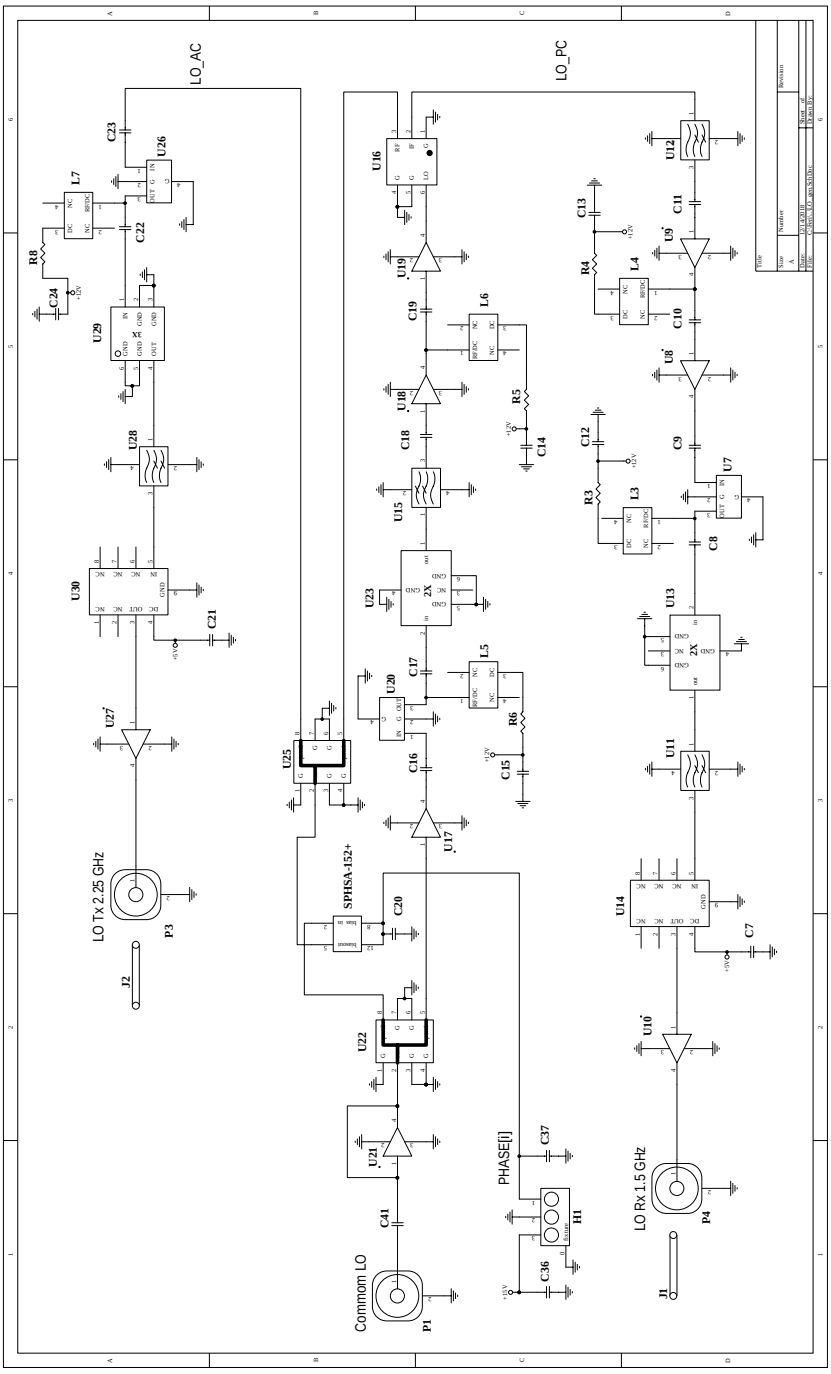

Figure B.1: Schematic diagram of LO generator in antenna modules used in prototype.

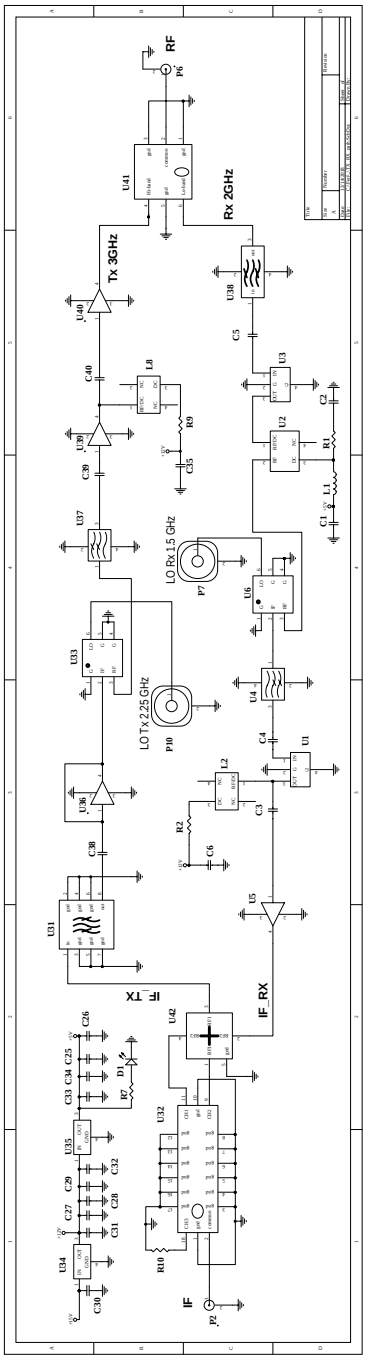

Figure B.2: Schematic diagram of RX and TX paths in antenna modules used in prototype.

Bill of Materials For Project [RDPA_v2.PrjPcb]

ITEM	Comment	Designator	Description	QTY
1	ATC530L104	C1, C2, C6, C7, C12, C13, C14, C15, C20, C24, C25, C26, C27, C28, C29, C31, C32, C33, C34, C35, C36, C37	Capacitor (Semiconductor SIM Model)	22
2	ATC520L103	C3, C4, C5, C8, C9, C10, C11, C16, C17, C18, C19, C21, C22, C23, C38, C39, C40, C41	Capacitor (Semiconductor SIM Model)	18
3	C1632X5R1E474M115AC	C30	0.47µF ±20% 25V Ceramic Capacitor X5R 0612 (1632 Metric)	1
4	LTST-C191KRKT	D1	LTST-C191KRKT Lite-On Inc. LED RED	1
5	LQW15AN43N	L1	43nH Unshielded Wirewound Inductor 250mA 700 mOhm	1
6	TCCH-80+	L2, L3, L4, L5, L6, L7, L8		7
7	SMA_thru_hole_amphenol_	P1, P3, P4, P7, P10	SMA Connector Jack, Female Socket 50 Ohm Through Hole	5
8	CONSMA006.062	P2, P6	SMA Connector Receptacle, Female	2
9	RC1206FR-0733R2L	R1	33.2 Ohm ±1% 0.25W, 1/4W Chip Resistor 1206 (3216 Metric)	1
10	CRCW201090R9FKEF	R2, R3, R6	90.9 ohm, 1%, 3/4W	3
11	CRCW2010133RFKEF	R4	133 Ohm ±1% 0.75W, 3/4W Chip Resistor 2010 (5025 Metric)	1
12	RHM200BFCT-ND	R5, R8	200 Ohm ±1% 0.5W, 1/2W Chip Resistor 2010 (5025 Metric)	2
13	470 ohm	R7	Resistor	1
14	RMCF2010FT110R	R9	110 Ohm ±1% 0.75W, 3/4W Chip Resistor 2010 (5025 Metric)	1
15	50 ohm	R10	Resistor	1
16	GALI-74+	U1, U7, U20, U26		4
17	TCBT-14+	U2		1
18	PGA-105+	U3		1
19	LFCN-900	U4, U12	LPF	2
20	PAT-3	U5, U40	MMIC-SHORT	1
21	ADE-30	U6, U16, U33	Mixer	3
22	PAT-0+	U8		1
23	MAR-4SM+	U9		1
24	PAT-1	U10, U17		2
25	BFCN-1525	U11, U15	LPF	2
26	SYK-2R	U13, U23	Doupler	2
27	YSF-162+	U14		1
28	MAR-3SM+	U18		1
29	PAT-6+	U19		1
30	BP2C1+	U22, U25	power slitter 650-1100 MHz	2
31	SPHSA-152+	U24	Phase Shifter	1
32	PAT-04+	U27		1
33	BFCN-2275	U28	LPF	1
34	RMK-3-33+	U29	Tripler	1
35	YSF-232+	U30		1
36	SXBP-707+	U31		1
37	TPLX-F2700+	U32		1
38	MC7812ACD2TG	U34	Three-Terminal Positive Voltage Regulator	1
39	MC7805CD2TG	U35	Three-Terminal Positive Voltage Regulator	1
40	BFCN-3010	U37	LPF	1
41	BFCN-1945+	U38		1
42	ERA-5SM+	U39		1
43	TDK_DPX202500DT	U41	Diplexer	1
44	Cross_over_RF	U42		1
				106

Figure B.3: Bill of materials of the RDPA modules used in the prototype.

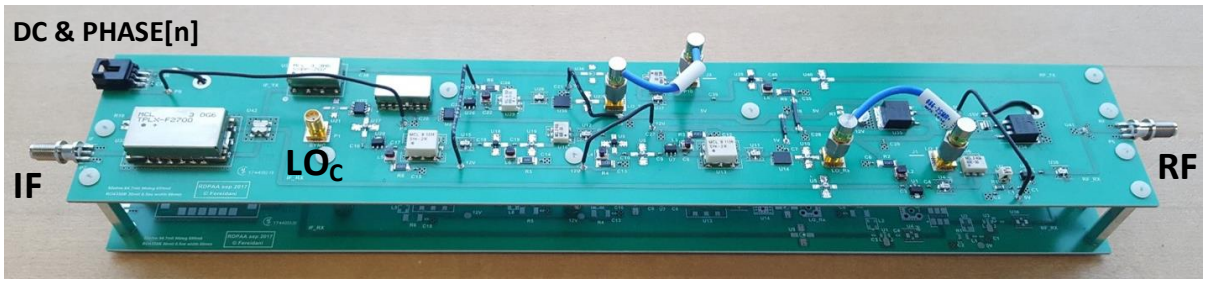

Figure B.4: A sample of antenna module used in the prototype.

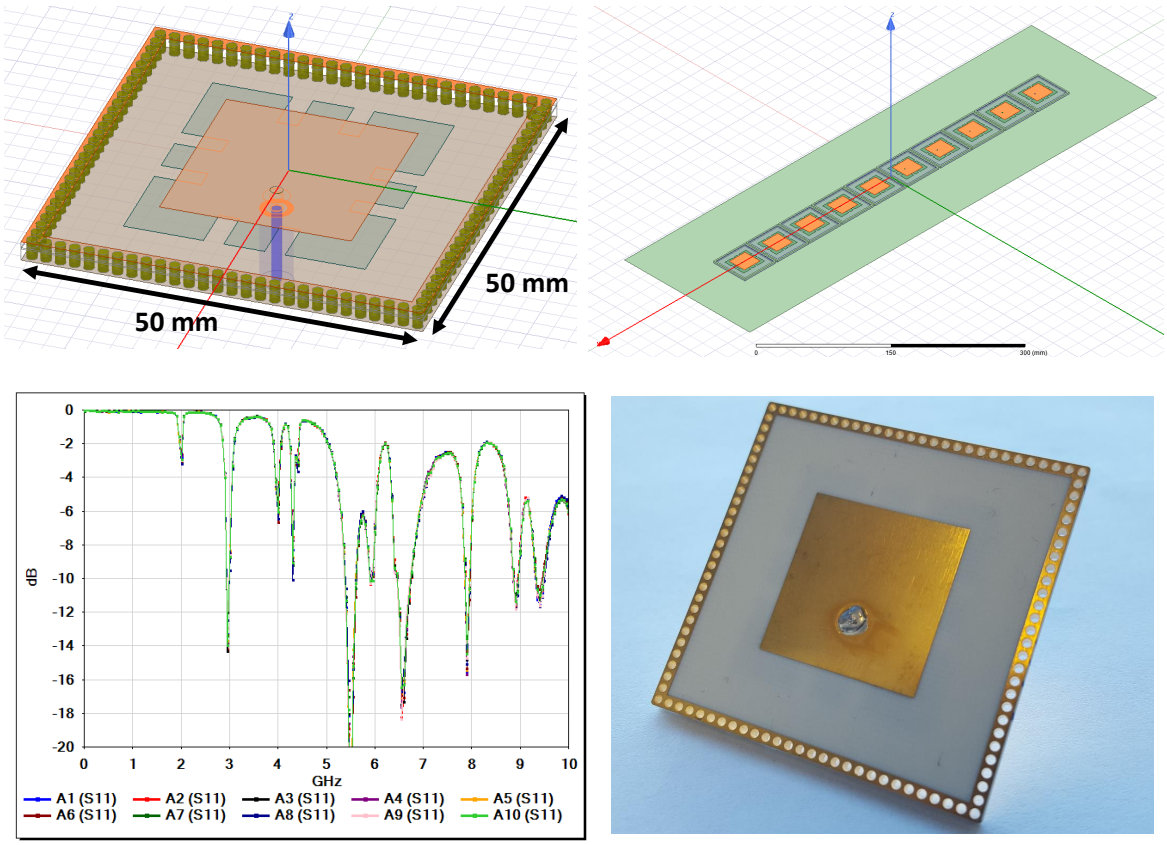

Figure B.5: Top-left: Dual band patch antenna. Top-right: 10-element E-plane array. Bottom-left: Measured input matching of all ten elements. Bottom-right: Sample fabricated antenna element.

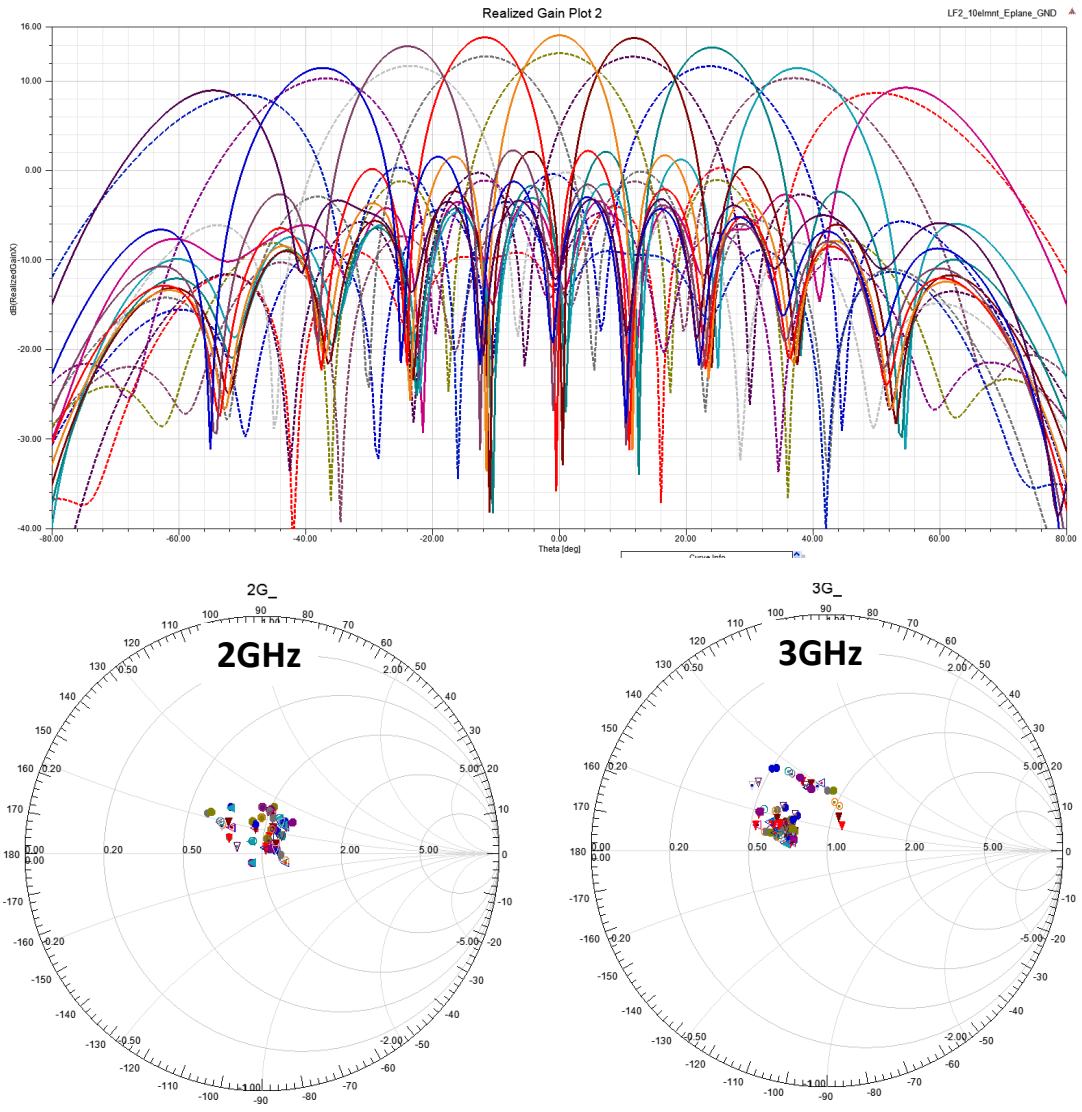

Figure B.6: Top: 10-element array radiation patterns for different scan angles (TX: solid lines, RX: dashed lines). Bottom: Active impedances (seen at all 10 ports) for scan angles 0 to 60°.

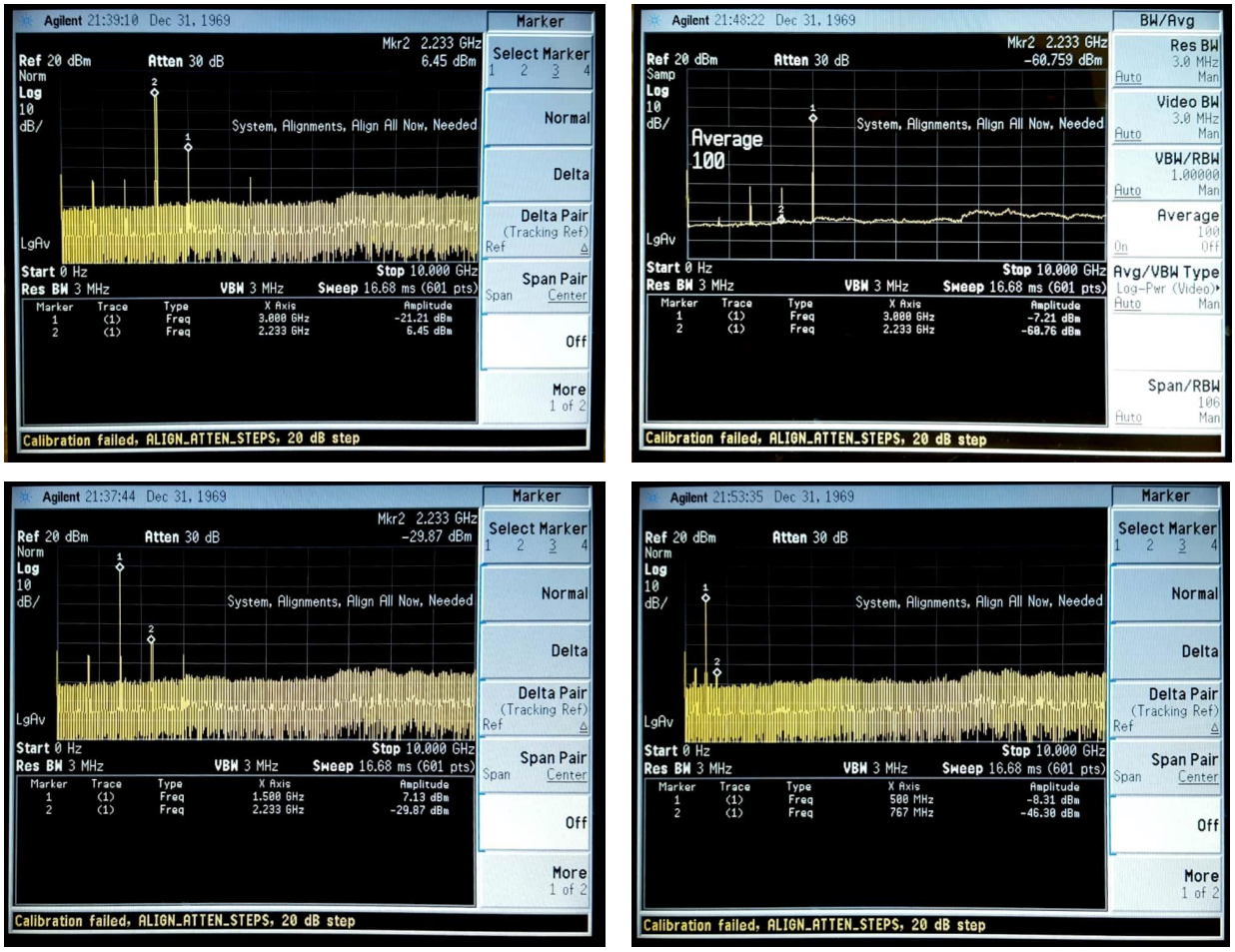

Figure B.7: The typical spectrum of an RDPA module used in the prototype. Top-left: LO_{TX}. Top-right: $TX - RF$. Bottom-left: LO_{RX}. Bottom-right: $RX - IF$.

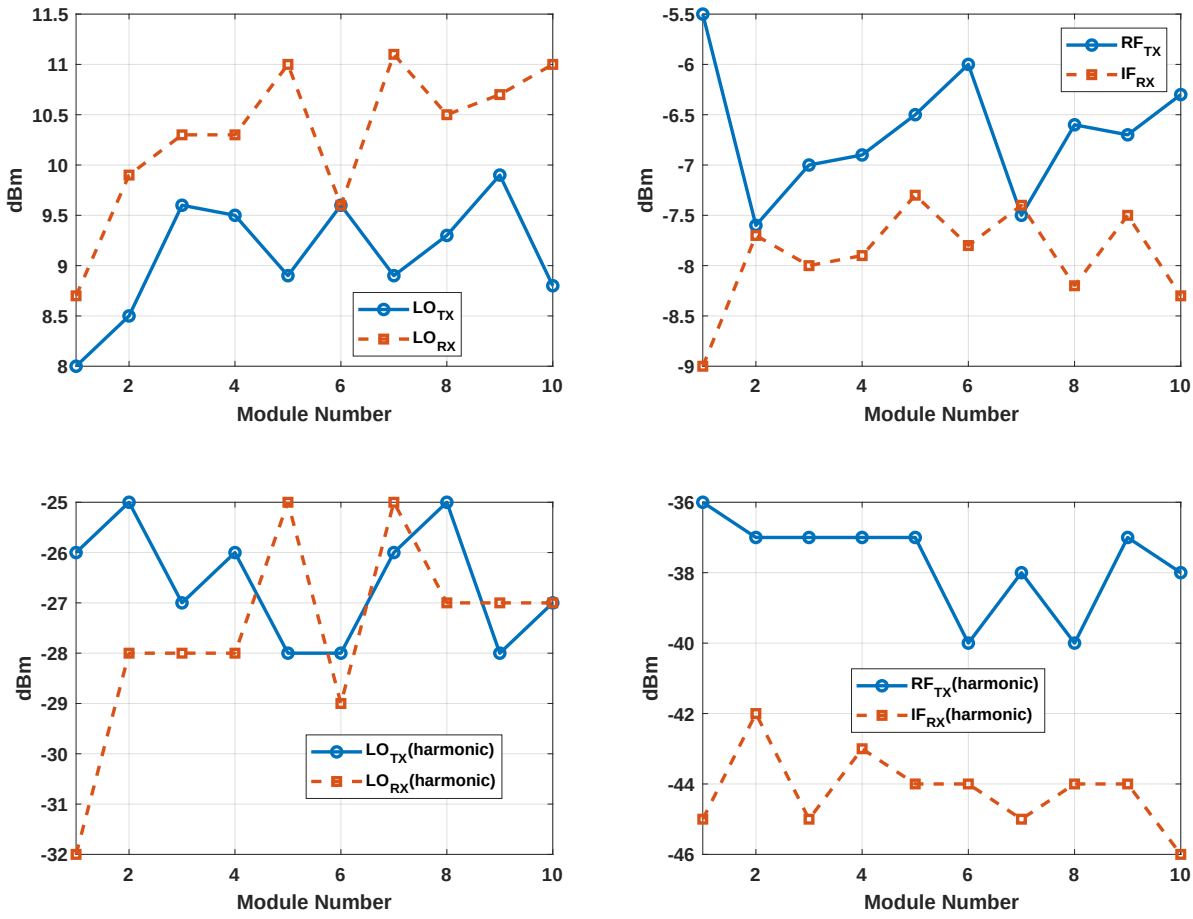

Figure B.8: Signal power test results on all 10 antenna modules. Top-left: $LO_{TX} = 2.25\,\text{GHz}$ and $LO_{RX} = 1.5\,\text{GHz}$ signal power. Top-right: Power of $RF_{TX} = 3\,\text{GHz}$ signal for input of $IF_{TX} = 0.75\,\text{GHz}, 0\,\text{dBm}$, Power of $IF_{RX} = 0.5\,\text{GHz}$ signal for input of $RF_{RX} = 2\,\text{GHz}, -31\,\text{dBm}$. Bottom-left: largest unwanted harmonic power in LO_{TX} spectrum at $LO_{TX}(harmonic) = 3\,\text{GHz}$, and largest unwanted harmonic power in LO_{RX} spectrum at $LO_RX(harmonic) = 3\,\text{GHz}$. Bottom-right: largest unwanted harmonic power in RF_{TX} spectrum at $RF_{TX}(harmonic) = 2.25\,\text{GHz}$, and largest unwanted harmonic power in IF_{RX} spectrum at $LO_RX(harmonic) = 0.25\,\text{GHz}$.

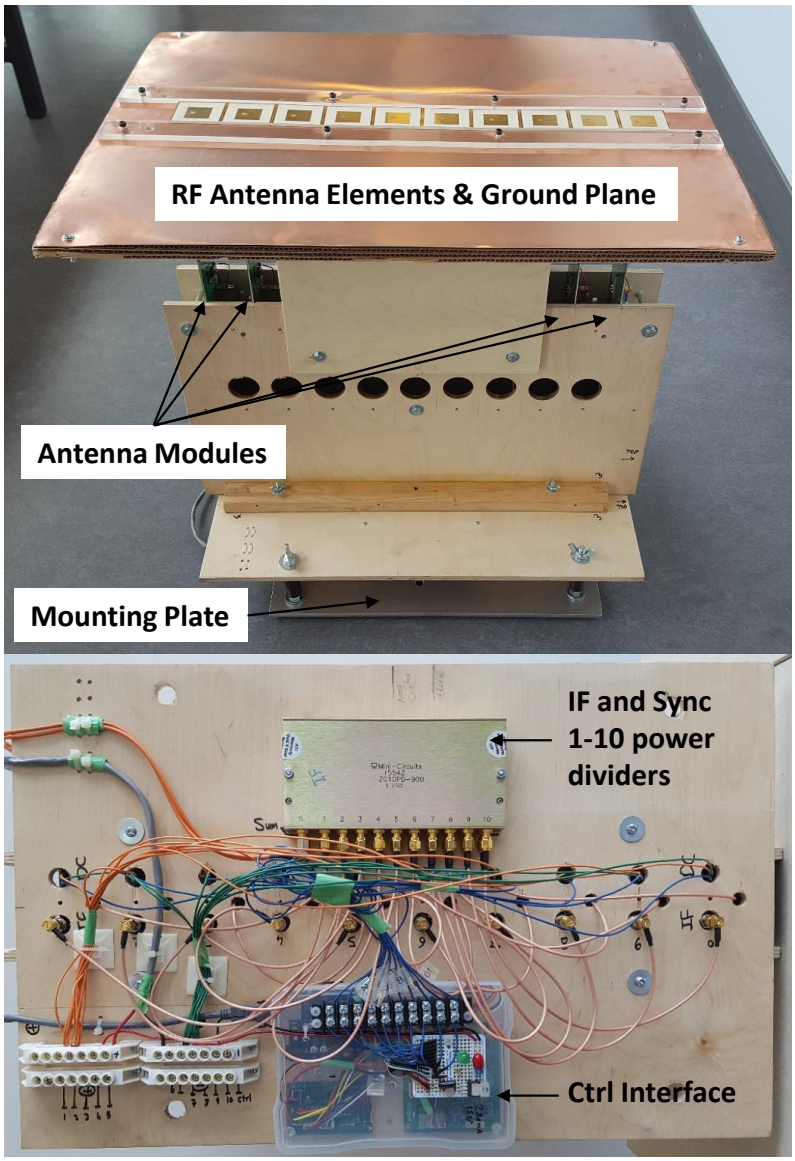

Figure B.9: Top: 10-module prototype test fixture. Bottom: Back of the fixture.

References

[1] Y. Zhang, K. Yang, and M. Amin, "Adaptive array processing for multipath fading mitigation via exploitation of filter banks," *IEEE Transactions on Antennas and Propagation*, vol. 49, no. 4, pp. 505–516, Apr. 2001.

[2] A. Fenn, *Adaptive Antennas and Phased Arrays for Radar and Communications:*. Artech House, 2007.

[3] J. Winters, "Smart antennas for wireless systems," *Personal Communications, IEEE*, vol. 5, no. 1, pp. 23–27, Feb. 1998.

[4] A. S. Ivica Stevanovic and J. R. Mosig, "Smart antenna systems for mobile communications," Ecole Polytechnique Federale de Lausanne, Tech. Rep., 2003.

[5] F. Khan, "Mobile internet from the heavens," *CoRR*, vol. abs/1508.02383, 2015.

[6] "http://www.parabolicarc.com/2017/03/03/spacex-launch-12000-satellites/."

[7] "http://oneweb.world."

[8] "www.o3bnetworks.com."

[9] "https://www.google.com/loon/."

[10] "www.internet.org/projects."

[11] P. Mousavi, M. Fakharzadeh, S. Jamali, K. Narimani, M. Hossu, H. Bolandhemmat, G. Rafi, and S. Safavi-Naeini, "A low-cost ultra low profile phased array system for mobile satellite reception using zero-knowledge beamforming algorithm," *Antennas and Propagation, IEEE Transactions on*, vol. 56, no. 12, pp. 3667–3679, Dec. 2008.

[12] E. Alian and et.al., "An efficient signal processing technique for phased arrays in satellite communications," in *ProEuromicro Conf. DSD/SEAA*, Czech Republic, Aug. 2018.

[13] N. B. Buchanan, V. F. Fusco, and M. Vorst, "SATCOM retrodirective array," *IEEE Transactions on Microwave Theory and Techniques*, vol. 64, no. 5, pp. 1614–1621, May 2016.

[14] S. Chandran, *Adaptive Antenna Arrays: Trends and Applications*. Springer Berlin Heidelberg, 2013.

[15] A. Van, "Electromagnetic reflector," Oct. 6 1959, US Patent 2,908,002.

[16] S. Andre and D. Leonard, "An active retrodirective array for satellite communications," *Antennas and Propagation, IEEE Transactions on*, vol. 12, no. 2, pp. 181–186, Mar. 1964.

[17] N. Buchanan, T. Brabetz, and V. Fusco, "A 62/66 GHz frequency offset retrodirective array," in *Microwave Symposium Digest, 2002 IEEE MTT-S International*, vol. 1, June 2002, pp. 315–318 vol.1.

[18] C. Pobanz, "Time varying active antennas, circuits and applications," Ph.D. dissertation, University California at Los Angeles, 1997.

[19] C. W. Pobanz and T. Itoh, "A microwave noncontact identification transponder using subharmonic interrogation," *Microwave Theory and Techniques, IEEE Transactions on*, vol. 43, no. 7, pp. 1673–1679, Jul 1995.

[20] T. Brabetz, V. Fusco, and S. Karode, "Balanced subharmonic mixers for retrodirective-array applications," *Microwave Theory and Techniques, IEEE Transactions on*, vol. 49, no. 3, pp. 465–469, Mar 2001.

[21] J.-Y. Park and T. Itoh, "A 60- GHz 4th subharmonic phase-conjugated retrodirective array," in *Microwave Conference, 2004. 34th European*, vol. 3, Oct 2004, pp. 1277–1280.

[22] K. Leong, Y. Wang, and T. Itoh, "A full duplex capable retrodirective array system for high-speed beam tracking and pointing applications," *Microwave Theory and Techniques, IEEE Transactions on*, vol. 52, no. 5, pp. 1479–1489, May 2004.

[23] L. DiDomenico and G. Rebeiz, "Digital communications using self-phased arrays," *Microwave Theory and Techniques, IEEE Transactions on*, vol. 49, no. 4, pp. 677–684, Apr 2001.

[24] "https://www.viasat.com/."

[25] D. Pozar, *Microwave Engineering*, 4th ed. Wiley, 2011.

[26] P. Vadivelu, P. Sen, S. Sarkar, D. Dawn, S. Pinel, and J. Laskar, "Integrated CMOS mm-wave phase shifters for single chip portable radar," in *Microwave Symposium Digest, 2009. MTT '09. IEEE MTT-S International*, June 2009, pp. 565–568.

[27] A. Abdellatif, N. Ranjkesh, M. Fahimnia, A. Taeb, S. Gigoyan, and S. Safavi-Naeini, "Low insertion loss variable phase shifter for emerging millimeter-wave communication systems," in *Microwave Symposium (IMS), 2014 IEEE MTT-S International*, June 2014, pp. 1–4.

[28] K. F. Braun, "Electrical oscillations and wireless telegraphy," *Nobel Lecture, December*, vol. 11, no. 1909, pp. 226–245, 1909.

[29] C. Balanis, *Antenna theory: analysis and design*, 3rd ed. Wiley India Pvt. Limited, 2009.

[30] R. C. Hansen, *Phased Array Antennas*, 1st, Ed. Wiley, 1998.

[31] J.-L. Kuo and etal, "60- GHz four-element phased-array transmit/receive system-in-package using phase compensation techniques in 65-nm flip-chip CMOS process," *Microwave Theory and Techniques, IEEE Transactions on*, vol. 60, no. 3, pp. 743–756, March 2012.

[32] G. Rebeiz, "Millimeter-wave sige rfics for large-scale phased-arrays," in *Bipolar/BiCMOS Circuits and Technology Meeting (BCTM), 2014 IEEE*, Sept 2014, pp. 56–59.

[33] A. Clemente, L. Dussopt, R. Sauleau, P. Potier, and P. Pouliguen, "Wideband 400-element electronically reconfigurable transmitarray in X band," *Antennas and Propagation, IEEE Transactions on*, vol. 61, no. 10, pp. 5017–5027, Oct 2013.

[34] "http://www.kymetacorp.com/technology/."

[35] "www.thinkom.com/land/mobile."

[36] M. Abdalla, K. Phang, and G. Eleftheriades, "A planar electronically steerable patch array using tunable pri/nri phase shifters," *Microwave Theory and Techniques, IEEE Transactions on*, vol. 57, no. 3, pp. 531–541, March 2009.

[37] P. Chang, "A photonic integrated-optic RF phase shifter for phased array antenna beam-forming applications," *Lightwave Technology, Journal of*, vol. 11, no. 12, pp. 2201–2205, Dec 1993.

[38] T.-Y. Yun, C. Wang, P. Zepeda, C. Rodenbeck, M. Coutant, M. yi Li, and K. Chang, "A 10- to 21- GHz, low-cost, multifrequency, and full-duplex phased-array antenna system," *Antennas and Propagation, IEEE Transactions on*, vol. 50, no. 5, pp. 641–650, May 2002.

[39] J. Buckwalter, A. Babakhani, A. Komijani, and A. Hajimiri, "An integrated subharmonic coupled-oscillator scheme for a 60- GHz phased-array transmitter," *Microwave Theory and Techniques, IEEE Transactions on*, vol. 54, no. 12, pp. 4271–4280, Dec 2006.

[40] J. Rao, D. Patel, and V. Krichevsky, "Voltage-controlled ferroelectric lens phased arrays," *Antennas and Propagation, IEEE Transactions on*, vol. 47, no. 3, pp. 458–468, Mar 1999.

[41] A. Gheethan, R. Guldiken, and G. Mumcu, "Microfluidic enabled beam scanning focal plane arrays," in *Antennas and Propagation Society International Symposium (APSURSI), 2013 IEEE*, July 2013, pp. 208–209.

[42] M. FEREIDANI SAMANI and S. NAEINI, "Adaptive phased array antenna architecture," Patent WO 2017/152 276 Al, 2017.

[43] M. Fereidani-Samani and S. Safavi-Naieni, "A novel retro-directive phased array antenna for two-way wireless links," *IEEE Transactions on Microwave Theory and Techniques, Special Issue on 5G Hardware and System Technologies*, submitted on Oct. 2018.

[44] H. H. Niknejad, Ali M., Ed., *mm-Wave Silicon Technology.* Springer US, 2008.

[45] F. O'Mahony, C. P. Yue, M. A. Horowitz, and S. S. Wong, "Design of a 10 GHz clock distribution network using coupled standing-wave oscillators," in *Proceedings of the 40th Annual Design Automation Conference.* New York, NY, USA: ACM, 2003, pp. 682–687.

[46] D. Cheng, *Field and Wave Electromagnetics: Pearson New International Edition*. Pearson Education Limited, 2014.

[47] F. P. OMahony, "10 GHz global clock distribution using coupled standing-wave oscillators," Ph.D. dissertation, Stanford University, 2003.

[48] J. Liu, T.-K. Jang, Y. Lee, J. Shin, S. Lee, T. Kim, J. Park, and H. Park, "A $0.012mm^2$ 3.1mw bang-bang digital fractional- N PLL with a power-supply-noise cancellation technique and a walking-one-phase-selection fractional frequency divider," in *2014 IEEE International Solid-State Circuits Conference Digest of Technical Papers (ISSCC)*. IEEE, feb 2014.

[49] W. Robins, *Phase Noise in Signal Sources: Theory and Applications*, ser. IEE telecommunications series. P. Peregrinus, 1984.

[50] Y. Zheng and C. E. Saavedra, "Full 360 vector-sum phase-shifter for microwave system applications," *IEEE Transactions on Circuits and Systems I: Regular Papers*, vol. 57, no. 4, pp. 752–758, Apr. 2010.

[51] A. W. Houghton and P. V. Brennan, "Phased array control using phase-locked-loop phase shifters," *IEE Proceedings H - Microwaves, Antennas and Propagation*, vol. 139, no. 1, pp. 31–37, Feb 1992.

[52] S. A. R. A. Mehr, M. Tohidian, and R. B. Staszewski, "Toward solving multichannel RF-SoC integration issues through digital fractional division," *IEEE Transactions on Very Large Scale Integration (VLSI) Systems*, vol. 24, no. 3, pp. 1071–1082, Mar. 2016.

[53] C.-C. Lin and C.-K. Wang, "A regenerative semi-dynamic frequency divider for mode-1 MB-OFDM UWB hopping carrier generation," in *ISSCC. 2005 IEEE International Digest of Technical Papers. Solid-State Circuits Conference, 2005.*

[54] D. Guermandi, P. Tortori, E. Franchi, and A. Gnudi, "A 0.75 to 2.2 GHz continuously-tunable quadrature VCO," in *ISSCC. 2005 IEEE International Digest of Technical Papers. Solid-State Circuits Conference, 2005.*

[55] Y.-F. Kuo and R.-M. Weng, "Regenerative frequency divider for 14 sub-band UWB applications," *Electronics Letters*, vol. 44, no. 2, p. 111, 2008.

[56] J. Lee and B. Razavi, "A 40- GHz frequency divider in 0.18um CMOS technology," *IEEE Journal of Solid-State Circuits*, vol. 39, no. 4, Apr. 2004.

[57] B. Acikel, T. R. Taylor, P. J. Hansen, J. S. Speck, and R. A. York, "A new high performance phase shifter using ba/sub x/sr/sub 1-x/tio3thin films," *IEEE Microwave and Wireless Components Letters*, vol. 12, no. 7, pp. 237–239, July 2002.

[58] H. Zarei and D. J. Allstot, "A low-loss phase shifter in 180 nm cmos for multiple-antenna receivers," in *2004 IEEE International Solid-State Circuits Conference (IEEE Cat. No.04CH37519)*, Feb 2004, pp. 392–534 Vol.1.

[59] J. Lee and S. Kim, "60 ghz switched-line-type phase shifter using body-floating switches in 0.13 um cmos technology," *Electronics Letters*, vol. 48, no. 7, pp. 376–378, March 2012.

[60] M. Cook and J. W. M. Rogers, "A highly compact 2.4-ghz passive 6-bit phase shifter with ambidextrous quadrant selector," *IEEE Transactions on Circuits and Systems II: Express Briefs*, vol. 64, no. 2, pp. 131–135, Feb 2017.

[61] K. Koh and G. M. Rebeiz, "0.13-μm cmos phase shifters for x-, ku-, and k-band phased arrays," *IEEE Journal of Solid-State Circuits*, vol. 42, no. 11, pp. 2535–2546, Nov 2007.

[62] J. Kaukovuori, K. Stadius, J. Ryynanen, and K. Halonen, "Analysis and design of passive polyphase filters," *IEEE Transactions on Circuits and Systems I: Regular Papers*, vol. 55, no. 10, pp. 3023–3037, nov 2008.

[63] Ituah, Stanley, "High frequency receiver front-end module for active antenna applications," Master's thesis, 2015.